



University  
of Glasgow

Winata, Steven (2023) *Real-time motion correction for Magnetic Resonance Imaging of the human brain at 7 Tesla*. PhD thesis.

<https://theses.gla.ac.uk/83788/>

Copyright and moral rights for this work are retained by the author

A copy can be downloaded for personal non-commercial research or study, without prior permission or charge

This work cannot be reproduced or quoted extensively from without first obtaining permission from the author

The content must not be changed in any way or sold commercially in any format or medium without the formal permission of the author

When referring to this work, full bibliographic details including the author, title, awarding institution and date of the thesis must be given

Enlighten: Theses

<https://theses.gla.ac.uk/>  
[research-enlighten@glasgow.ac.uk](mailto:research-enlighten@glasgow.ac.uk)

# **Real-Time Motion Correction for Magnetic Resonance Imaging of the Human Brain at 7 Tesla**

Steven Winata, B.Eng. (Hons)

Submitted in fulfilment of the requirements for  
the degree of *Doctor of Philosophy*

School of Psychology and Neuroscience  
College of Medical, Veterinary and Life Sciences  
University of Glasgow



University  
of Glasgow

August 2023



# Abstract

Magnetic resonance imaging (MRI) at the magnetic field strength of 7 Tesla (7T) enhances the quality of images available for research and clinical use. The improvements are however accompanied by novel challenges that are specific to ultra high-field MRI, which includes field strengths of 7T and above. Transmit  $B_1^+$  field inhomogeneity is also higher, causing uneven signal intensity and linking to an uneven SAR distribution, which is also higher than at lower field strengths. The potential for higher spatial resolution imaging can also result in more pronounced motion artefacts. To address these issues in routine clinical use, motion correction strategies are required. This thesis describe the implementation of real-time, image-based Multislice Prospective Acquisition Correction (MS-PACE) technique for 7T MRI. Firstly, developmental work was done to establish a 7T-specific MS-PACE implementation. Pulse sequence and image reconstruction pipeline work was implemented using the Siemens Integrated Development Environment for Applications (IDEA) and Image Calculation Environment (ICE) framework. The technique was then validated in a task-based functional MRI study with healthy subjects. It was also integrated with parallel transmit imaging using slice-by-slice  $B_1^+$  shimming. Validation experiments were performed in vivo using the Siemens MAGNETOM Terra 7T MRI scanner (Siemens Healthineers, Erlangen, Germany) at the Imaging Centre of Excellence (ICE).



# Contents

<b>Abstract</b>	<b>i</b>
<b>Acknowledgements</b>	<b>xix</b>
<b>Declaration</b>	<b>xxi</b>
<b>1 Introduction</b>	<b>1</b>
<b>2 Theory</b>	<b>5</b>
2.1 Nuclear magnetic resonance . . . . .	5
2.1.1 Nuclear spin . . . . .	6
2.1.2 Boltzmann distribution . . . . .	7
2.1.3 Laboratory and rotating frames of reference . . . . .	9
2.1.4 Relaxation times and contrast . . . . .	11
2.1.5 Bloch equations . . . . .	14
2.2 Image formation . . . . .	15
2.2.1 Slice-selection gradients . . . . .	15
2.2.2 Spatial encoding and k-space . . . . .	16
2.2.3 Gradient echo . . . . .	20
2.2.4 Spin echo . . . . .	21
2.2.5 Image reconstruction . . . . .	22
2.2.6 Parallel imaging acquisition and reconstruction . . . . .	22
2.3 Advanced sequences . . . . .	26
2.3.1 Echo planar imaging (EPI) . . . . .	26
2.3.2 Turbo spin echo (TSE) . . . . .	29
2.4 Simultaneous multislice imaging (SMS) . . . . .	31
2.4.1 Concept . . . . .	31

2.4.2	Reconstruction . . . . .	32
2.5	Ultra-high field MRI . . . . .	33
2.5.1	Parallel transmit MRI . . . . .	35
2.6	Functional MRI (fMRI) . . . . .	36
2.7	Motion correction in MRI . . . . .	37
2.7.1	The motion issue . . . . .	37
2.7.2	Motion correction techniques . . . . .	38
<b>3</b>	<b>Motion correction for echo-planar imaging at 7 Tesla using multislice prospective acquisition correction (MS-PACE)</b>	<b>47</b>
3.1	Introduction . . . . .	47
3.2	MS-PACE . . . . .	47
3.3	Equipment . . . . .	49
3.3.1	Locations and scanners . . . . .	49
3.3.2	Programs used for 7T MS-PACE technique development . . . . .	49
3.3.3	Phantom . . . . .	50
3.3.4	Coils . . . . .	51
3.4	Methods . . . . .	51
3.4.1	Motion detection: the effect of the number of slices in the registration subset . . . . .	51
3.4.2	Motion detection: the effect of intra-volume motion . . . . .	52
3.4.3	Application to real-time motion correction in fMRI protocol . . . . .	52
3.5	Results . . . . .	54
3.5.1	Motion detection: the effect of the number of slices in the registration subset . . . . .	54
3.5.2	Motion detection: the effect of intra-volume motion . . . . .	58
3.5.3	Application to real-time motion correction in fMRI protocol . . . . .	60
3.6	Discussion . . . . .	70
3.6.1	Motion detection: the effect of the number of slices in the registration subset . . . . .	70
3.6.2	Motion detection: the effect of intra-volume motion . . . . .	70
3.6.3	Application to real-time motion correction in fMRI protocol . . . . .	70
3.7	Conclusion . . . . .	72

<b>4</b>	<b>Prospective motion correction using MS-PACE for 7T task-based functional MRI (fMRI)</b>	<b>73</b>
4.1	Introduction . . . . .	73
4.2	Methods . . . . .	74
4.2.1	Functional analysis . . . . .	76
4.3	Results . . . . .	77
4.4	Discussion . . . . .	87
4.5	Conclusion . . . . .	90
<b>5</b>	<b>MS-PACE prospective motion correction using parallel transmit imaging (pTx) at 7T</b>	<b>91</b>
5.1	Introduction . . . . .	91
5.1.1	Online pTx pulse design and slice-by-slice $B_1^+$ shimming . . . . .	91
5.2	Methods . . . . .	92
5.2.1	Functional analysis . . . . .	95
5.3	Results . . . . .	96
5.3.1	Application of MS-PACE to data acquisition using pTx . . . . .	96
5.3.2	Comparison of MS-PACE corrected acquisitions in CP and pTx modes	103
5.4	Discussion . . . . .	107
5.4.1	Application of MS-PACE to data acquisition using pTx . . . . .	107
5.4.2	Comparison of MS-PACE corrected acquisitions in CP and pTx modes	108
5.5	Conclusion . . . . .	108
<b>6</b>	<b>Conclusion</b>	<b>109</b>
6.1	Future work . . . . .	109
6.2	Summary . . . . .	111
<b>A</b>	<b>Using unseparated multiband slices as an image registration shortcut</b>	<b>113</b>
A.1	Introduction . . . . .	113
A.2	Methods . . . . .	114
A.3	Results . . . . .	115
A.4	Discussion . . . . .	116
A.5	Proposed future algorithm . . . . .	116
<b>B</b>	<b>Preliminary work on MS-PACE navigated turbo spin echo (TSE) at 7T</b>	<b>119</b>



# List of Tables

3.1	Mean and standard deviation ( <i>mean</i> $\pm$ <i>SD</i> ) of the non-corrected and corrected translation and rotation parameter estimates (x, y and z-axes) from three separate subject acquisitions. . . . .	65
3.2	The results of Student t-test comparing the means of each rigid body parameter from scans with against without prospective motion correction. The numbers in parentheses signify the degrees of freedom in each statistical calculation, which is the number of pairs evaluated subtracted by 1. . . . .	65
4.1	The six EPI scans acquired from each subject and the task variation. The acquisition order was varied for each subject. . . . .	75
4.2	The results of Student t-test comparing the mean voxel displacement from scans with against without MS-PACE in the three functional group scans. The numbers in parentheses signify the degrees of freedom in each statistical calculation, which is the number of pairs evaluated subtracted by 1. . . . .	77
4.3	The results of Student t-test comparing the GLM results from tapping scans with prospective motion correction versus without (but retrospectively-corrected). The numbers in parentheses signify the degrees of freedom in each statistical calculation, which is the number of pairs evaluated subtracted by 1. . . . .	84
4.4	Comparison of outside-primary motor cortex ROI activation as a percentage of the full normalised Talairach brain slice in the integrated GLM map with an individual motion correction technique, i.e. BrainVoyager standard retrospective correction (RC) and MS-PACE. . . . .	87
5.1	The parameter variation of the four functional scans acquired from each subject.	94

5.2 Student t-test comparing the mean voxel displacement from scans with against without MS-PACE in both transmit modes. The numbers in parentheses signify the degrees of freedom in each statistical calculation, which is the number of pairs evaluated subtracted by 1. . . . . 99

# List of Figures

2.1	The precession of the magnetic moment $\vec{\mu}$ of hydrogen around the static, external magnetic field $\vec{B}_0$ at the Larmor frequency $\omega_L$ . The sense of rotation is shown for nuclei, such as protons, with a positive gyromagnetic ratio. . . . .	7
2.2	The energy level diagram for hydrogen ( $I=1/2$ ) when subjected to an external field $B_0$ , illustrating the Zeeman splitting. $\Delta E$ is the energy differential between the two energy states. . . . .	8
2.3	Magnetisation as viewed using the laboratory (left) and rotating (right) frame of reference. $B_1^{eff}$ is the effective $\vec{B}_1$ in the rotating frame of reference. . . . .	10
2.4	Longitudinal relaxation after an excitation with a $90^\circ$ RF pulse. The time constant $T_1$ is equivalent to 63% ( $\approx 1 - \frac{1}{e}$ ) of the maximum longitudinal magnetisation ( $M_0$ ). . . . .	12
2.5	Transverse relaxation after an excitation with a $90^\circ$ RF pulse. The time constant $T_2$ is equivalent to 37% ( $\approx \frac{1}{e}$ ) of the initial transverse magnetisation ( $M_{xy}$ ). . .	13
2.6	The free induction decay (FID) signal with its characteristic exponential decay. . . . .	14
2.7	A slice of specified thickness $\Delta z$ excited by the slice-selection gradient $G_z$ and an RF pulse containing the defined resonant frequency bandwidth $\Delta\omega$ . . . . .	16
2.8	A pulse diagram showing a sinc-shaped RF excitation pulse along with the slice-selection gradient and its corresponding rephasing gradient. . . . .	16
2.9	The application of a phase encoding gradient causes the spins across the sample to precess at varying frequencies. While these return to the Larmor frequency after the gradient has passed, each spin now possesses a unique phase angle. . .	18

2.10	Example of a Cartesian k-space acquisition pattern. Firstly (in a), the frequency and phase encoding gradients are applied to shift the encoding to the corner of the k-space from the centre (red dot). Readout is started and the frequency encoding gradient is then applied to acquire the first line of k-space. Then, a new combination of phase encoding gradient and frequency prephase gradient is applied to start another k-space line acquisition. The process is repeated until all the lines are acquired (in b). . . . .	19
2.11	A basic gradient echo sequence. After an initial low flip angle $\alpha$ RF pulse (typically less than $90^\circ$ in a fast low angle shot or FLASH gradient echo sequence [27]), a dephasing readout gradient ( $G_x$ ) is applied. A rephasing gradient then immediately follows. The phase encoding gradient ( $G_y$ ) is applied in steps in order to acquire the entire image. At the echo time (TE), a gradient echo forms and can be acquired. Data sampling is applied during the frequency-encoding gradient. . . . .	20
2.12	A basic spin echo sequence. After an initial RF pulse and eventual decay of the signal, a $180^\circ$ refocusing RF pulse is applied. A spin echo forms, which is at its peak at the echo time (TE). . . . .	21
2.13	(a) The representation of an image acquired using turbo spin echo (TSE) in the k-space domain and (b) the actual image after a 2D inverse discrete Fourier transform is performed on the k-space data. This sequence type was originally published under the name RARE [29]. . . . .	23
2.14	Representation of receive coil array for use in parallel imaging acquisition. . . .	24
2.15	Calculation of unsampled data points in GRAPPA. First, as in (a), GRAPPA coefficients are calculated from the autocalibration signal lines in each receive coil. Using these coefficient, unsampled data points can be calculated from its neighbouring sampled points in all coils as illustrated in (b). . . . .	25
2.16	(a) The undersampled k-space map from a receive coil of a turbo spin echo (TSE) acquisition with an acceleration factor of 3, where for every acquired line, the two following lines are unacquired. (b) Reconstructing the undersampled k-space directly results in aliasing. If the lines are filled using GRAPPA reconstruction with ACS data, the aliasing can be eliminated. . . . .	26
2.17	(a) A pulse diagram showing a single-shot, gradient-echo EPI sequence. The echo spacing represents the time between the readout of two k-space lines. (b) The k-space trajectory of a single-shot EPI acquisition. . . . .	28

---

2.18	A turbo spin echo (TSE) sequence with an echo train length (ETL) of 4. After an initial RF excitation pulse, a series of refocusing RF pulses is applied. Multiple spin echoes form in the interval between the refocusing pulses, allowing for more k-space readouts. The first echo appears after approximately twice the time between the excitation and refocusing pulses ( $2\tau$ ). $G_y$ gradients are varied from excitation to excitation and from echo to echo. . . . .	30
2.19	(a) To excite several slices simultaneously, a composite multiband RF pulse composed of two single-band RF pulses with a frequency offset of $\omega$ is used. (b) Using the blipped-CAIPI technique, where rewinding gradients are added in slice-select direction, the slices are shifted by $FOV/2$ to simplify the separation process. . . . .	33
2.20	SNR values in different parts of the human brain plotted against the main magnetic field strength $B_0$ . A fitting of the cerebrum's SNR values is shown as the red line, showing a near-linear increase in SNR with increasing $B_0$ . Reproduced from [49] with permission from the publisher John Wiley and Sons, Inc. . . . .	34
2.21	Simulated gradient-echo images with increasing magnetic field strength, showing a regressing trend of image homogeneity. Reproduced from [4] with permission from the publisher John Wiley and Sons, Inc. . . . .	34
2.22	The comparison of (A) sagittal and (B) coronal MPRAGE images of the brain of a multiple sclerosis patient acquired with single (sTx) and parallel transmit (pTx) MRI. The cerebellum is highlighted with the red arrows. Reproduced from [50] with permission from the publisher IOP Publishing. . . . .	36
2.23	Various categories of motion mitigation and compensation techniques. Reproduced from [2] with permission from the publisher John Wiley and Sons, Inc. . . . .	39
2.24	The basic principle of iterative registration of two images with an optimiser and interpolator. This process is guided by a similarity metric. . . . .	41
3.1	The 7T MS-PACE motion detection and correction pipeline. In this example, as only a subset of three slices is used for each registration, detection and correction can be done multiple times within a repetition time. . . . .	48

3.2	A truncated version of the ICE image reconstruction pipeline developed for the 7T MS-PACE technique, demonstrating how the data processing branches into two. On ICE, the pipeline is constructed with individual processing modules (functors) with input and output nodes that control data flow between them. The data branches out of the <i>source</i> functor to form a separate real-time motion calculation branch towards the <i>MultiSliceRegFunctor</i> where motion estimation and feedback of motion parameters to the pulse sequence for real-time acquisition system updates occur. GRAPPA processing is also active in the real-time branch ( <i>GrappaFB</i> ). The other branch heads to the standard image reconstruction pipeline. . . . .	50
3.3	X-axis translation parameters acquired from the registration of the motion-affected dataset. The red curve signifies the reference volume-to-volume registration. The fewest (2) and the most (18) image registration slices cases are highlighted with bolder colours. The inset focuses on the 230-300s time window (post the right-tilting motion). . . . .	55
3.4	Translation parameters across the three spatial axes acquired from the registration of the motion-affected dataset with variable numbers of navigator slices. . . . .	56
3.5	Rotation parameters across the three spatial axes acquired from the registration of the motion-affected dataset with variable numbers of navigator slices. . . . .	57
3.6	A BOLD-EPI volume unaffected (a) and affected (b) by multidirectional intra-volume motion. . . . .	58
3.7	Translation and rotation parameters in both registration schemes. Blue curve shows full volume registration, red points show multislice-subset registrations. Volumes affected by intra-volume motion highlighted in grey. The translation parameters are in the left column, while the rotation ones are in the right column. . . . .	59
3.8	Rigid-body motion parameter estimates (x, y and z-axes) from the acquisitions without (blue) and with (red) real-time motion correction. The translation parameters are in the left column, while the rotation parameters are in the right column. . . . .	60

3.9	Box plot representation of the rigid body motion parameter estimates (x, y and z-axes) from the acquisitions without and with real-time motion correction. The translation parameters are in the left column, while the rotation parameters are in the right column. Each box includes the interquartile range (IQR) of the parameter values. The red line represents the median. Each whisker extends to the furthest data point in each wing that is within 1.5 times the IQR. Data points outside this range are represented by the outlier dots. . . . .	61
3.10	Temporal SNR (tSNR) maps from a single subject without (a) and with (b) real-time motion correction. These maps illustrate the temporal variance in noise and were calculated by comparing the mean signal of each voxel to its standard deviation over the time series. An improvement in tSNR is observed in (b). . .	62
3.11	Comparison of the non-corrected and corrected translation parameter estimates (x, y and z-axes) from three separate subject acquisitions using the same protocol. . . . .	63
3.12	Comparison of the non-corrected and corrected rotation parameter estimates (x, y and z-axes) from three separate subject acquisitions using the same protocol.	64
3.13	Comparison of the residual translation parameters calculated from a single subject with the multislice-to-volume method (left column) and with FSL's MCFLIRT tool (right column) from the acquisitions without (blue) and with (red) real-time motion correction. . . . .	66
3.14	Comparison of the residual rotation parameters calculated from a single subject with the multislice-to-volume method (left column) and with FSL's MCFLIRT tool (right column) from the acquisitions without (blue) and with (red) real-time motion correction. . . . .	67
3.15	Comparison of the rigid body motion parameter estimates with motion correction applied and with motion correction plus masking. These were retrospectively calculated post-acquisition. The data are derived from one subject. . . .	68
3.16	Comparison of the rigid body motion parameter estimates from a subject dataset acquired with the masking-enabled sequence, with motion correction applied and with motion correction plus masking. . . . .	69
4.1	The block design used in the study. The finger tapping task blocks were interleaved with the rest blocks. Apart from the first rest block, which included calibration scans, each rest/task block lasted 40 seconds, which is equal to 10 volumes. . . . .	74

4.2	Mean voxel displacement comparison of the acquisitions without and with MS-PACE prospective motion correction for the three groups of functional scans: resting (top), left-hand tapping (middle) and right-hand tapping (bottom). The error bars represent the standard deviation in each dataset. . . . .	78
4.3	Temporal SNR (tSNR) maps and differences ( $\delta$ tSNR) derived from the resting scans. The rows show data from individual subjects. In each row, the leftmost set of three images are from a lower slice, the middle set of three images are from a middle slice and the rightmost set of three images are from an upper slice. Within each set of three images, the first column is the tSNR map with MS-PACE turned off, the second column is the tSNR map with MS-PACE turned on, and the third column image is the $\delta$ tSNR(On-Off). . . . .	79
4.4	Average $\delta$ tSNR(On-Off) of the resting scans across all subjects. Each subject's $\delta$ tSNR map was normalised into the standard MNI152 space before the average was calculated. . . . .	80
4.5	Trimmed average $\delta$ tSNR(On-Off) of the resting scans across all subjects (extreme 5% excluded). Each subject's $\delta$ tSNR map was normalised into the standard MNI152 space before the average was calculated. . . . .	81
4.6	Temporal SNR (tSNR) maps and differences ( $\delta$ tSNR) derived from the resting scans in all ten subjects when prospective motion correction was turned off or on. The maps were plotted for slices 0 (most inferior), 20 and 40 in subject-native EPI space. In each row, the leftmost set of three images are from a lower slice, the middle set of three images are from a middle slice and the rightmost set of three images are from an upper slice. Within each set of three images, the first column is the tSNR map with MS-PACE turned off, the second column is the tSNR map with MS-PACE turned on, and the third column image is the $\delta$ tSNR(On-Off). . . . .	82
4.7	Analysis of scan update rate during prospective motion correction from one run, showing current imaging volume subset indices plotted against the origin subset of motion feedback received. The indices are of the first slice of each three-slice subset (e.g. 0 for 0-20-40, 1 for 1-21-41, etc.). The red-shaded area indicates feedback coming from the previous volume. . . . .	83

4.8	Integrated GLM results of all subjects' left-hand tapping paradigm scans without (a,c) and with (b,d) MS-PACE prospective motion correction. BrainVoyager-retrospectively-corrected (RC) data are shown in the bottom row. The white boxes indicate the location of the hemisphere's primary motor cortex on the Talairach brain (coronal view). The bar scale is of the $\beta$ weight, which indicates the activation during the task blocks. . . . .	85
4.9	Integrated GLM results of all subjects' right-hand tapping paradigm scans without (a,c) and with (b,d) MS-PACE prospective motion correction. BrainVoyager-retrospectively-corrected (RC) data are shown in the bottom row. The white boxes indicate the location of the hemisphere's primary motor cortex on the Talairach brain (coronal view). The bar scale is of the $\beta$ weight, which indicates the activation during the task blocks. . . . .	86
5.1	The 8-channel transmit, 64-channel receive head coil used in the study. The design features an open face to help reduce claustrophobic reactions. A visor mirror was placed to reflect the screen correctly towards the subject. Reproduced with permission from Dr G. Shajan. . . . .	93
5.2	The block design used in the study, which is similar to in Section 4.2. The finger tapping task blocks were interleaved with the rest blocks. Apart from the first rest block, which included calibration scans, each rest/task block lasted 40 seconds, which is equal to 10 volumes. . . . .	93
5.3	Transmit channel-wise $B_1^+$ field magnitude maps from the centre slice in one subject. . . . .	96
5.4	Transmit channel-wise $B_1^+$ field phase maps from the centre slice in one subject. . . . .	96
5.5	Combined $B_1^+$ field maps for slices 16, 26 (centre) and 36 in one subject. . . . .	97
5.6	Mean voxel displacement comparison of the acquisitions without and with MS-PACE prospective motion correction for the CP acquisitions. The error bars represent the standard deviation in each dataset. . . . .	98
5.7	Mean voxel displacement comparison of the acquisitions without and with MS-PACE prospective motion correction for the pTx acquisitions. The error bars represent the standard deviation in each dataset. . . . .	98

5.8	Temporal SNR (tSNR) maps and differences ( $\delta$ tSNR) derived from the pTx scans in all six subjects when prospective motion correction was turned off or on. The maps were plotted for slices 16, 26 (centre) and 36 in subject-native EPI space. In each row, the leftmost set of three images are from slice 16, the middle set of three images are from slice 26 and the rightmost set of three images are from slice 36. Within each set of three images, the first column is the tSNR map with MS-PACE turned off, the second column is the tSNR map with MS-PACE turned on, and the third column image is the $\delta$ tSNR(pTx-CP). . . . .	99
5.9	Mean $\delta$ tSNR(On-Off) of the pTx scans across all subjects. Each subject's $\delta$ tSNR map was normalised into the standard MNI152 space before the average was calculated. . . . .	100
5.10	Trimmed mean $\delta$ tSNR(On-Off) of the pTx scans across all subjects. Each subject's $\delta$ tSNR map was normalised into the standard MNI152 space before the average was calculated. . . . .	101
5.11	Integrated GLM results of all subjects' pTx scans without (a) and with (b) MS-PACE prospective motion correction. The white boxes indicate the location of the hemisphere's primary motor cortex on the Talairach brain (coronal view). The bar scale is of the $\beta$ weight, which indicates the activation during the task blocks. . . . .	102
5.12	Temporal SNR (tSNR) maps and differences ( $\delta$ tSNR) derived from the pTx scans in all six subjects when prospective motion correction was turned off or on. The maps were plotted for slices 16, 26 (centre) and 36 in subject-native EPI space. In each row, the leftmost set of three images are from slice 16, the middle set of three images are from slice 26 and the rightmost set of three images are from slice 36. Within each set of three images, the first column is the tSNR map with MS-PACE turned off, the second column is the tSNR map with MS-PACE turned on, and the third column image is the $\delta$ tSNR(pTx-CP). . . . .	103
5.13	Mean $\delta$ tSNR(pTx-CP) of the MS-PACE prospectively-corrected scans acquired in CP and pTx modes across all subjects. Each subject's $\delta$ tSNR map was normalised into the standard MNI152 space before the average was calculated. . .	104
5.14	Trimmed mean $\delta$ tSNR(On-Off) of the MS-PACE prospectively-corrected scans acquired in CP and pTx modes. Each subject's $\delta$ tSNR map was normalised into the standard MNI152 space before the average was calculated. . . . .	105

---

5.15	Integrated GLM results of all subjects' MS-PACE prospectively-corrected scans acquired on (a) CP and (b) pTx modes. The white boxes indicate the location of the hemisphere's primary motor cortex on the Talairach brain (coronal view). The bar scale is of the $\beta$ weight, which indicates the activation during the task blocks. . . . .	106
A.1	An unseparated MB slice and its corresponding slices after slice-GRAPPA separation. Notice the folding and aliasing effects on the MB slice. . . . .	114
A.2	Residual rigid-body motion parameters (x, y and z-axes) for the unseparated SMS volume registration (blue) and slice-GRAPPA separated SMS volume registration (red). The translation parameters are on the left column, while the rotation parameters are on the right column. . . . .	115
A.3	The schematic of image registration with collapsed multiband slices for simultaneous multislice imaging. After skipping the multiband separation process, a collapsed SMS-acquired slice (current image) is iterated through a registration process against a pseudo-collapsed reference image generated from earlier-acquired reference data. . . . .	117
B.1	Inferior (a), centre (b) and superior (c) slices from the 7T MS-PACE-navigated TSE sequence. The inset on the top left are the EPI navigators used for the corresponding TSE slices. Note the heavy blurring artefacts in all slices, reflecting that the application was still under development. . . . .	119



# Acknowledgements

I cannot emphasise enough on how this thesis would not have happened without the priceless support of many people at the Imaging Centre of Excellence (ICE) and outside. First and foremost, I feel very privileged to have Prof David Porter as my supervisor. Without his generous support and unparalleled scientific mind, I would have never reached this point. I am thankful for our long sessions of troubleshooting sequence issues at the scanner and for helping to nurture my scientific rigour and, most importantly, patience and persistence. Thank you for being always approachable and for your continuous reassurance. I am also grateful of my second supervisor Prof Keith Muir's accessibility, ideas and constant support.

A very special thanks to the two scientists in our small, tightly-knit MR Physics group at ICE. Thank you to Dr Graeme Keith for patiently putting up to my oft-silly questions, supporting my experimental work and giving important tips and comments that helped me to develop this thesis. Congratulations on your new house by the way! I look forward to watching rugby and football with you again soon. I am grateful as well to Dr Sydney Williams for her constant support, scientific and moral, that helped me to get to this point. I am so happy for you and Adal on your baby! Also to the best boy/dog Toby, I'm sure you will make a very good big brother to wee Máxi. Thanks, Graeme and Sydney, for lifting me up during the difficult times as well. I am lucky to have worked with excellent scientists like the both of you.

I am also grateful to Dr Daniel Hoinkiss at the Fraunhofer Institute of Digital Medicine MEVIS in Bremen, Germany. Thank you very much for your support in getting the technical translation and development of the motion correction technique for my thesis to happen. Your sharp knowledge in the area has helped me to develop my work properly. Many thanks to you and Prof Matthias Günther as well for hosting me in Bremen during my research visit.

Many thanks to a later addition to our ICE family, Dr Belinda Ding Yuan for her support in getting my experiments up and running. Your feedback and encouragement also helped me to plough on and finally cross the line. I am also grateful to have a colleague and friend from the same part of the world.

I thank my reviewers Dr Kristin Flegal and Dr John Foster for giving me constructive feed-

---

backs and encouragements during the reviews. I would like to also thank my viva voce examiners, Prof David Atkinson and Dr William Holmes, and the convener, Dr Junichi Hachisuka, for taking their time to examine my thesis and participate in my defence.

I am grateful as well for the colleagues I have worked with at ICE. A million thanks to Dr Jon Trinder for his constant IT support and for bearing with my insatiable need for storage space. Many thanks to Dr Salim al-Wasity and Dr Kristian Stefanov for helping me to design my fMRI studies and to understand the postprocessing steps. I am grateful to the NHS radiographers Rosie Woodward and Tracey Hopkins for supporting my scanner sessions and making sure these were done safely. I am also grateful for Jackie Staig's support, without whom volunteer recruitment would have been a nightmare! I want to thank my desk neighbour Dr Paul McElhinney for the interesting chats we had over the years. Also to Harvinder Deol and Kevan Dineen at the ICE front desk, thanks for always being approachable and helpful.

Especially sustaining me throughout these years is our incredible ICE pub quiz team, including our non-ICE members. I always looked forward to our frequent ventures and really enjoyed conquering different pub quizzes and doing other activities with you all. I am very grateful that we have been able to develop our friendships outwith the lab. I will always treasure the time we spent together.

Last but not least, I want to thank my parents, my younger brothers Andrew and Gilbert, my Glasgow friends, my old mates from undergraduate in the University of Sheffield and high school in Jakarta. Some of us might be separated by thousands of kilometres but your relentless support kept me going, wherever you were.

Working through this PhD thesis has been full of up and downs, especially with a global pandemic showing up along the way. All your support has gotten me through these challenges and drove me across the finish line.

Thank you all, truly.

# Declaration

With the exception of chapters 1 and 2, which contain introductory material, all work in this thesis was carried out by the author unless otherwise explicitly stated. On-site experimental support from NHS Scotland and Siemens Healthineers UK was received. NHS Scotland supported in ensuring the safe conduct of the work at the 7T scanner facility, while Siemens Healthineers UK provided support on scanner use.

This thesis was undertaken during the course of the COVID-19 pandemic, which severely restricted access to the 7T scanner and human imaging studies during 2020 and 2021. The project was also subject to several additional months of delay during 2021 and 2022, when the scanner was unavailable for extended periods for technical and operational reasons. The developmental and experimental work for the projects relevant for this thesis was significantly impacted as a result.



# Chapter 1

## Introduction

Magnetic resonance imaging (MRI) has developed in the past few decades to provide clinical professionals and academic researchers worldwide with a powerful tool for anatomical imaging. MRI has since become indispensable tools for radiological examinations, medical research and neuroscience studies. However, MRI is particularly sensitive to motion effects, which can degrade the acquired images to a level that is unsuitable for diagnosis, leading to extended or even repeated scans. The financial impact is also substantial, with Andre et al. (2015) estimating a loss of US\$115,000 per scanner annually [1]. Common types of artefacts observed include subject motion-related ghosting and blurring, flow effects and motion of internal organs. De-phasing and inhomogeneous signals due to main magnetic  $B_0$  or transmit  $B_1^+$  field effects can also be confounded further by motion [2]. In the past few years, 7T MRI has been gradually becoming more available for routine clinical purposes as more 7T scanners were given regulatory approval. At this field strength, there is a capacity for higher signal-to-noise ratio, which in turn can be traded for higher spatial resolution imaging. However, this potential for higher spatial resolution means motion-related ghosting and blurring effects can become more critical at 7T, such that small movements can cause major artefacts in the output image. Field fluctuations due to susceptibility changes linked to motion are also increased. There is also more image distortion effects when a subject moves. In particular, this is an issue for the longer scan times used to acquire high resolution images [3]. UHF MRI also has to contend with the issue of field inhomogeneity and signal unevenness [4], which lead to the benefits of UHF not being fully exploited. Parallel transmit imaging (pTx) is a technique that can be used to tackle these problems.

Motion correction can be performed to reduce the effects of these artefacts. Hardware- and software-based motion correction approaches have been proposed. The former group includes the usage of fixation pads, while the latter includes methods such as dynamic frequency correc-

---

tion, flow-compensated gradients, respiratory gating, cardiac triggering and retrospective motion correction. Another approach falling within the latter group is prospective motion correction, which works by adapting the image acquisition with the goal of keeping the slice position and orientation as constant as possible. PMC is used to reduce rigid-body motion effects. A common PMC approach is Prospective Acquisition Correction (PACE). PACE works by comparing a volume from a reference timepoint to successive volumes, detecting any motion that has occurred in the interval [5]. Multislice-PACE (MS-PACE) derives from PACE but uses only three slices in the echo-planar imaging (EPI) navigator volumes to estimate the motion updates [6]. This allows improved temporal resolution of motion updates while achieving the intended compensation of motion effects. This method has been successfully implemented and shown robust motion compensation with several 3T MRI routines but has yet to be implemented at 7T.

The objective of the work described in this thesis is the development of a prospective motion correction technique for routine application in 7 tesla (7T) ultra-high field (UHF) MRI, adjusting for imaging issues that are more pronounced at higher field strengths. A 7T implementation of the MS-PACE method was developed and analysed in this thesis. The wider aim is for the methods within the project could be applied to other sequence types beyond the scope of this thesis.

The following Chapter 2 describes the requisite theory covering the topics of this thesis, from nuclear magnetic resonance principles to motion correction methods in MRI.

Chapter 3 of this thesis explores the development of multislice-to-volume image registration-based PMC for 7T EPI. Firstly, the technique's limits were examined. A main element of the technique is the use of only a subset of slices for motion detection instead of a full volume, thus allowing for repeated sub-TR motion detection and correction. The effects of varying this number of slices were thus evaluated. MS-PACE's sub-TR detection capability also poses an opportunity for capturing more intra-volume motion and this was also studied. With the outcomes of these studies considered, the technique was developed further for an implementation in functional MRI (fMRI) protocols using blood level oxygen dependant (BOLD) contrast, which are often long and therefore susceptible to motion-related degradation. A novel integration of the parallel imaging technique, in-plane generalised autocalibrating partially parallel acquisitions (GRAPPA) [7] with the multislice-to-volume technique was also implemented due to the elevated spatial distortion effects in ultra high-field (UHF) imaging, including 7T [8].

In Chapter 4, following the technical development and implementation, it was evaluated in a task-based fMRI study in vivo. While an integral neuroimaging tool, fMRI suffers from various sources of noise [9], low-frequency drift [10] and long-term subject motion [11][12]. Coupled with these longer-term effects, the protocols used in task-based fMRI studies are inherently more

---

susceptible to artefacts due to the amount of physical motion. With the BOLD effect being quite small [13], motion can significantly affect subsequent data analyses. This second experimental chapter studied how the usage of MS-PACE may ameliorate these motion effects and assist functional analysis. By applying motion correction and thus acquiring more consistent datasets, reproducibility of fMRI experiments can be improved [14].

A novel integration of pTx capability with MS-PACE was implemented and the effects were studied in Chapter 5. This implementation sought to tackle the issue of  $B_1^+$  inhomogeneity that is more prominent at 7T.

Phantom and healthy subject validation experiments in vivo were performed using the Siemens MAGNETOM Terra 7T MRI scanner (Siemens Healthineers, Erlangen, Germany) at the Imaging Centre of Excellence in Glasgow, Scotland, United Kingdom. The facility houses one of the first clinical setting-located 7T MRI scanners in the UK and serves as a nexus for University of Glasgow, NHS Greater Glasgow & Clyde and industrial partners to conduct clinical imaging research. One study (Section 3.4.1) was conducted on a developmental research visit at the Fraunhofer Institute of Digital Medicine MEVIS in Bremen, Germany. Early work on developing a 7T MS-PACE navigated TSE sequence was done (preliminary images shown in Appendix B), which made it clear that a dedicated 7T development was required and provided the motivation to base further work on an in-house EPI sequence for 7T MS-PACE. This forms the work described in the Chapters 3, 4 and 5 with self-navigated EPI. A long-term goal was to develop fully 7T MS-PACE navigated TSE but this was not realised within the timeframe of this thesis.

Some of the work in this thesis has been published and presented in scientific meetings and conferences. The list is within the Published Work section, preceding the full bibliography.



# Chapter 2

## Theory

### 2.1 Nuclear magnetic resonance

While magnetic resonance imaging (MRI) was developed in 1970s, the nuclear magnetic resonance (NMR) principles underpinning it were first demonstrated in the 1940s independently by Felix Bloch [15] and Edward Purcell [16]. Since then, MRI has grown into a vital medical imaging and diagnostic tool. The lack of ionising radiation, as opposed to in X-ray, computed tomography or positron emission tomography, makes MRI attractive for routine diagnostic and research use. It utilises the NMR phenomenon, which takes advantage of the nuclear spin occurring in nuclei lacking nuclear pairing such as  $^1\text{H}$  or hydrogen. The human body has a high water content, which in turn contains an abundance of hydrogen nuclei. This property makes the human body suitable for MRI. Image generation in MRI utilises magnetic fields to generate signals from a subject or object. It takes advantage of different spin relaxation rates of tissues to create contrast. These relaxation parameters,  $T_1$  (longitudinal),  $T_2$  (transverse) and  $T_2^*$  characterise the rate of change of the magnetic spins in their respective directions.  $T_2^*$  considers the local magnetic field inhomogeneity and chemical differences in the scanned region, and the subsequent dephasing. Using pulse sequences, these characteristics are utilised to generate basic weighted images [17].

To acquire a localised image, multiple electromagnetic fields have to be applied. A standard clinical MRI scanner applies two types of electromagnetic fields. The primary static magnetic field  $B_0$  causes the nuclear spins of the hydrogen nuclei to precess at the Larmor frequency about the longitudinal  $z$  direction. A typical commercial clinical scanner typically features a  $B_0$  field of 1.5, 3 or 7 Tesla (T). Experimental and preclinical scanners are available at up to 21T [18]. Conversely, ultra-low field scanners with 0.1T and less have also been developed [19].

## 2.1. Nuclear magnetic resonance

---

After the primary field, a resonating RF pulse  $B_1^+$  is transmitted perpendicular to the  $z$  direction. This causes the magnetisation to flip at an angle away from its alignment parallel to  $B_0$ . The magnetisation now lies in the transverse  $x - y$  plane before relaxing back into the initial alignment. The magnetic flux then induces a voltage within the receive coil  $B_1^-$  and an NMR signal is recorded.

This theory section is primarily based on the key texts of [20][21][22][23]. Further sources is referenced accordingly following the content.

### 2.1.1 Nuclear spin

The phenomenon of nuclear spin occurs when the number of protons, the number of neutrons, or the number of both are odd. The absence of nuclear pairing results in a nucleus with a net spin. Spin quantum number,  $I$ , characterises this angular momentum.  $I$  can take the value of any non-negative full and half integer. This phenomenon was first described by Pauli in 1924 [24]. An example of a nucleus with a half integer  $I$  is  $^1\text{H}$  or hydrogen. As it has just one proton in its nucleus, its corresponding  $I$  is  $1/2$ . Due to its abundance within the human body, hydrogen has a special importance in MRI.

The aforementioned absence of nuclear pairing gives rise to a spin angular momentum  $S$  in the nucleus, which can be characterised by the equation below:

$$\vec{S} = \hbar \vec{I} \quad (2.1)$$

where  $\hbar$  is the reduced Planck constant, which is the Planck constant divided by  $2\pi$ .  $\hbar$  relates the particle's energy to its angular frequency.  $\vec{S}$  also has a  $z$  component which is expressed by:

$$\vec{S}_z = \hbar m \quad (2.2)$$

where  $m$  is the magnetic quantum number, which has total possible values of  $2I + 1$ . For the  $^1\text{H}$  nuclei of  $I = \frac{1}{2}$ , the possible  $m$  values are  $-\frac{1}{2}$  and  $\frac{1}{2}$ . These also govern the spin angular momentum orientation.

The spinning charge in the nucleus from the protons and neutrons means it now has an intrinsic magnetic moment. This then gives rise to a magnetic field around its spinning axis with its own magnetic dipole moment  $\vec{\mu}$ .

$$\vec{\mu} = \gamma \vec{S} \quad (2.3)$$

where the gyromagnetic ratio  $\gamma$  is a constant that varies depending on the nucleus. For the hydrogen  $^1\text{H}$  nucleus, the  $\gamma$  is valued at  $42.58 \times 2\pi \text{MHzT}^{-1}$ .

The  $z$  component of  $\vec{\mu}$  is expressed by:

$$\vec{\mu}_z = \gamma \vec{S}_z = \gamma \hbar m \quad (2.4)$$

When an external magnetic field  $\vec{B}_0$  is introduced, the magnetic moment  $\vec{\mu}$  will tend to align with the vectors of  $\vec{B}_0$  [20]. Due to the spin angular momentum, the nucleus experiences a torque that results in rotational motion about the field vectors of  $\vec{B}_0$  called precession, which is shown in Figure 2.1. The precession occurs at the frequency called the Larmor frequency,  $\omega_L$ . This relationship can be described as below:

$$\omega_L = -\gamma \vec{B}_0 \quad (2.5)$$

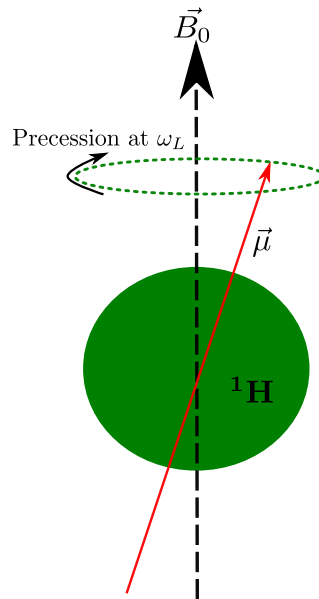


Figure 2.1: The precession of the magnetic moment  $\vec{\mu}$  of hydrogen around the static, external magnetic field  $\vec{B}_0$  at the Larmor frequency  $\omega_L$ . The sense of rotation is shown for nuclei, such as protons, with a positive gyromagnetic ratio.

### 2.1.2 Boltzmann distribution

Due to the Zeeman effect, the hydrogen nucleus' spins have two possible discrete energy states, either parallel ("spin-up") or anti-parallel ("spin-down") to the direction of  $\vec{B}_0$ . The alignment of

## 2.1. Nuclear magnetic resonance

these spins are governed by the strength of  $\vec{B}_0$  and their thermal energy. It is energetically expedient to align with the external field and thus the lower energy spins are parallel to it. Conversely, higher energy spins are able to oppose the field and will be anti-parallel to it. This expediency means the majority of spins are in parallel to  $\vec{B}_0$  while in equilibrium. As illustrated in Figure 2.2, the energy requirement for opposing the field is proportional to the external magnetic field strength.

The Boltzmann distribution can determine the probability of each hydrogen spin adopting either energy state. If  $n_i$  is the number of lower energy spins and  $n_j$  is the number of the high energy spins, then the predicted equilibrium distribution is:

$$\frac{n_i}{n_j} = e^{(\Delta E/kT)} \quad (2.6)$$

where  $\Delta E$  is the energy differential between the two energy states,  $k$  is the Boltzmann constant ( $k = 1.381 \times 10^{-23} JK^{-1}$ ) and  $T$  is the absolute temperature (in Kelvin).  $\Delta E$  itself can be expressed as following:

$$\Delta E = \gamma \hbar B_0 \quad (2.7)$$

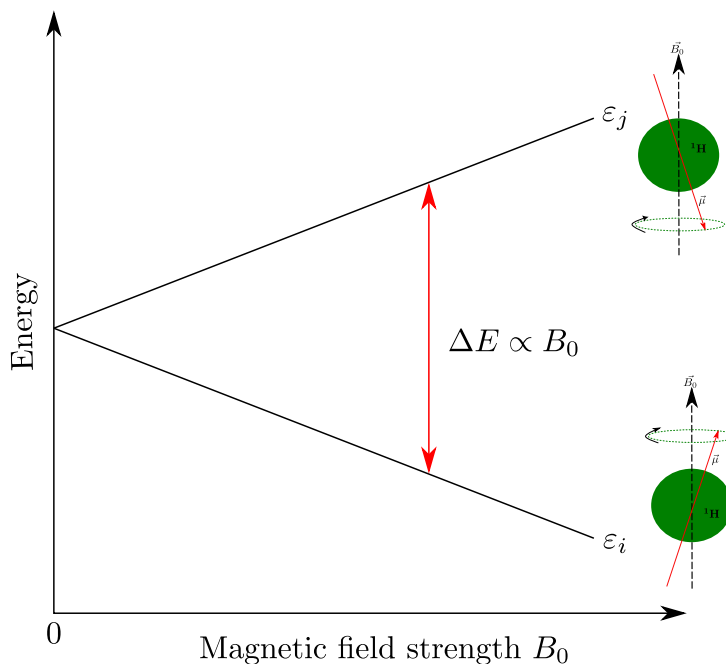


Figure 2.2: The energy level diagram for hydrogen ( $I=1/2$ ) when subjected to an external field  $B_0$ , illustrating the Zeeman splitting.  $\Delta E$  is the energy differential between the two energy states.

Summing the effects of all the spins within the area of interest results in a net magnetisation  $\vec{M}$ , which is parallel to the  $\vec{B}_0$  field.  $\vec{M}$  can be represented as a sum of the magnetic moment  $\vec{\mu}$  vectors.

$$\vec{M} = \Sigma \vec{\mu} \quad (2.8)$$

While the magnetic moments all precess about the  $\vec{B}_0$  field vectors, the phases of the individual nuclei are randomly distributed and thus cancel each other, assuming the system is in thermal equilibrium. There remains the longitudinal net magnetisation  $M_0$  in the  $\vec{B}_0$  direction, which for  $N_s$  number of spins at equilibrium can be estimated as below:

$$M_0 \approx N_s \frac{\hbar^2 \gamma^2 B_0}{4kT} \quad (2.9)$$

It can be seen that the  $M_0$  is proportional to the number of spins  $N_s$  and  $B_0$ . This is relevant to the generation of an NMR signal when subjected to radiofrequency pulses, which will be described in a later section.

### 2.1.3 Laboratory and rotating frames of reference

At thermal equilibrium, the net magnetisation  $\vec{M}$  is completely aligned with the z or longitudinal axis, in the direction of  $\vec{B}_0$ . However, a signal can only be generated if this magnetisation is perturbed from its equilibrium and flipped away towards the x-y or transverse plane. Magnetic resonance is used for this purpose. Resonance occurs when a nucleus is subject to energy oscillating at, or near, its Larmor (resonant) frequency  $\omega_L$ . Exposed to such external energy, the nucleus will be able to gain energy. On a quantum level, this means lower energy state nuclei gains energy and thus are able to transit into a higher energy state. The active component of the resultant magnetic field  $\vec{B}_1$  is applied perpendicular (but not precisely) to the static  $\vec{B}_0$  field. The combination of all the field effects and its effect on the magnetisation can then be related as:

$$\frac{d\vec{M}}{dt} = \gamma(\vec{M} \times \vec{B}) \quad (2.10)$$

To describe this phenomenon, two different frames of reference can be used: the laboratory and the rotating frames of reference. The laboratory frame is stationary. In this frame of reference, the longitudinal z-axis is set on the direction of the static, external magnetic field  $\vec{B}_0$ . The transverse x-y plane is then established normal to the z-axis and thus the  $\vec{B}_0$  field. This stationary frame of reference, however, is not an easy way to observe the complex motion that occurs during the application of an RF pulse. This is where a rotating frame of reference can be

## 2.1. Nuclear magnetic resonance

useful in illustrating this phenomenon.

In the rotating frame of reference, the z-axis remains in the same direction (the direction of  $\vec{B}_0$ ). The difference is the x-y plane rotates around the z-axis at the Larmor frequency of the subject nucleus. Consequently, a simplified picture of the precession is created. The rotating frame essentially excludes the effect of  $\vec{B}_0$  and the precession of the net magnetisation  $\vec{M}$ . The previously-rotating  $\vec{B}_1$  field is now static with the respect to the frame. This is illustrated in Figure 2.3. For the rotating frame of reference, the axes are referred to as  $x'$ ,  $y'$  and  $z'$ . The two coordinate systems can be linked with a rotation matrix  $R$ :

$$\begin{bmatrix} x' \\ y' \\ z' \end{bmatrix} = R \begin{bmatrix} x \\ y \\ z \end{bmatrix} = \begin{bmatrix} \cos(\omega_L t) & -\sin(\omega_L t) & 0 \\ \sin(\omega_L t) & \cos(\omega_L t) & 0 \\ 0 & 0 & 1 \end{bmatrix} \begin{bmatrix} x \\ y \\ z \end{bmatrix} \quad (2.11)$$

where  $\omega_L$  is the Larmor frequency and also the frequency of the rotating frame. As the z-axis is unchanged in both systems ( $z = z'$ ), there is no transformation along that axis.

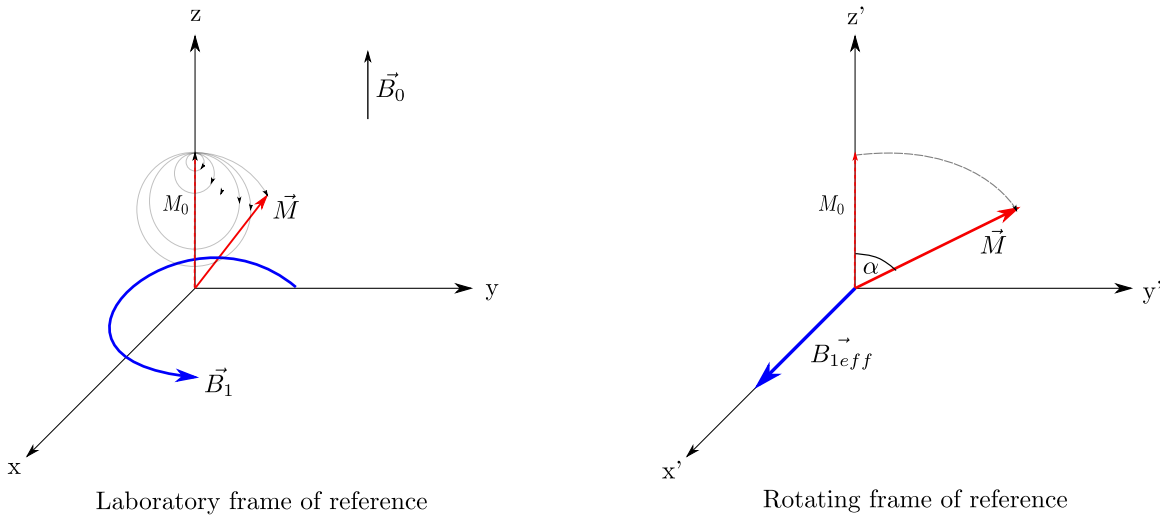


Figure 2.3: Magnetisation as viewed using the laboratory (left) and rotating (right) frame of reference.  $B_{1\vec{eff}}$  is the effective  $\vec{B}_1$  in the rotating frame of reference.

As observed in the rotating frame of reference in Figure 2.3, the applied  $\vec{B}_1$  field causes the magnetisation  $\vec{M}$  to be perturbed from its equilibrium state in the static field  $\vec{B}_0$  direction towards the x-y plane. This angle between  $\vec{M}$  and its former alignment with  $\vec{B}_0$  is called the flip angle ( $\alpha$ ), which for a fixed amplitude can be characterised as:

$$\alpha = \gamma B_1 t \quad (2.12)$$

in which  $t$  is the duration of the applied  $\vec{B}_1$  field. When a net magnetisation with magnitude  $M_0$  on the z-axis is subjected to an RF excitation and a corresponding  $\vec{B}_1$  field on the x-axis, the net magnetisation  $\vec{M}$  in the rotating frame of reference can be disentangled to its axial components as following:

$$M_x = 0 \quad (2.13)$$

$$M_y = M_0 \sin(\alpha) \quad (2.14)$$

$$M_z = M_0 \cos(\alpha) \quad (2.15)$$

Therefore, the net magnetisation  $\vec{M}$  has now moved towards the y-z plane in the rotating frame of reference. Following Faraday's law, the precession of the magnetisation  $\vec{M}$  in the laboratory frame of reference then induces a voltage that can be recorded as an NMR signal in the RF receive coil.

### 2.1.4 Relaxation times and contrast

The magnetisation does not remain in its post-perturbation state when the  $\vec{B}_1$  field is removed. The magnetisation gradually evolves back to its equilibrium state. This gradual return is driven by spin-lattice (also called  $T_1$  and longitudinal) relaxation, and spin-spin (also called  $T_2$  and transverse) relaxation.

#### $T_1$ relaxation

Energy starts being released from the spins after excitation. The spins begin transferring energy to its environment (thus lattice). Consequently, the longitudinal component of the magnetisation  $M_z$  gradually returns to its non-excited, thermally-stable state  $M_0$ . The time constant  $T_1$  characterises this behaviour.  $T_1$  is defined as the time it takes for 63% of the equilibrium longitudinal magnetisation to be recovered. This is equivalent to  $1 - \frac{1}{e}$  of  $M_0$ . Figure 2.4 displays the longitudinal relaxation after an excitation with a  $90^\circ$  RF pulse.

This recovery of longitudinal magnetisation as function of time can then be mathematically formulated:

$$M_z(t) = M_0(1 - e^{-\frac{t}{T_1}}) \quad (2.16)$$

We can also relate the rate of the longitudinal magnetisation regrowth to  $T_1$ . This rate is proportional to the difference between  $M_0$  and  $M_z(t)$ :

$$\frac{dM_z(t)}{dt} = \frac{M_0 - M_z(t)}{T_1} \quad (2.17)$$

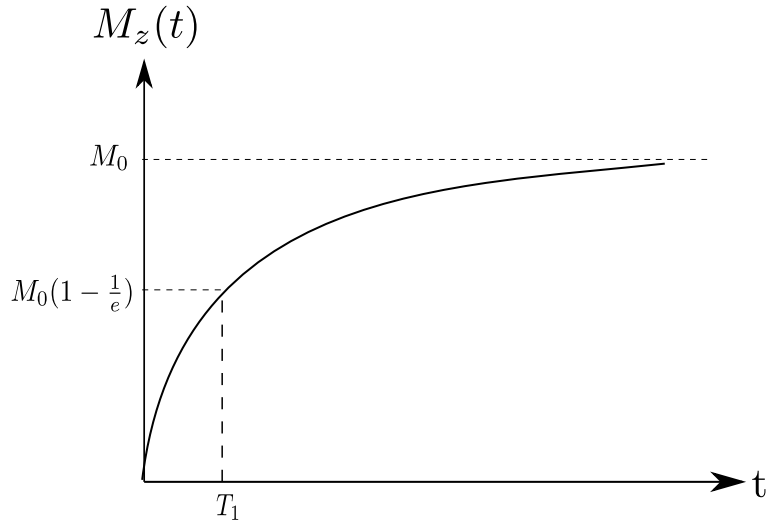


Figure 2.4: Longitudinal relaxation after an excitation with a  $90^\circ$  RF pulse. The time constant  $T_1$  is equivalent to 63% ( $\approx 1 - \frac{1}{e}$ ) of the maximum longitudinal magnetisation ( $M_0$ ).

The size of  $T_1$  and the relaxation efficiency largely depend on the  $\vec{B}_0$  field strength and magnetic field fluctuations from surrounding molecular dynamics. These molecular dynamics are characterised by a molecular tumbling rate or correlation time,  $\tau_c$ , which is the time required for the molecule to rotate by approximately 1 radian. When  $\tau_c$  is close to the Larmor frequency  $\omega_L$ , longitudinal relaxation is optimum and thus the  $T_1$  value is minimised. This implies that at higher  $\vec{B}_0$  field strengths (e.g. 7 Tesla), where the corresponding  $\omega_L$  is higher, the difference between  $\tau_c$  and  $\omega_L$  is bigger. Consequently, the relaxation is less optimum and the  $T_1$  also increases.

### $T_2$ relaxation

Along with the longitudinal/ $T_1$  relaxation, the transverse magnetisation  $M_{xy}$  starts to gradually decay due to magnetic field interactions with surrounding spins. These interactions disrupt the magnetic moments of the spins and their precessional frequencies, leading to dephasing.  $M_{xy}$  then eventually returns to its equilibrium value, which is zero. This relaxation is characterised by the  $T_2$  constant, which is the time required for the transverse magnetisation to decay to 37% of its original value. This is equivalent to  $\frac{1}{e}$  of  $M_{xy}(0)$ . Figure 2.5 displays the transverse relaxation after an excitation with a  $90^\circ$  RF pulse.

This recovery of transverse magnetisation as function of time can then be mathematically formulated as:

$$M_{xy}(t) = M_{xy}(0)(e^{-\frac{t}{T_2}}) \quad (2.18)$$

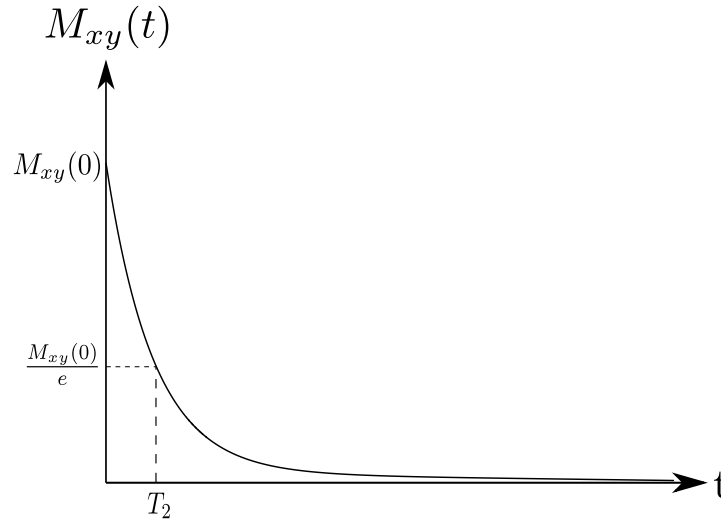


Figure 2.5: Transverse relaxation after an excitation with a  $90^\circ$  RF pulse. The time constant  $T_2$  is equivalent to 37% ( $\approx \frac{1}{e}$ ) of the initial transverse magnetisation ( $M_{xy}$ ).

We can also relate the rate of the transverse magnetisation decay to  $T_2$ . This rate is proportional to the  $M_{xy}(t)$ :

$$\frac{dM_{xy}(t)}{dt} = -\frac{M_{xy}(t)}{T_2} \quad (2.19)$$

### $T_2^*$ relaxation

In the real world, the real transverse magnetisation decay ends up being faster than the  $T_2$  time constant due to additional spatially dependent dephasing caused by  $\vec{B}_0$  inhomogeneities due to varying susceptibility values across the sample (or within an imaging voxel). Instrumental factors, such as local field gradients generated by eddy currents can contribute to this dephasing process. This extra decay can be represented by the time constant  $T_{2i}$ . Both of these dephasing effects can be combined and described by the time constant  $T_2^*$ . The dephasing-influenced signal decay results in a characteristic oscillating profile called the free induction decay (FID), shown in Figure 2.6.  $T_2^*$  is related to the two former time constants as:

$$\frac{1}{T_2^*} = \frac{1}{T_2} + \frac{1}{T_{2i}} \quad (2.20)$$

These relaxation time constants are tissue-varying and the knowledge of them is vital in designing NMR or MRI sequences. An image of desired contrast can be acquired by adeptly using these properties.

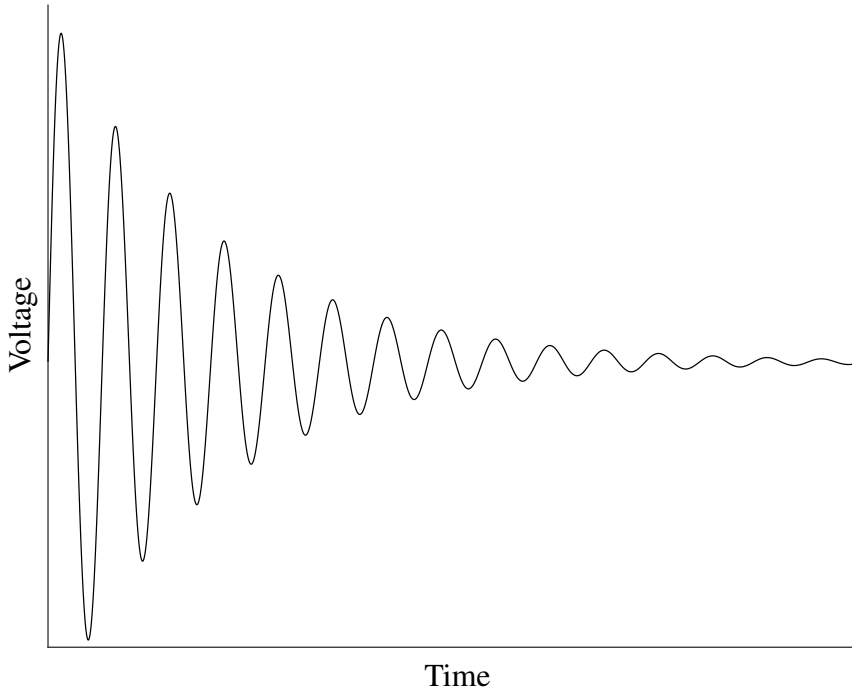


Figure 2.6: The free induction decay (FID) signal with its characteristic exponential decay.

### 2.1.5 Bloch equations

The relaxation time constants can be used to describe macroscopically the net magnetisation  $\vec{M}$  in the Bloch equations. These equations were introduced in 1946 in a seminal paper on nuclear induction by physicist Felix Bloch [15]. These equations are a way to mathematically simulate the evolution of magnetisation in an NMR experiment. The equations for the laboratory frame of reference are as follows:

$$\frac{dM_x}{dt} = \gamma(\vec{M}(t) \times \vec{B}(t))_x - \frac{M_x}{T_2} \quad (2.21)$$

$$\frac{dM_y}{dt} = \gamma(\vec{M}(t) \times \vec{B}(t))_y - \frac{M_y}{T_2} \quad (2.22)$$

$$\frac{dM_z}{dt} = \gamma(\vec{M}(t) \times \vec{B}(t))_z - \frac{M_z - M_0}{T_1} \quad (2.23)$$

where  $\vec{B}(t)$  is the resultant of the main (static) magnetic field and the dynamic magnetic field component generated by an applied RF transmit pulse if present.

## 2.2 Image formation

To simply excite the nuclear spins and acquire the NMR signals is not sufficient to produce a spatially-encoded image. In order to localise the signal spatially within the required 3D volume, magnetic field gradients are applied across the measured volume. While these fields are applied along the z-direction (the same as the  $\vec{B}_0$  field), their magnitudes vary linearly along the x, y and z-axes. These gradients  $G_x$ ,  $G_y$  and  $G_z$  spatially modulate the Larmor frequency and encode the locations of the NMR signals for precise reconstruction into an image. A resultant gradient vector can then be formulated by superimposing these orthogonal gradients:

$$\vec{G} = G_x + G_y + G_z = \frac{dB_z}{dx} + \frac{dB_z}{dy} + \frac{dB_z}{dz} \quad (2.24)$$

### 2.2.1 Slice-selection gradients

In order to selectively acquire a slice for imaging, a slice-selection gradient is applied along the z-direction while a bandwidth-specific RF pulse is applied. The gradient application causes the resonant frequencies to now linearly vary along the z-axis. Note that the slice-selection gradient is assigned to the z-axis by convention, but can in practice be orientated in any direction in 3D space. The simultaneously-applied RF pulse has a specific envelope that contains a defined band of frequencies around a centre frequency  $\omega_c$ , which is in turn determined by its position along the z-axis:

$$\omega_c = \gamma(B_0 + zG_z) \quad (2.25)$$

Assuming a perfect excitation, this pulse will only excite a set of spins within the pulse's bandwidth  $\Delta\omega$ . As a result, a thin slice of thickness  $\Delta z$  is excited. This process is illustrated in Figure 2.7.

$$\Delta\omega = \gamma G_z \Delta z \quad (2.26)$$

A basic example of a shaped envelope RF excitation pulse is the sinc pulse (shown in Figure 2.8). To excite a very exact band of frequencies and thus an ideal slice with a rectangular profile, the sinc pulse has to be transmitted for an infinite amount of time. As this is impractical, a sinc pulse is truncated to a limited number of side lobes.

At the end of the slice-selection gradient, a negative gradient lobe (also called rephasing gradient) is applied to cancel the dephasing effects of the preceding/positive selection gradient. The size of this rephasing gradient is typically half the size of slice-selection gradient. It is also notable that the gradients do not form a rectangular shape, but instead a trapezoidal shape. This

## 2.2. Image formation

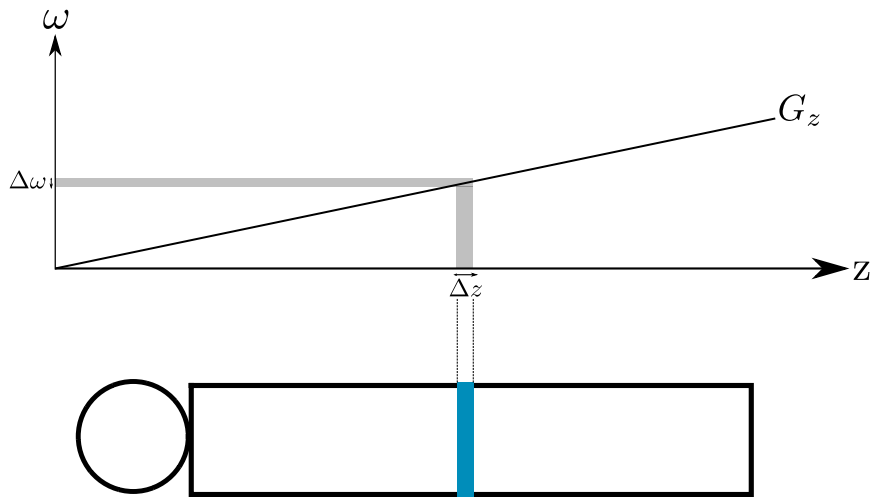


Figure 2.7: A slice of specified thickness  $\Delta z$  excited by the slice-selection gradient  $G_z$  and an RF pulse containing the defined resonant frequency bandwidth  $\Delta\omega$ .

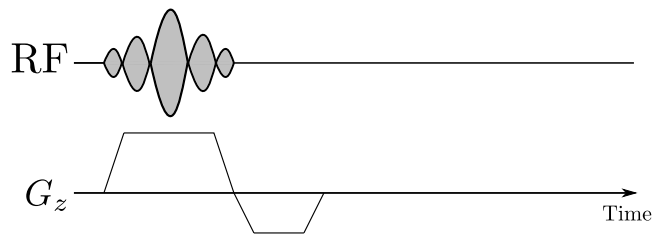


Figure 2.8: A pulse diagram showing a sinc-shaped RF excitation pulse along with the slice-selection gradient and its corresponding rephasing gradient.

is due to the inherent limitation on the gradient slew rate achievable by MRI scanners, which means ramping the gradients up or down take some time.

### 2.2.2 Spatial encoding and k-space

#### Frequency encoding

The magnetic field gradient creates a distortion of the magnetic field experienced at the different positions along the corresponding gradient axis, which, by convention, is usually assigned to be the x-axis. These variations mean the spins across the axis now spin on varying frequencies. Thus, the resonant frequency of a spin is now a linear function of its spatial position. This feature can then be exploited to provide precise spatial locations of acquired NMR signals in the x-direction. This process is called frequency encoding. The gradient experienced across the x-axis itself is also referred to as the readout gradient. At the centre of the gradient coil or  $x = 0$ ,

the gradient effect is zero and thus only the effect of  $\vec{B}_0$  is experienced there. Data are sampled during application of the frequency-encoding gradient.

### Phase encoding

An additional spatial encoding gradient is also applied perpendicularly to the slice-selection and frequency-encoding gradient (assigned to the y-axis by convention). As a result, the spins across this direction also become altered momentarily. The resonant frequencies then return to their original Larmor frequency shortly after the gradient is switched off. However, the spins retain a spatially-dependent phase shift that is proportional to the strength and duration of the applied gradient. This process, illustrated in Figure 2.9, can thus be called phase encoding. In contrast to frequency encoding, data are not sampled during application of the phase-encoding gradient.

### K-space

These encoding processes can then be used to create a raw data map in the spatial frequency domain, also known as k-space.  $G_x$  and  $G_y$  are used to acquire signal information across the  $k_x$  and  $k_y$  directions respectively, where the individual k-space values are given by:

$$k_x = \frac{\gamma}{2\pi} \int_0^{t_x} G_x(t) dt \quad (2.27)$$

$$k_y = \frac{\gamma}{2\pi} \int_0^{t_y} G_y(t) dt \quad (2.28)$$

where  $t_x$  and  $t_y$  are the duration of the application of the x and y-axes gradients respectively.

We can now also formulate the spatially-varying phase with its respective location on  $(k_x, k_y)$ , compared to the value at the centre of the gradient coil:

$$\phi(x, y) = 2\pi(xk_x + yk_y) = \gamma \left( \int_0^{t_x} G_x(t) dt + \int_0^{t_y} G_y(t) dt \right) \quad (2.29)$$

To cover the entirety of k-space, the encoding must traverse the domain in several steps. This process is illustrated in Figure 2.10 with a Cartesian acquisition pattern. The encoding must also fulfil the Nyquist-Shannon sampling requirement, which means the sizes of the frequency ( $\Delta k_x$ ) and phase ( $\Delta k_y$ ) encoding steps in the k-space are equal to the inverse of the field of view (FOV) of the acquired MR image [25][26]:

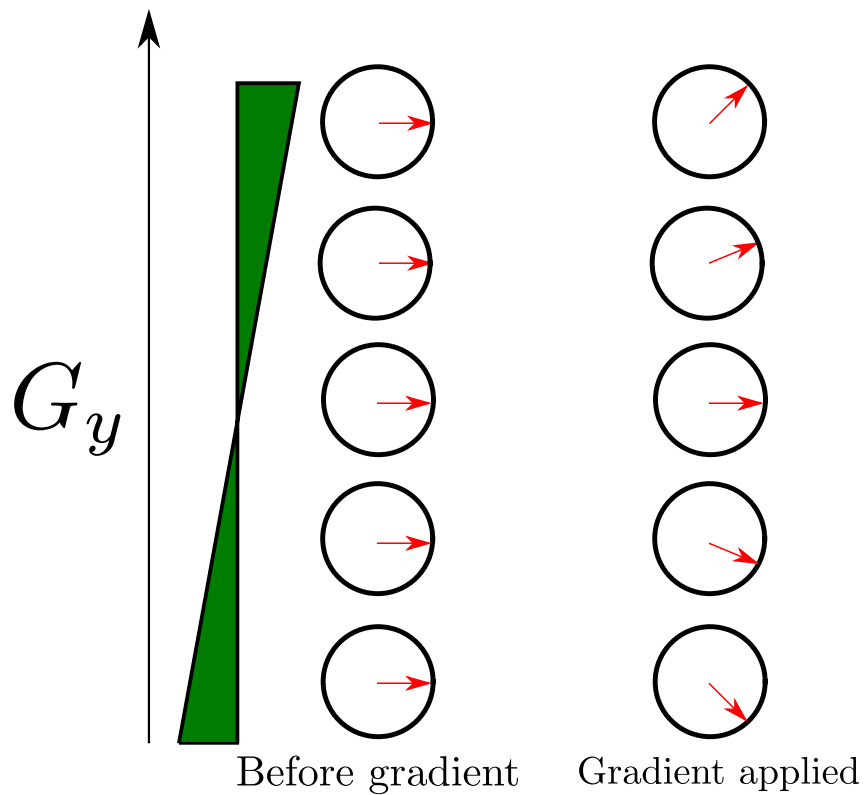


Figure 2.9: The application of a phase encoding gradient causes the spins across the sample to precess at varying frequencies. While these return to the Larmor frequency after the gradient has passed, each spin now possesses a unique phase angle.

$$\Delta k_x = \frac{1}{FOV_x} \quad (2.30)$$

$$\Delta k_y = \frac{1}{FOV_y} \quad (2.31)$$

The process starts with the frequency and phase encoding gradients being applied to signals from a line in k-space. In the following readout, the same frequency encoding gradient is then applied with a phase encoding gradient of a different strength to cover another line. This is then repeated until all the required k-space lines are acquired. Data sampling is applied during frequency encoding and after phase encoding.

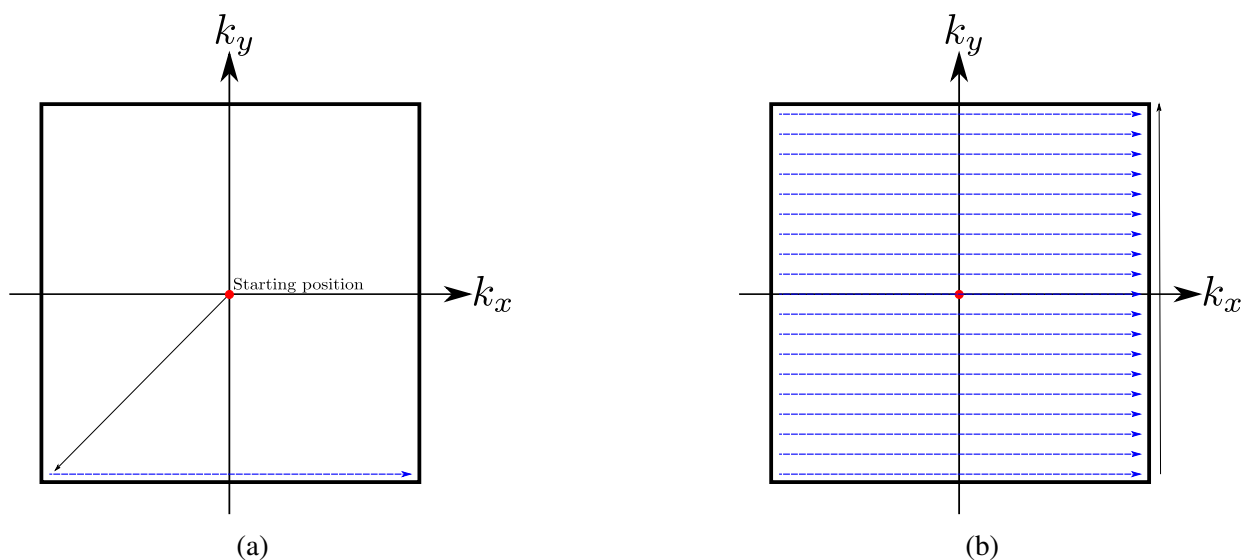


Figure 2.10: Example of a Cartesian k-space acquisition pattern. Firstly (in a), the frequency and phase encoding gradients are applied to shift the encoding to the corner of the k-space from the centre (red dot). Readout is started and the frequency encoding gradient is then applied to acquire the first line of k-space. Then, a new combination of phase encoding gradient and frequency prephase gradient is applied to start another k-space line acquisition. The process is repeated until all the lines are acquired (in b).

### 2.2.3 Gradient echo

The eventual decay of the FID signal as shown in Figure 2.6 means that there is a limited amount of time available to acquire perform the relevant encoding. However, a gradient of opposing polarity can be applied to recover the FID signal. The first step in gradient echo acquisition involves an application of a dephasing gradient. This dephaser is high strength and of a negative polarity. Resonant frequencies of spins shift and the FID starts to dephase and decay more rapidly. Immediately after this process, a positive rephasing gradient is applied. The rephaser realigns the spins dispersed by the dephaser and frequency information can be encoded. This signal or echo is called the gradient echo. The rephaser also has half of the zero-order moment with the dephaser. Maximum signal is reached at the point where the rephaser's area matches the dephaser's. Figure 2.11 displays how this technique is applied by means of a pulse diagram.

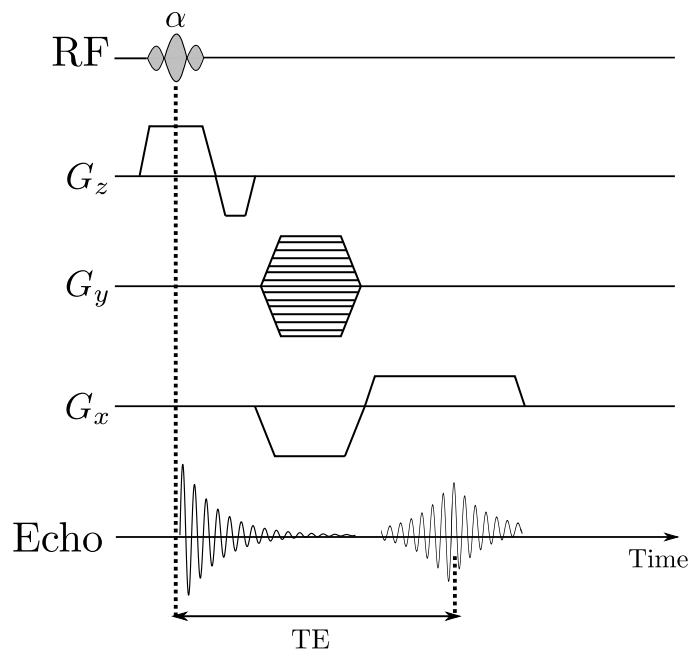


Figure 2.11: A basic gradient echo sequence. After an initial low flip angle  $\alpha$  RF pulse (typically less than  $90^\circ$  in a fast low angle shot or FLASH gradient echo sequence [27]), a dephasing readout gradient ( $G_x$ ) is applied. A rephasing gradient then immediately follows. The phase encoding gradient ( $G_y$ ) is applied in steps in order to acquire the entire image. At the echo time (TE), a gradient echo forms and can be acquired. Data sampling is applied during the frequency-encoding gradient.

### 2.2.4 Spin echo

Another basic pulse sequence technique for signal acquisition is based on the spin echo. The discovery of the spin echo phenomenon by Erwin Hahn in 1949 [28] is one of the most important discoveries in the history of NMR and paved the way for its eventual imaging application. A spin echo is generated by the application of two RF pulses, generally a  $90^\circ$  initial pulse followed by a  $180^\circ$  refocusing pulse. After the magnetisation vectors dephase and the FID signal decays, the refocusing pulse is applied. The spins then start to rephase with the slower precessing spins now ahead of the faster spins. The result is then a refocused signal in the form of the spin echo. A maximum signal is obtained at the echo time (TE), which is at the centre of the echo. Figure 2.12 displays how this technique is applied in the form of a pulse diagram. The signal eventually decays again, but additional RF refocusing pulses can be used to retrieve more signals. This is discussed in a later section.

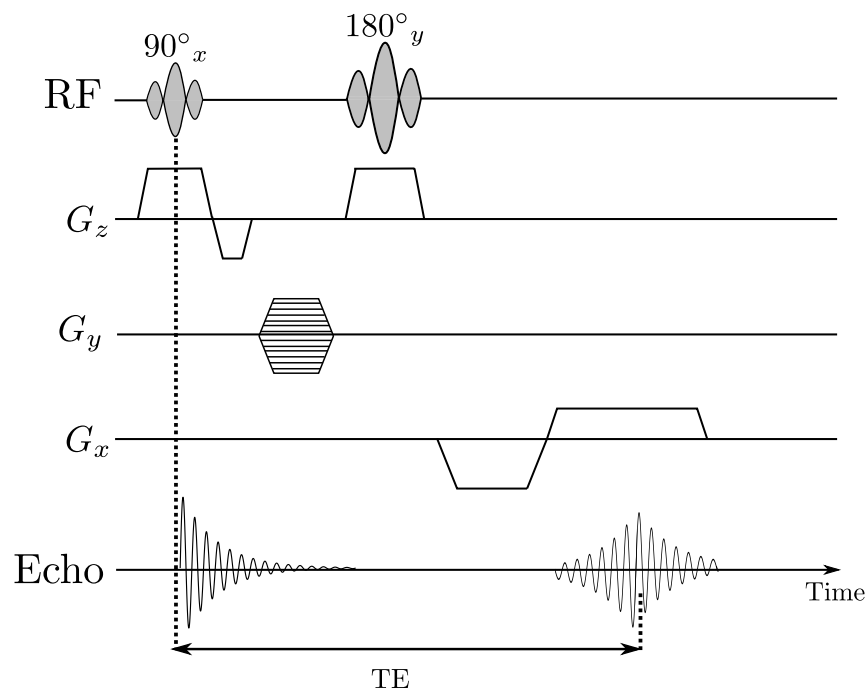


Figure 2.12: A basic spin echo sequence. After an initial RF pulse and eventual decay of the signal, a  $180^\circ$  refocusing RF pulse is applied. A spin echo forms, which is at its peak at the echo time (TE).

### 2.2.5 Image reconstruction

In the processes described in Section 2.2.2, spatial encoding is used to map MR signals acquired from a sample or subject. However, this information, which is in the spatial frequency or k-space domain, is not sufficient to be presented as a visually useful MR image. A further processing of this k-space information is required. The k-space contains information from a range of spatial frequencies. Lower spatial frequency information lies in the vicinity of the centre of k-space. This area contains the general information regarding the contrast of the received signal. Meanwhile, higher spatial frequency information are stored in the outer areas of the k-space. Contributions to the image sharpness and finer details are contained in this area. As the spatial frequencies in k-space  $S(k_x, k_y)$  and the pixel location of the MR image  $s(x, y)$  are a Fourier transform pair, the frequency  $k_x$  and phase  $k_y$  information can be converted into an MR image using a two-dimensional Fourier transform (2D FT). The acquired signal including its spatially-varying phase information can be represented in k-space as follows:

$$S(k_x, k_y) = \iint s(x, y) e^{-i2\pi(k_x x + k_y y)} dx dy \quad (2.32)$$

Applying an inverse Fourier transform, the MR image can be reconstructed from this k-space information:

$$s(x, y) = \frac{1}{(2\pi)^2} \iint S(k_x, k_y) e^{i2\pi(k_x x + k_y y)} dk_x dk_y \quad (2.33)$$

However, in practice, as the overall signal is acquired in discrete, quantised samples instead of continuously, a discrete form of the inverse Fourier transform (2D-IDFT) is instead performed to reconstruct the k-space information. If  $N_x \times N_y$  discrete data points were acquired, then the transform equation becomes:

$$s(x, y) = \frac{1}{N_x N_y} \sum_{k_x=0}^{N_x-1} \sum_{k_y=0}^{N_y-1} S(k_x, k_y) e^{i2\pi(\frac{k_x x}{N_x} + \frac{k_y y}{N_y})} \quad (2.34)$$

### 2.2.6 Parallel imaging acquisition and reconstruction

Today, MRI coils are often equipped with a large number of receive elements (32 and 64 are typical) as shown in Figure 2.14. This feature can be used for parallel imaging acquisition and reconstruction. Parallel imaging techniques enable expedited acquisitions without having to increase gradient slew rates significantly and thus avoid limitations due to potential safety issues [30] or available gradient performance. Two widely-used parallel imaging techniques are

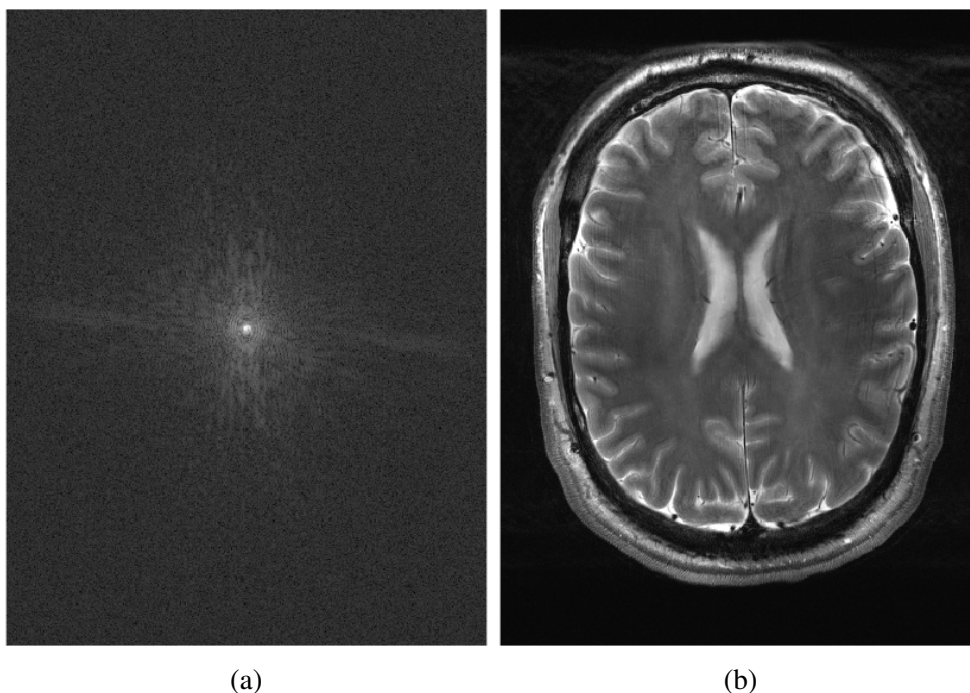


Figure 2.13: (a) The representation of an image acquired using turbo spin echo (TSE) in the k-space domain and (b) the actual image after a 2D inverse discrete Fourier transform is performed on the k-space data. This sequence type was originally published under the name RARE [29].

GRAPPA (generalised autocalibrating partial parallel acquisition) [7] and SENSE (sensitivity encoding) [31], which are applied in k-space and image space respectively. This section focuses on the usage of GRAPPA, which was used in the work described in this thesis.

GRAPPA claims its ancestry to the earlier k-space parallel imaging technique autocalibrating SMASH (simultaneous acquisition of spatial harmonics) [7]. It speeds up acquisition of each slice (in-plane) by acquiring only a reduced number of k-space phase encoding lines but with the centre fully-sampled, which forms the autocalibration signal (ACS) region. Reconstructing this partially-sampled k-space straight away violates the Nyquist requirement and creates image ghosts. However, by exploiting spatially-varying receive coil sensitivities, a full, unaliased image can still be obtained.

The process of reconstructing a GRAPPA-acquired image goes through several steps, illustrated in Figure 2.15. GRAPPA uses the information from all  $C$  receive coils. To reconstruct an unsampled  $k_y$  line in a specific coil  $a$  on line  $k_y - n\Delta k_y$  distanced from the ACS ( $n$  being an integer), first the GRAPPA coefficients from each of the receive coils are calculated using the ACS lines. A linear fitting using the fully-sampled centre ACS region  $S_c^{ACS}$  is performed to calculate

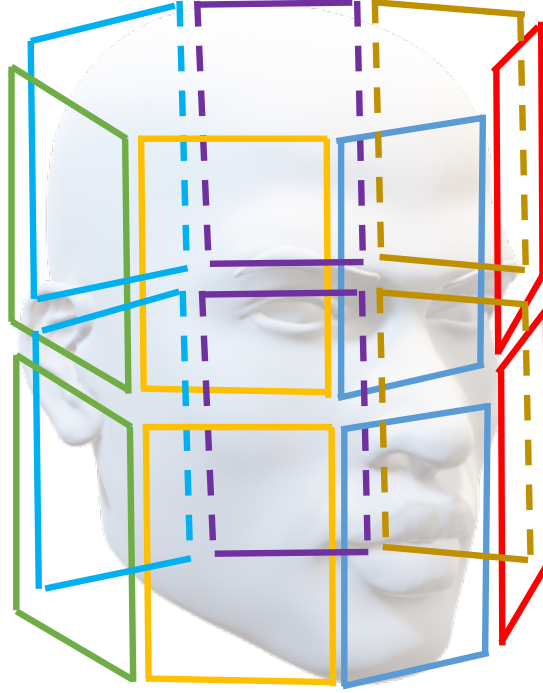


Figure 2.14: Representation of receive coil array for use in parallel imaging acquisition.

GRAPPA coefficients:

$$\sum_{c=1}^C S_c^{ACS}(k_y - x\Delta k_y) = \sum_{c=1}^C w_{a,c} S_a(k_y) \quad (2.35)$$

with  $w_{a,c}$  being the coil-wise GRAPPA coefficient, which are then used to estimate the unsampled data in the outer region of k-space.

A sliding block reconstruction is then used to reconstruct the unsampled k-space points. Each sliding block consists of a group of surrounding lines and thus each missing line can be reconstructed with several possible blocks surrounding it. Using combined available data from all  $C$  coils  $B$  number of sliding blocks (weighted by the expanded GRAPPA coefficients  $w_{a,c,n,b}$ ) and acceleration factor  $A$ , the unsampled  $k_y$  line can be reconstructed:

$$S_a(k_y - n\Delta k_y) = \sum_{c=1}^C \sum_{b=0}^{B-1} w_{a,c,n,b} S_a(k_y - BA\Delta k_y) \quad (2.36)$$

The process of calculating all the missing k-space lines into a fully-sampled k-space map  $S_c^{fs}$  can also be represented as a convolutional process of the partially-sampled k-space map  $S_c^{ps}$

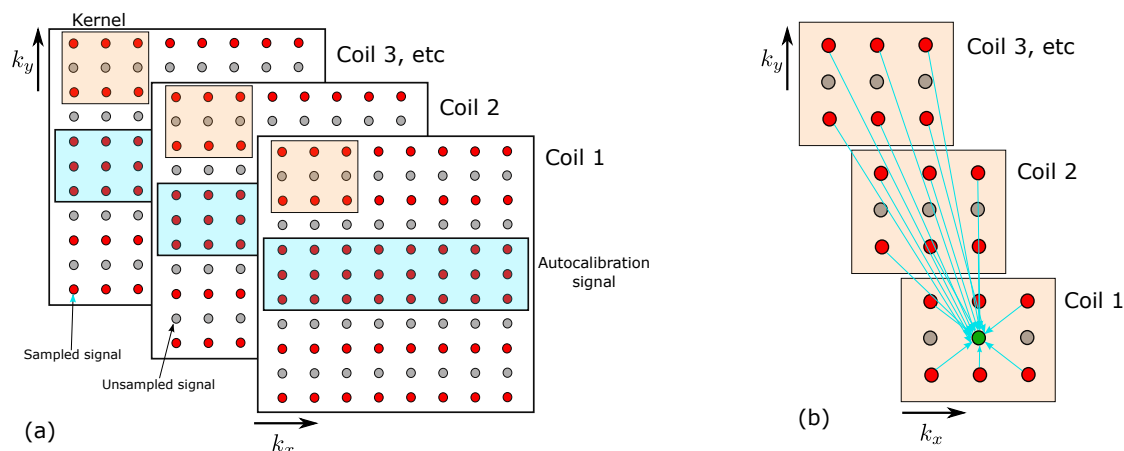


Figure 2.15: Calculation of unsampled data points in GRAPPA. First, as in (a), GRAPPA coefficients are calculated from the autocalibration signal lines in each receive coil. Using these coefficient, unsampled data points can be calculated from its neighbouring sampled points in all coils as illustrated in (b).

with the GRAPPA weight kernel  $w_{kc}$  of line  $k$  and coil  $c$  across all  $C$  receive coils.

$$S_c^{fs} = \sum_{c=1}^C w_{kc} \otimes S_c^{ps} \quad (2.37)$$

After this process is iterated across all the unacquired  $k$ -space lines, the data from each receive coil is inverse Fourier transformed into conventional coil-wise images  $s_c(x, y)$ . These images are then combined using the basic sum-of-squares method or with a sum weighted by the coil sensitivity variance [32]. Combining all the coil images results in the final image  $s(x, y)$  using the former method:

$$s(x, y) = \sqrt{\sum_{c=1}^C |s_c(x, y)|^2} \quad (2.38)$$

It is crucial that the unacquired lines are calculated and filled in. Reconstructing the undersampled  $k$ -space flouts the Nyquist-Shannon sampling requirement, which results in aliasing (shown in Figure 2.16).

GRAPPA has a special relevance in ultra high-field (UHF) strength imaging, especially for echo planar imaging or EPI (which itself is described further in Section 2.3.1). With EPI, the degree of spatial distortions increases the  $B_0$  field strength, the effective echo spacing and the extent of magnetic susceptibility variation. Additionally, the long readout time in the phase encoding direction can cause distortions. GRAPPA accelerates acquisition and therefore reduces distortion susceptibility without incurring a high acquisition time penalty. It also eliminates the

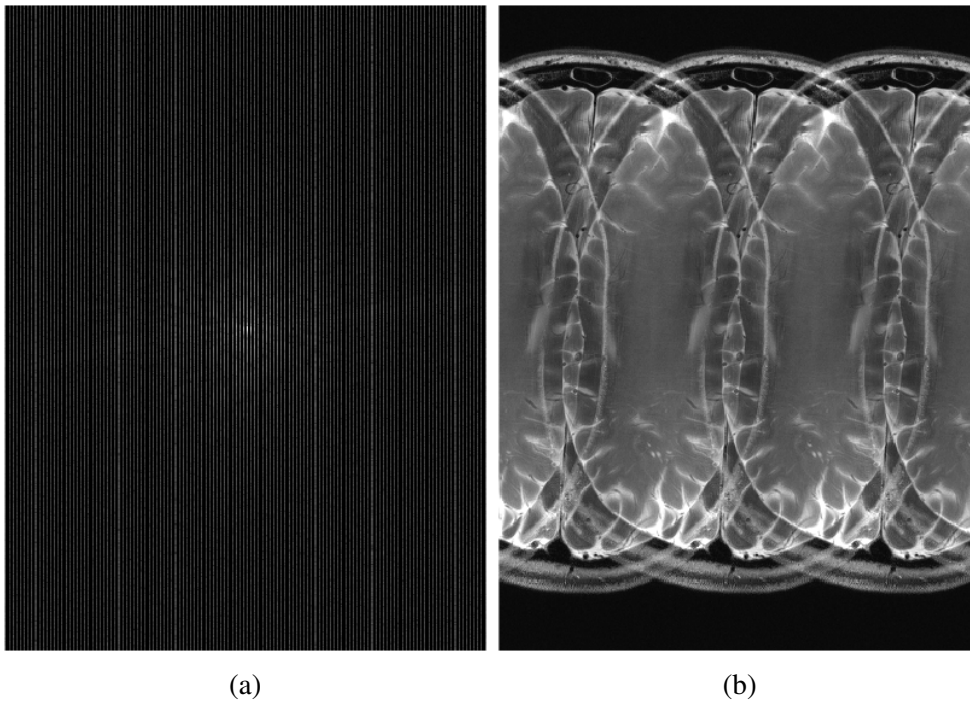


Figure 2.16: (a) The undersampled k-space map from a receive coil of a turbo spin echo (TSE) acquisition with an acceleration factor of 3, where for every acquired line, the two following lines are unacquired. (b) Reconstructing the undersampled k-space directly results in aliasing. If the lines are filled using GRAPPA reconstruction with ACS data, the aliasing can be eliminated.

need to reduce the FOV, which can introduce a phase wrap-around artefact [8]. This acquisition acceleration is also important in 7T MRI as it assists in reducing scan times when high spatial resolution (high k-space coverage) is used.

## 2.3 Advanced sequences

### 2.3.1 Echo planar imaging (EPI)

One example of a fast acquisition technique is the echo planar imaging technique or EPI. Despite it and its derivations remaining widely used today, this technique was first established in the early days of MRI. Nobel laureate Peter Mansfield first proposed this in 1977 [33] as a planar imaging technique exploiting the properties of the spin echo. The technique can now be implemented with gradient echo and spin echo techniques. Figure 2.17 illustrates the way the basic EPI technique works. It initially involves the application of a simple spin preparation module, such as a single RF excitation pulse. Following this pulse, the prephase gradients are

applied in both readout (frequency encoding) and phase encoding directions, which result in the spins acquiring negative phase shifts and stepping the acquisition to the corner of k-space. After this step, the first k-space line is acquired with a positive readout gradient lobe. A short, positive phase encoding gradient is then applied to move the acquisition to the next k-space line, followed by data sampling for this line using a negative readout gradient. These steps are repeated until all of the k-space lines are acquired. This method of alternating encoding gradients create a continuous Cartesian trajectory with alternating directions along  $k_x$  for alternate lines that typifies this technique. While this base technique only uses a single RF excitation pulse (single-shot), multi-shot variations of EPI can be implemented by using more excitation pulses. Overall, the technique provides a rapid way to acquire k-space, with one slice obtainable in less than 100ms.

The EPI acquisition requires a high receiver bandwidth in order to traverse through all of k-space before the  $T_2^*$  relaxation completes. However, the low spatial resolution of EPI also makes it unsuitable for certain clinical purposes. Due to imperfect gradient switching, gradient imperfections and linear eddy currents, k-space shifts occur during readout. Phase errors also accumulate during the acquisition of the alternating lines. The result is a ghost replica of the image, shifted by  $FOV/2$ . This is called a Nyquist ghost [34]. One way to compensate for this is by a phase correction reference scan prior to the primary acquisition. This reference acquires the positive and negative direction readouts without the phase encoding to determine the necessary phase offsets [35]. Beside the Nyquist ghosting, EPI is also vulnerable to other factors, such as  $B_0$  inhomogeneity, off-resonance induced chemical shift effects and spatial distortions. This effect is more pronounced in the phase encoding direction than in the frequency encoding direction, because of its low bandwidth per pixel caused by the long readout time. The phase encoding bandwidth is smaller, essentially equal to the frequency encoding bandwidth divided by the number of readout samples and inversely proportional to the echo spacing in the EPI echo train. If the other chemical component (e.g. fat) is known, the chemical shift in the phase encoding direction can be estimated as following:

$$\Delta y = \Delta f \frac{FOV_y}{BW_y} \quad (2.39)$$

where  $\Delta y$  is the chemical shift,  $\Delta f$  is the precession frequency difference (e.g. between water and fat),  $FOV_y$  is the field of view, and  $BW_y$  is the bandwidth (equivalent to the inverse of time between each readout sample).

### 2.3. Advanced sequences

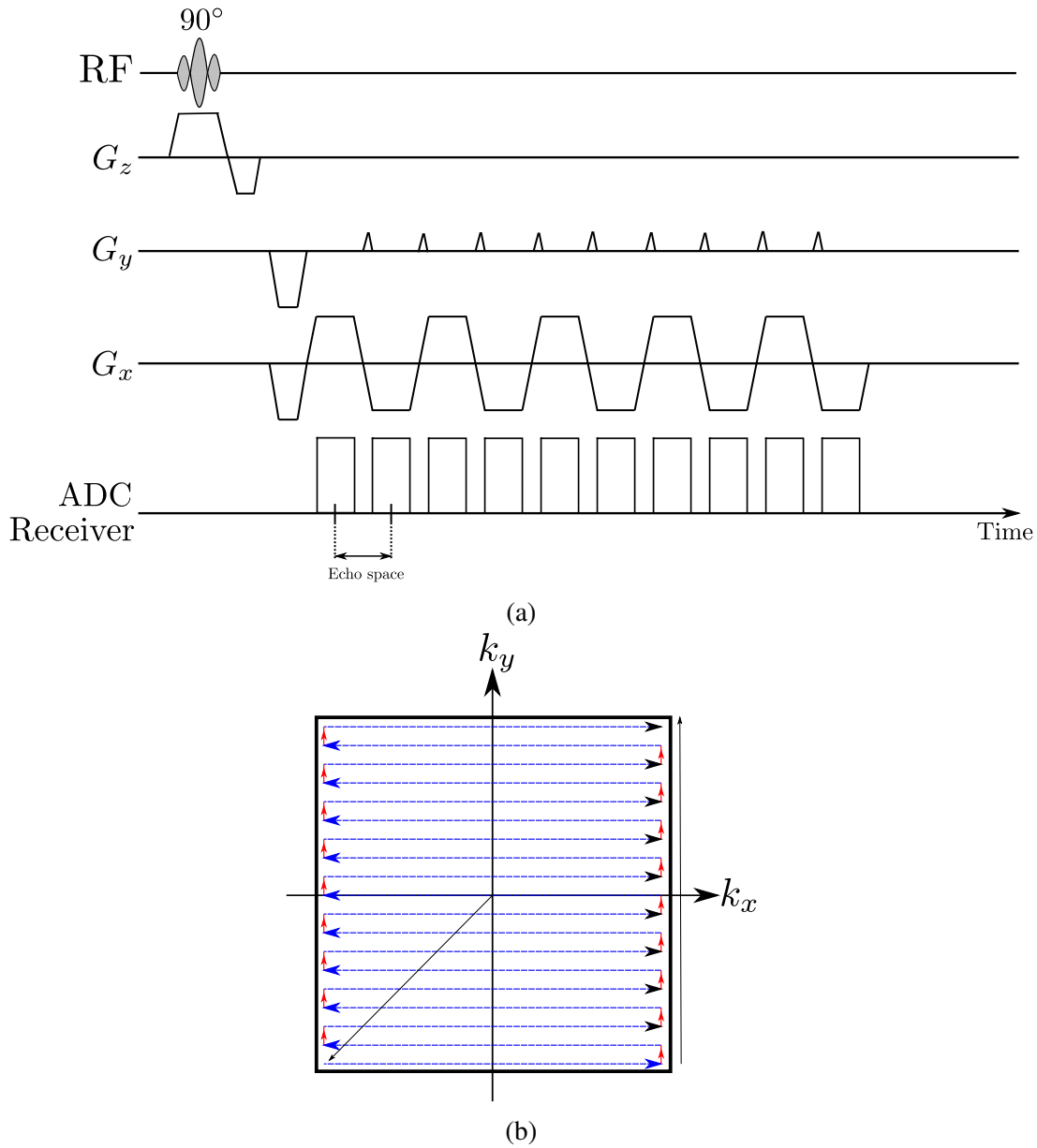


Figure 2.17: (a) A pulse diagram showing a single-shot, gradient-echo EPI sequence. The echo spacing represents the time between the readout of two k-space lines. (b) The k-space trajectory of a single-shot EPI acquisition.

### 2.3.2 Turbo spin echo (TSE)

Another accelerated MR imaging technique is a variation of the spin echo technique called turbo spin echo (TSE). TSE is also known as fast spin echo (FSE) or, as originally introduced in 1986, rapid acquisition with relaxation enhancement (RARE) [29]. This technique differentiates itself from the standard spin echo technique by the usage of multiple, consecutive RF refocusing pulses, instead of just one. The application of this refocusing pulses series generate a train of further spin echoes. Accompanied by adjustments by addition of phase encoding steps during and between the echoes, several k-space lines can be acquired within a single repetition time interval. The result is a significantly-accelerated spin echo acquisition, with the acceleration factor governed by the number of echoes acquired within one TR or the echo train length (ETL). This acceleration gives TSE superior  $T_2$  contrast compared to standard spin echo. The subsequent time savings can also be utilised to improve the acquisition in other ways. Extra time per repetition can be allocated to recover more longitudinal magnetisation and therefore improve SNR. More phase-encoding steps can also be added to improve the image resolution. While these are beneficial, some drawbacks are present. The addition of more refocusing pulses increases the specific absorption rate (SAR) with potential consequences on tissue heating. This can be offset by using smaller flip angles on the refocusing pulses [36]. TSE also suffers from altered contrast, for example bright fat signals when used for  $T_2$ -weighted imaging [37]. The technique is susceptible to coherent ghosting when there is subject motion during imaging, due to the sampling of multiple k-space segments at each spin excitation.

Overall image contrast is governed by the effective TE ( $TE_{eff}$ ), which is the time when the zero-order and low-order phase-encoding gradient moments are acquired. As these encoding steps cover the contrast data-rich centre of the k-space, changing  $TE_{eff}$  can be used to obtain a desired contrast [38]. Typically,  $TE_{eff}$  is defined to be the centre of the echo train.

### 2.3. Advanced sequences

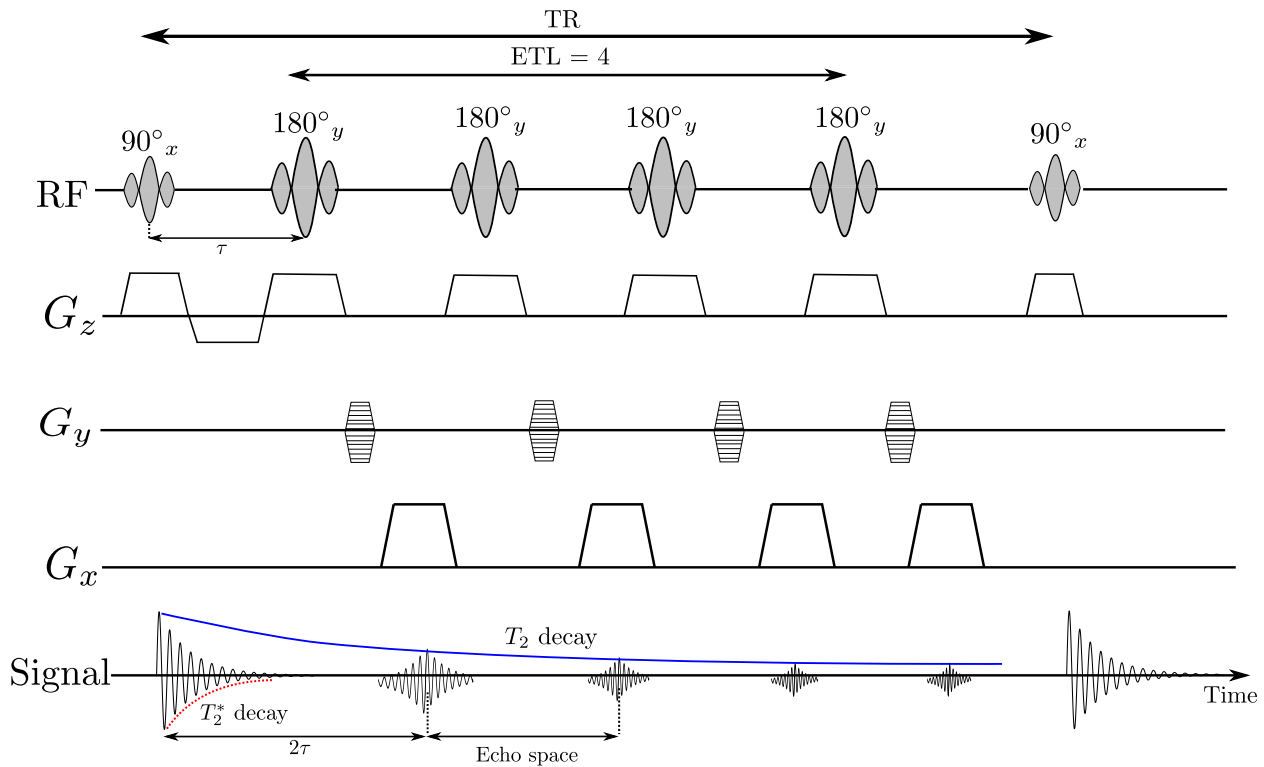


Figure 2.18: A turbo spin echo (TSE) sequence with an echo train length (ETL) of 4. After an initial RF excitation pulse, a series of refocusing RF pulses is applied. Multiple spin echoes form in the interval between the refocusing pulses, allowing for more k-space readouts. The first echo appears after approximately twice the time between the excitation and refocusing pulses ( $2\tau$ ).  $G_y$  gradients are varied from excitation to excitation and from echo to echo.

## 2.4 Simultaneous multislice imaging (SMS)

As the multislice-to-volume prospective motion correction later described in Chapter 3 utilises a subset of slices for motion detection, the use of simultaneous multislice imaging (SMS) can potentially speed up the rate of motion correction updates. The concept of the technique is explored in this section.

### 2.4.1 Concept

The basic principle of SMS involves applying a multiband RF pulse with a slice-selective gradient, which excites several slices in the volume at once. While accelerating acquisition time, SMS techniques inflict minimum SNR reduction as it does not affect the echo train length or phase encoding steps [39] [40]. SMS acceleration can however incur SNR penalties due to slice aliasing that occurs during reconstruction (measured by the g-factor). When the distance between slices is especially small, the g-factor penalty is high and aliasing effects become more prominent. These negative effects can be reduced by controlling the slice aliasing during k-space sampling. An effective sampling technique is the controlled aliasing in parallel imaging results in higher acceleration (CAIPIRINHA) method [41]. CAIPIRINHA uses a phase-shifted sampling patterns with a goal of reducing pixel overlap and separating the close slices in a controlled manner. Consequently, the aliasing during reconstruction can be minimised. Its derivation Blipped-CAIPI [42] includes rewinding gradients in the slice-select direction, which allows phase accrual to be kept within  $\pm \frac{\pi}{2}$ . This reduces the occurrence of voxel-tilting artefacts, which are especially problematic in EPI applications with SMS, such as functional MRI (fMRI) and diffusion-weighted imaging (DWI) studies [42]. The higher spatial and temporal resolution would also be beneficial for blood oxygen level dependent fMRI [43]. DWI is commonly performed with EPI-based techniques and is particularly sensitive to motion [44].

A major constraint in designing the simultaneous multi-slice part of the technique would be the peak amplitude of the multiband RF pulse. The peak power of the multi-band pulse increases quadratically with the number of simultaneously excited slices [39]. With the power-demanding refocusing pulses and the higher power levels at 7T, the pulse would be susceptible to causing localised SAR peaks that may not be possible due to the safety limits in operation at the scanner. Several possible strategies can be used to mitigate this issue. These include phase-shifting the component multiband pulses or by using asymmetric multiband pulses (e.g. using “root-flipping”) [45] [46]. Another method that can be employed is to modify the excitation pulses to occur in a periodic manner, for example the power independent of number of slices

## 2.4. Simultaneous multislice imaging (SMS)

---

(PINS) algorithm (which modifies the pulses using a Dirac comb function) [47]. Designing the pulses using the principles of these methods can reduce power and prevent it from exceeding the scanner limits.

### 2.4.2 Reconstruction

The SMS-acquired data are reconstructed using the slice-GRAPPA (generalised autocalibrating partial parallel acquisition) technique [42]. This version of GRAPPA reconstruction involves several steps, similar to in-plane (slice-specific) GRAPPA reconstruction (described in Section 2.2.6) but with several differences. First, k-space data of the target slices is acquired from each of the receive coils. As several slices are acquired at the same time, this can create a complication where the images stack on one another in the same area and become difficult to disentangle. This is where a sampling technique like CAIPIRINHA or blipped-CAIPI can help. Using the additional rewinding gradients in the slice-select direction, the slices simultaneously excited by the complex RF pulse accrue extra phases, causing the relevant slices to be maximally-shifted in the phase-encoding direction. Consequently, separating the simultaneously-acquired set of slices becomes simpler. This process is illustrated in Figure 2.19

While basic GRAPPA reconstruction only considers the single-slice ( $xy$ ) plane, slice-GRAPPA includes the  $z$  or slice dimension. The weights of the individual slices are acquired from an autocalibration scan (ACS) acquired at the start. Instead of a fully-sampled centre of k-space, the slice-GRAPPA ACS consists of a fully-sampled volume of single-band slices from each coil. The GRAPPA weights of each slices are also calculated to enable separation of the aliased slices. The in-plane GRAPPA k-space convolutional relationship can be extended to describe this calculation of the separated image [44]:

$$S_{cz}^{sp} = \sum_{c=1}^C w_{kcz} \otimes S_c^{mb} \quad (2.40)$$

where to obtain the separated image k-space map  $S_{cz}^{sp}$  from receive coil  $c$  and slice  $z$ , the slice-GRAPPA weights  $w_{kcz}$  are convolved with the aliased multiband image  $S_c^{mb}$  across all  $C$  receive coils.

An inverse Fourier transform is then applied, providing images from each coil. The reconstruction is completed by combining these individual images using sum-of-squares or weighted complex sum, thereby producing the desired image [7].

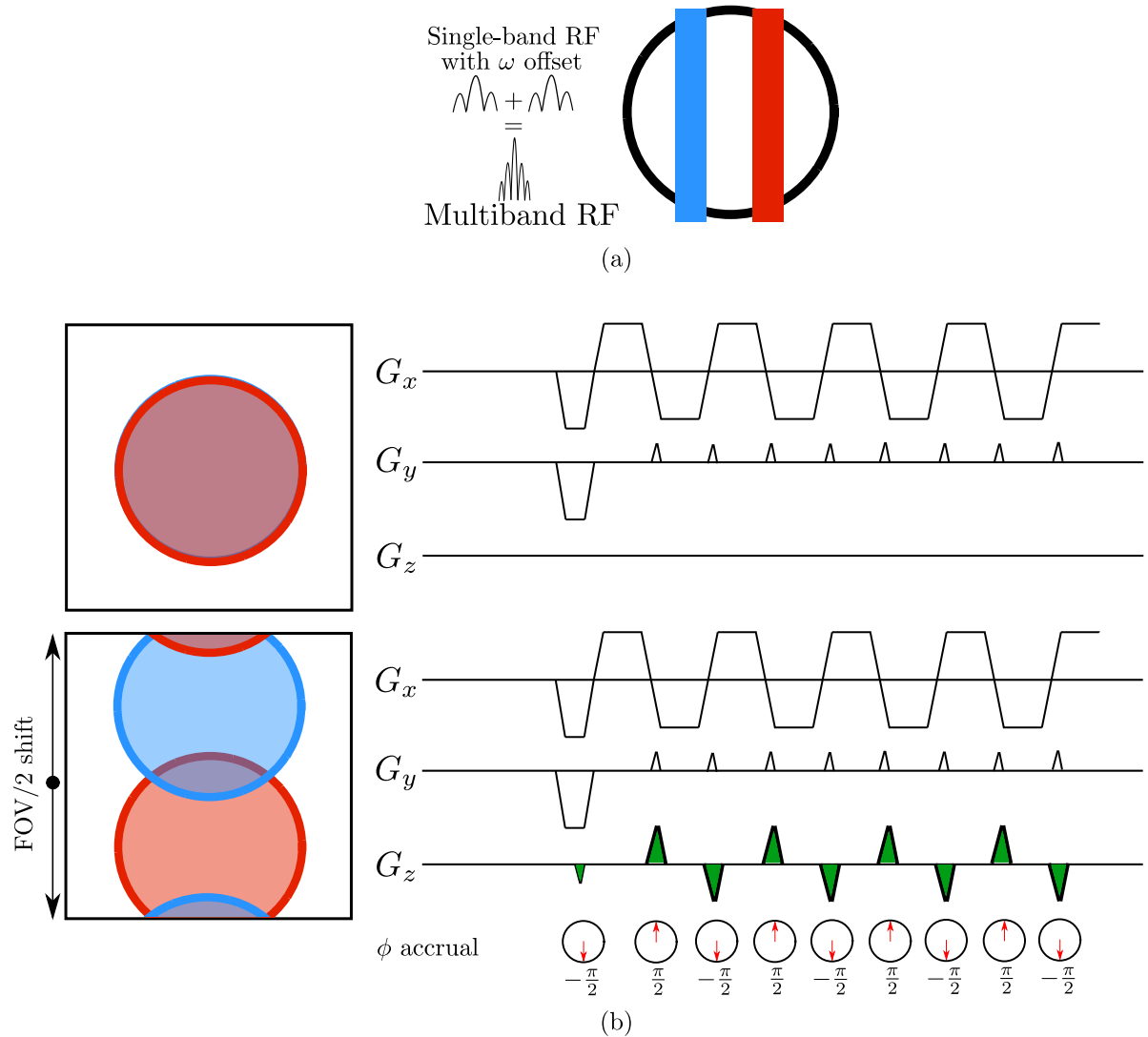


Figure 2.19: (a) To excite several slices simultaneously, a composite multiband RF pulse composed of two single-band RF pulses with a frequency offset of  $\omega$  is used. (b) Using the blipped-CAIPI technique, where rewinding gradients are added in slice-select direction, the slices are shifted by  $FOV/2$  to simplify the separation process.

## 2.5 Ultra-high field MRI

Ultra-high field (UHF) MRI scanners for human scanning, especially at the field strength of 7 Tesla, are becoming increasingly available. 7T scanners were becoming more available in routine clinical settings. The motivation behind the move towards higher field strengths is primarily the intrinsic increase in SNR, which grows near-linearly with the magnetic field strength (shown

## 2.5. Ultra-high field MRI

in 2.20) [48][49].

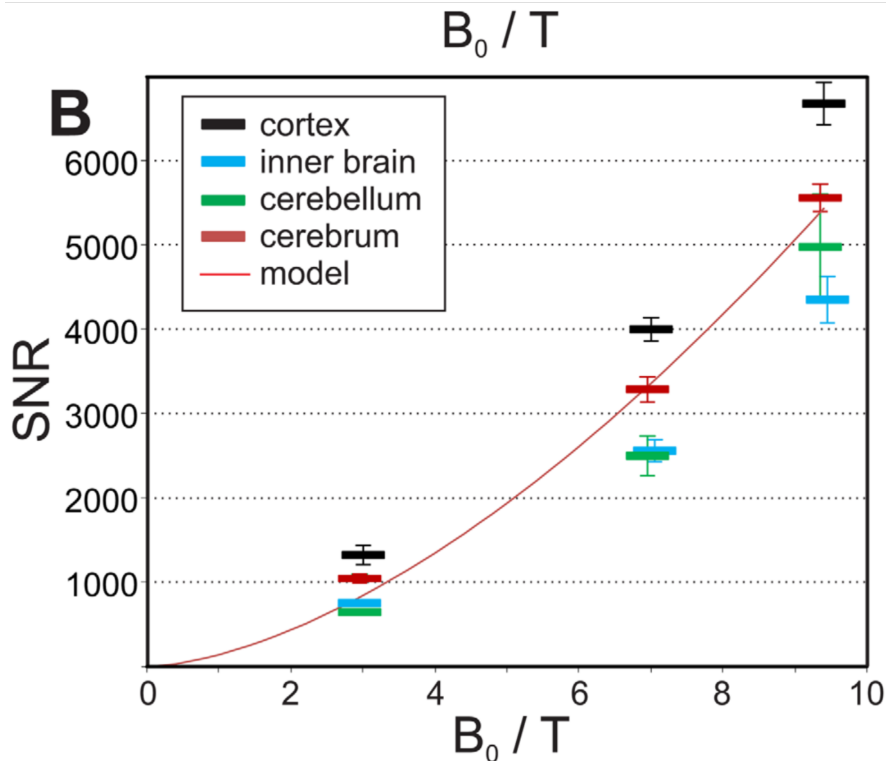


Figure 2.20: SNR values in different parts of the human brain plotted against the main magnetic field strength  $B_0$ . A fitting of the cerebrum's SNR values is shown as the red line, showing a near-linear increase in SNR with increasing  $B_0$ . Reproduced from [49] with permission from the publisher John Wiley and Sons, Inc.

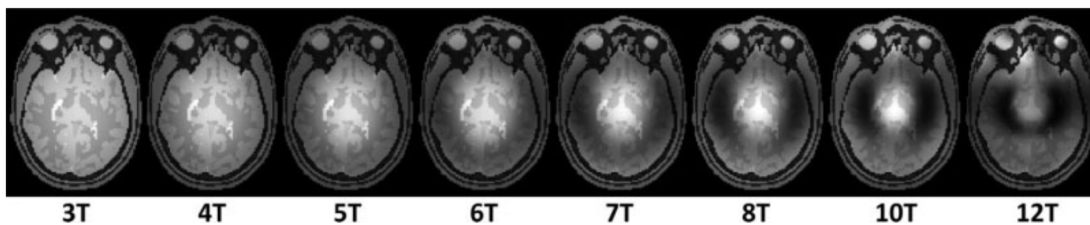


Figure 2.21: Simulated gradient-echo images with increasing magnetic field strength, showing a regressing trend of image homogeneity. Reproduced from [4] with permission from the publisher John Wiley and Sons, Inc.

With increasing magnetic field strength, the RF wavelength becomes shorter. At 7T, the  $^1\text{H}$  nucleus resonates at 298Hz and the RF wavelength in human tissue is 12cm. This wavelength is equal to or shorter than many organs in the human body and especially relevant for this thesis, half the longest measure of the head [50]. The interferences between the electromagnetic (EM)

waves cause RF transmit/ $B_1^+$  field or flip angle inhomogeneity. The consequence is a progressively more inhomogeneous image profile as the field strength increases, as illustrated in Figure 2.21 [4]. Compensating this with applying much higher RF transmit power can cause uneven and potentially unsafe SAR levels within the anatomy [45] [51]. This  $B_1^+$  field inhomogeneity and its related issues have been the primary reasons why parallel transmit imaging (pTx) has become an important tool in UHF MRI research.

### 2.5.1 Parallel transmit MRI

Parallel transmit coils can remedy this by using multiple arrays to transmit RF signals and create a more uniform RF excitation profile. The overall  $B_1^+$  directed towards the target can then be expressed by a sum of  $B_1^+$  contribution from individual transmit channels [52]. Assuming the same pTx RF pulse  $b_{pTx}$  is played out the whole time on all channels and applying complex weights  $w_c$  with the variable spatial coverage of each of the  $T$  transmit channels  $S_c$ , the sum can be expressed as:

$$B_1^+ = \sum_{c=1}^T B_{1,c}^+ = b_{pTx} \sum_{c=1}^T w_c S_c \quad (2.41)$$

While this can enhance the image quality, using pTx pulses can also cause SAR issues. The transmitted EM waves may create constructive and destructive RF interferences within the subject, which lead to unsafe local SAR hotspots. Robust modelling of the SAR patterns is thus vital for the implementation of parallel transmit imaging for human scanning in vivo. For safety purposes, SAR patterns within tissue are simulated using digital models, which are verified by  $B_1$  mapping. Image uniformity is optimised by using  $B_1^+$  shimming or full pTx methods that use dedicated RF and gradient waveforms, where they are designed to work to complement each other [52] [53]. By applying these optimised RF and gradient waveforms, localised SAR hotspots and loss of signal and contrast from  $B_1^+$  field inhomogeneity can be minimised [2] [54].

While the amount of clinical validation of pTx for UHF MRI is still limited, the studies which explored pTx in clinical cohorts have demonstrated improved image quality and consequently potential for clinical benefits. Figure 2.22, which compares brain images of a multiple sclerosis patient acquired with single transmit (sTx) conventional and pTx imaging, shows significant improvement in signal homogeneity when pTx was used in comparison to sTx. The cerebellar region, which suffers from signal losses in sTx, has improved spatial uniformity.

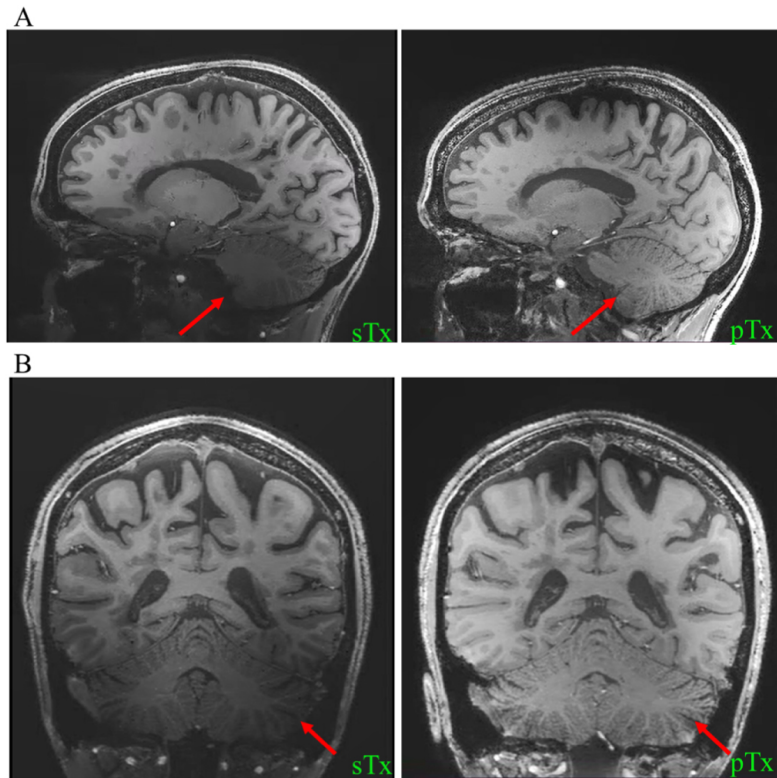


Figure 2.22: The comparison of (A) sagittal and (B) coronal MPRAGE images of the brain of a multiple sclerosis patient acquired with single (sTx) and parallel transmit (pTx) MRI. The cerebellum is highlighted with the red arrows. Reproduced from [50] with permission from the publisher IOP Publishing.

## 2.6 Functional MRI (fMRI)

A type of MRI application is functional MRI (fMRI), which measures neuronal changes in the brain related to blood flow. The relationship between these two processes in the form of neurovascular coupling can be exploited to create a blood oxygen level dependant (BOLD) contrast, a now-integral fMRI technique first described by Ogawa et al. (1990) [55].

When a cerebral region responds to a stimulus, the neurons require energy to be transported from outside as they do not have excess energy storage. The neurovascular unit, consisting of neural tissue and blood vessels [56], regulates accordingly and induces a haemodynamic response in the region to provide the neurons with necessary energy to function. This leads to a local change in the ratio of the two haemoglobin (Hb) substrates, oxyhaemoglobin and deoxyhaemoglobin. The former is diamagnetic, while the latter is paramagnetic. As deoxyhaemoglobin is paramagnetic, it increases local field susceptibility which leads to faster  $T_2$  and  $T_2^*$  relaxation. This means as the concentration of deoxyhaemoglobin increases,  $T_2$  and  $T_2^*$  re-

laxation times decrease. This relationship can be described as following [13]:

$$R_2^* \propto V[dHb]^\beta \quad (2.42)$$

where  $R_2^*$  is the transverse relaxation rate (equivalent to  $\frac{1}{T_2^*}$ ),  $V$  is the blood volume,  $[dHb]$  is the concentration of deoxyhaemoglobin in blood and  $\beta$  is the exponent signifying that this relaxation-blood oxygenation relationship is not always a simple proportionality.

Using fast imaging sequences such as EPI [57], these small changes can be observed over a time series. The BOLD contrast has been used in resting-state (observing baseline changes) and stimulus or task-based fMRI experiments [58]. Due to increasing susceptibility differences between the two Hb substrates and capacity for higher spatial resolution imaging, the BOLD effect becomes more pronounced at higher  $B_0$  field strengths (including the focus field strength of 7T in this thesis) compared to lower field strengths such as 1.5 and 3T [59].

## 2.7 Motion correction in MRI

### 2.7.1 The motion issue

Today, MRI has become a vital evaluation and diagnostic tool routinely used for clinical management and research studies. The variety of pulse sequence and contrast techniques available also makes MRI easily adaptable for a myriad of purposes. Nonetheless, MRI is an imaging modality particularly susceptible to motion effects due to the extended scan time. While it is feasible for patients to remain still during shorter scans, the lengths of some MRI sessions, which can extend to 30 minutes or more, can cause some discomfort to the patients. Compounded by other potential sources of anxiety (e.g. claustrophobia, loud noises, contrast injection), subject motion can become quite significant during MR scanning [60]. Motion effects can also be short and fast (e.g. due to coughing, swallowing or sneezing), or longer-term and subconscious (e.g. involuntary muscle movements) [61]. Staying still during the whole scan can also be challenging for certain categories of patients, for example geriatric, paediatric or neuropathic patients. These motion effects on images may obscure important anatomical features and thus render them unusable for accurate clinical diagnosis. This often leads to a need for repeated scans, which incur additional costs and time and potentially delaying vital diagnoses for certain patients.

Acquiring signal data in the frequency/Fourier domain (k-space) also comes with potential complications when motion is involved. A shift in the subject's anatomical position during scanning will cause phase to accumulate and shift in the k-space data. Rotational motion effects

appear in both image and k-space domains. In multi-shot sequences, this can also lead to shot-to-shot phase variations. There is also a risk of short-term motion within the spatial encoding window after a single excitation, which can lead to shifts in k-space because the relationship between dephase and rephase gradients is disrupted. Periodic, patterned motion causes noticeable ghosting in the resulting image. Meanwhile, if the motion is random and follows an irregular pattern, the subsequent dephasing and erroneous phase accumulation cause the reconstructed image to have significant blurring and ringing artefacts [2].

Motion artefacts can be generally classified into rigid body and non-rigid (or deformable or elastic) motion. Rigid body motion is described by the spatial changes in the six degrees of freedom of the subject's three-dimensional region of interest (ROI). These cover translation along three axes and rotation about three axes. Rigid body motion is primarily caused by the aforementioned shifting of the patient's ROI during scanning [62]. On the other hand, non-rigid motion is caused by various physiological processes in the human body, such as respiratory and cardiac motion.

### **Motion artefacts at higher field strengths**

Due to the higher spatial resolution at 7T, motion effects are amplified compared to imaging at lower field strength. Small movements can cause major artefacts in the resulting image. In particular, this is an issue for the longer scan times used to acquire high-resolution and high-SNR images [3]. Even for cooperative subjects, involuntary motion inevitably occurs during the longer scan times required for these acquisitions [63][64]. Higher static field strengths like 7T are also associated with an increased level of discomfort in some subjects. Temporary physiological effects such as nausea, vertigo, headache and metallic dysgeusia may be experienced by subjects [65][66]. Therefore, there is a higher risk of subject motion. Small spatial changes have also been shown to disrupt the uniformity of the  $B_0$  field distribution, resulting in undesired phase changes [67]. In addition, with uneven signal intensity distribution due to the  $\vec{B}_1$  transmit field inhomogeneity [68], these motion effects negatively offset the improvements from using a higher field scanner.

### **2.7.2 Motion correction techniques**

With motion artefacts being commonplace in MRI examinations and their deleterious effects documented extensively, a multitude of motion mitigation and compensation techniques have been proposed and developed over time [2][62][69][70][71]. Figure 2.23 shows categories of common techniques for mitigating and compensating for motion in MRI.

<b>Motion prevention</b>	<b>Artifact reduction</b>	<b>Motion correction</b>
Training	Faster imaging	Navigators
Distraction	Insensitive sequences	Self-navigated trajectories
Feed and wrap (for babies)	Gradient moment nulling	Prospective correction
Foam restraints	Saturation bands	Retrospective correction
Sedation	Triggering and gating	
Bitebars/head holders	Phase reordering	
Breathhold		

Figure 2.23: Various categories of motion mitigation and compensation techniques. Reproduced from [2] with permission from the publisher John Wiley and Sons, Inc.

### Motion prevention techniques

The most elementary way to prevent the occurrence of motion artefacts is by preventing motion from happening in the first place and/or using fast acquisition techniques that are less motion sensitive. This can be achieved by using restraints, pre-scan subject training or anaesthesia. Widely used in routine and experimental MRI scanning, flexible head restraints such as polystyrene cushions, foam pads and plastic straps can be used to restrict the subject's head motion within the coil. Customised head restraints are also used for some repeat or long examinations, but implementing it for regular clinical practice can be impractical [71]. Nonetheless, this restriction is not able to completely eliminate subject motion. Another classic example of head restraining tool is bite bars fixed to the top of the head coil. While this technique was able to reduce head motion to an acceptable level, the major discomfort caused and the increased frequency of oral motion present hurdles for widespread adoption [72]. An alternative method is to administer or partial or general anaesthesia to the subject (typically in paediatric examinations) prior to the scan. General anaesthesia is more reliable than partial sedation for this purpose, but both come with potential adverse events and/or long-term risks [73].

Motion artefacts can also be "pre-empted" by employing fast acquisition and acceleration techniques, providing that the scanner hardware is able to accommodate this multitude of techniques. Additionally, taking advantage of the multiple parallel receiver channels can accelerate the acquisition even further. Parallel imaging techniques, such as the Generalized Autocalibrating Partially Parallel Acquisitions (GRAPPA) technique [7], yield unaliased images with much reduced acquisition time. Simultaneous multislice imaging (SMS) acquisition also expedites acquisition by using a multiband RF pulse to excite multiple slices at the same time (discussed in Section 2.4) [39] [74].

### Retrospective motion correction

Using retrospective motion correction techniques, motion effects can be corrected after the acquisition of k-space data. This class of techniques uses detected motion information to develop a matrix model of acquired data, which is then used to interpolate, transform and correct the data [75]. There is a range of methods used to obtain the necessary motion parameters to correct the data retrospectively. One way is by using MR navigators, for example with FID navigators [76], fat image navigators/FatNavs [77] and PROPELLER (periodically rotated overlapping parallel lines with enhanced reconstruction) [78]. Another way is to use volume-to-volume motion detection, which detects motion by registering each volume to a reference volume [62]. Alternatively, physiological (respiration/cardiac) pattern synchronisation and modelling can be used [79]. Another option is using external tracking devices that subsequently feed motion information into the processor for retrospective correction [80]. While the formerly mentioned techniques rely on accurate scan-time estimation of motion, there are also techniques that are based on iterative models using k-space data independent of navigators or trackers. These techniques calculate motion parameters either by evaluating consistency across the data [81] or minimising a metric of image or gradient entropy [82] [83] [84]. While limiting additional complications to the scanning protocol, retrospective techniques have their drawbacks. Retrospective algorithms are often computationally expensive and sophisticated. Coupled with long scan times, these techniques are not particularly feasible for high resolution acquisition [84]. On the contrary, retrospective techniques are not sensitive to corruption caused by the feedback of erroneous motion information that may occur in prospective techniques.

Estimation of motion parameters is a vital component in successfully reconstructing the motion-corrupted images. This can be achieved by using image registration. The parameters and thus the transformation between the reference and subsequent motion-affected acquisitions can be calculated iteratively with registration. In the case of head motion, a rigid body model can be used to describe the motion evolution. This model consists of six parameters, which are three (x-, y- and z-axes) translation and three (x-, y- and z-axes) rotation parameters.

### Image registration

Image registration is a tool used to measure and correct the misalignment between individual images or imaging volumes. It has found applications in many fields from astronomy to medical imaging. While the algorithms available for image registration are many, the process involved in each of these algorithms is underpinned by the same principle of operation, as illustrated in Figure 2.24. The operation involves repeatedly performing a spatial transformation  $\tau$  of a

moving or source image  $I_{mvg}$ . A comparison guided by a similarity metric  $s$  is then performed between this transformed moving image  $I_{trans} = \tau(I_{mvg})$  and the reference, target or fixed image  $I_{ref}$ . These steps are then iterated  $n$  times until the optimal alignment is found. This problem can be expressed as following:

$$\operatorname{argmin}(s_n(\tau_n(I_{mvg}), I_{ref})) \quad (2.43)$$

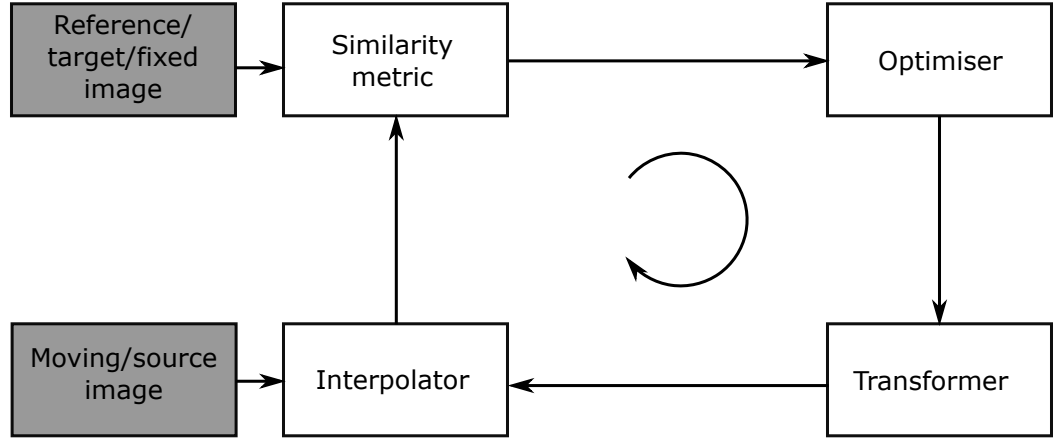


Figure 2.24: The basic principle of iterative registration of two images with an optimiser and interpolator. This process is guided by a similarity metric.

A wide taxonomy of similarity metrics and registration optimisers can be used for this iterative registration process [85]. In terms of similarity metrics, the simplest is by calculating the sum of squared intensity differences ( $s_{SSD}$ ) between the moving and reference images:

$$s_{SSD} = \sum_{(x,y)} |I_{mvg}(x,y) - I_{ref}(x,y)|^2, \forall (x,y) \in I_{mvg} \cap I_{ref} \quad (2.44)$$

This metric has a low computational power requirement and thus fast, but unsuitable for multimodal or multicontrast registration (e.g. registration of CT and MR images, or PET and CT) because of the substantial signal and contrast differences between the modalities. More complex metrics include cross-correlation ( $s_{CC}$ ) and mutual information ( $s_{MI}$ ):

$$s_{CC} = \frac{\sum(I_{mvg} - \overline{I_{mvg}}) - (I_{ref} - \overline{I_{ref}})}{\sqrt{\sum(I_{mvg} - \overline{I_{mvg}})^2 \sum(I_{ref} - \overline{I_{ref}})^2}}, \forall \in I_{mvg} \cap I_{ref} \quad (2.45)$$

$$s_{MI}(I_{mvg}, I_{ref}) = H(I_{mvg}) + H(I_{ref}) - H(I_{mvg}, I_{ref}) \quad (2.46)$$

where  $\overline{I_{mvg}}$  and  $\overline{I_{ref}}$  are the average voxel values for the moving and reference images respec-

## 2.7. Motion correction in MRI

---

tively,  $H(I_{mvg})$  is the entropy of the moving image,  $H(I_{ref})$  is the entropy of the reference image and  $H(I_{mvg}, I_{ref})$  is the joint entropy of both images. These algorithms are more robust for multimodal/contrast registration, but incur a higher computational power and time. A variant of this metric is the Mattes' mutual information metric [86][87]:

$$s_{MI} = - \sum_{L \in I_{mvg}} \sum_{K \in I_{ref}} p(L, K) \log\left(\frac{p(L, K)}{p(L)p(K)}\right) \quad (2.47)$$

where  $p(L)$  and  $p(K)$  are the individual marginal probability distributions of the moving and reference images respectively, and  $p(L, K)$  is the joint probability distribution of both images. Note that as mutual information is maximum when the transformed moving image is the most similar to the reference, the negative of  $s_{MI}$  is required for the minimisation problem. This metric uses a concept in information theory to estimate the similarity of two images by evaluating the relationships between their underlying image histograms, instead of their signal intensities.

The registration optimiser receives the value of the similarity metric  $s_n$  and determines the progression of the iteration process. An example is by using a regular step gradient descent method. This method works by iterating step-by-step along the negative gradient of the similarity metric function  $F$ ,  $-\nabla F$ . This method works well for single-modal registration. Multimodal registration employs other optimiser methods such the one-plus-one evolutionary iteration. The iterative minimisation process eventually arrives at a spatial transformation that best represents the registration between the moving and reference images.

Another vital component of the image registration process is the choice of the spatial transformation type. These types are classified to the number of degrees of freedom they include. The first type is the rigid body transformation model. This model covers six degrees of freedom and only considers translation  $t$  and rotation  $r$  with respect to the x-, y- and z-axes. Consequently, this model is very simple, yet able to estimate in-plane and through-plane motion-induced changes [88]. A rigid body spatial transformation matrix can be expressed as following:

$$\tau = \begin{bmatrix} r_{xx} & r_{xy} & r_{xz} & t_x \\ r_{yx} & r_{yy} & r_{yz} & t_y \\ r_{zx} & r_{zy} & r_{zz} & t_z \\ 0 & 0 & 0 & 1 \end{bmatrix} \quad (2.48)$$

We can then decompose this matrix into a separate translation  $T$  vector and rotation  $R$  matrix:

$$T = \begin{bmatrix} t_x \\ t_y \\ t_z \end{bmatrix}, R = \begin{bmatrix} r_{xx} & r_{xy} & r_{xz} \\ r_{yx} & r_{yy} & r_{yz} \\ r_{zx} & r_{zy} & r_{zz} \end{bmatrix} \quad (2.49)$$

Following the conventional way of applying rotation first before the translation, the overall transformation of the vector  $\vec{x}$  after  $n$  transformations can be described as [5]:

$$\vec{x}_{final} = R_{tot}\vec{x} + t_{tot} \quad (2.50)$$

where  $R_{tot} = R_1 + R_2 + \dots + R_n$  and  $t_{tot} = R_2t_1 + \dots + R_nt_{n-1} + t_n$ .

Using the full rotation matrix means there is a total of 12 parameters (9 rotational and 3 translational). These 3D rotational parameters can be represented in more compact ways, which will reduce the number of parameters to six. This is also important for prospective motion correction application as there are now fewer parameters to be fed back into the scanner system (discussed in the next subsection 2.7.2). First is the Euler angles  $(\phi, \theta, \psi)$ , which compact the 3D rotational parameters into three angular values. However, as the Euler angle triples are not unique to a set of 3D rotations, it is vulnerable to the gimbal lock phenomenon that can return unrealistic registration results [89]. A more elegant way to represent these rotational components is by using quaternions [90]. Quaternions represents the 3D rotational system as:

$$q = w + q_xi + q_yj + q_zk = (w, \vec{q}), \vec{q} = \begin{bmatrix} q_x \\ q_y \\ q_z \end{bmatrix} \quad (2.51)$$

where  $w$  is the rotation around the three axes  $(q_x, q_y, q_z)$  with  $(1, i, j, k)$  as the basic quaternions. The quaternions also has a property where  $i = j = k = \sqrt{-1}$ . The 3D rotational parameters can then be reduced into simpler representations using the unit quaternions or versors of  $q$ , which is also unique:

$$\|q\| = 1 = \sqrt{w^2 + q_x^2 + q_y^2 + q_z^2} \quad (2.52)$$

Combining all of the rotations produces the overall rotation [5]:

$$q_{tot} = q_1 + q_2 + \dots + q_n \quad (2.53)$$

Rigid body transformation can provide an estimate of in-plane and through-plane motion, but

an option of using non-rigid transformation is also available. One transformation model of this class, affine transformation, takes into account shearing and scaling transformation components. However, the increase to twelve degrees of freedom also means an increase in calculation time and a reduction in the confidence limits of parameter estimates. Other non-rigid models such as in-plane or out-of-plane deformable models are available [88], but these are not very applicable in neurological imaging. As the shape of the head and brain does not change significantly with motion, a rigid body model is suitable [91].

### **Prospective motion correction**

Another approach to motion correction is using prospective motion correction techniques. This group of techniques uses tracking or navigating tools to detect motion during the acquisition and subsequently adapt the scanner coordinates in real time. The objective is to keep the spatial relationship between the subject and scanner's imaging volume constant. Similar to in retrospective techniques, the tracking data needed for correction can be acquired using MR navigators and external tracking equipment.

External tracking equipment is typically independent of the MRI scanner itself. Examples include in-bore optical trackers [92], reflector-based laser positioning system [93], outer-bore stereo tracker cameras [80], NMR probes [94] and ultrasound imagers [95]. When cameras or other optical trackers are used, the device must be properly aligned to markers attached on the subject's head. Markerless techniques, such as using point cloud reconstructions [96], have also been introduced. While able to provide fast and accurate updates to the imaging system, external devices have the downside of additional complexity and inconvenience to the subject. Paired with the limited space within the head coil and the overall MR system, implementing these devices in routine clinical environment is challenging.

MR navigators can be classified into k-space and image-space navigators. The use of navigators have evolved since a 1989 method proposed by Ehman and Felmlee [97], which uses one-dimensional frame projections via interleaved sampling to determine displacement in the frequency encoding direction. K-space navigator techniques, such as orbital [98] and cloverleaf navigators [99], sample the k-space in motion-sensitive trajectories that can be then compared to a reference. Alternatively, image-based navigators can also be used, in which the MR images themselves are employed to acquire real-time motion parameters. Techniques in this category include PROMO [100] and the Prospective Acquisition Correction (PACE) [5]. PROMO uses three orthogonal spiral navigators, which are then passed onto an extended Kalman filter framework. PACE, which also provides a base to the methodologies later described in this thesis, was originally used to track motion effects in functional MRI (fMRI). The motion parameters are

obtained by performing six degree-of-freedom, rigid-body image registration of the initial EPI volume to the subsequent volumes. These MR navigator techniques have the distinct advantage of not requiring potentially cumbersome devices and consequently inconvenience to subjects. However, it is important to note that these navigators have to be acquired along with the primary imaging sequence, which inevitably extend scan times, and also with consistent SNR in the case of the image-space navigators as less motion-corrupted image would need to be discarded during post-scan analysis [101]. The navigator echo acquisitions must fit within the pulse sequence architecture [2].

Overall, beside the reduction of data interpolation effects, prospective techniques minimise the changes in magnetisation history due to the constant update of the imaging volume as the acquisition progresses. Motion-induced relaxation effects can then be avoided [5]. The need for rapid navigators limit the use of computationally-expensive navigator techniques, but for brain imaging, this is precluded by the fact that the rigid-body model often sufficiently describe head motion. There is also a limit with motion-induced  $B_0$  distortion effects, which can not be directly compensated by this class of techniques [102]. This is especially important at 7T due to the increased  $B_0$  inhomogeneity.



# Chapter 3

## Motion correction for echo-planar imaging at 7 Tesla using multislice prospective acquisition correction (MS-PACE)

### 3.1 Introduction

This chapter presents an alternative technique for prospective motion correction in 7T clinical MRI. The technique proposed in this chapter is adapted from a technique previously implemented at 3T, namely Multislice Prospective Acquisition Correction (MS-PACE), which in turn is inspired by PACE [5][6]. This echo planar imaging (EPI)-based technique has also been used in a navigator-based technique for clinical sequences such as turbo spin echo. This chapter aims to develop and validate MS-PACE application for 7T EPI motion correction. Problems unique to 7T and ultra high field MRI were considered during this development process.

### 3.2 MS-PACE

The MS-PACE technique, which was originally proposed by Hoinkiss and Porter [6], is a prospective motion correction technique that acquires real-time motion information by registering subsets of 2D EPI navigator slices to a reference volume acquired at the start of the measurement. This varies from the base PACE method which employ registration of full volumes of navigator slices to a reference volume [5]. This subset of slices registration scheme allows real-time updates to be performed at a heightened temporal resolution. These navigator slices can act as a navigator for other sequences but also as a self-navigator in EPI acquisitions.

## 3.2. MS-PACE

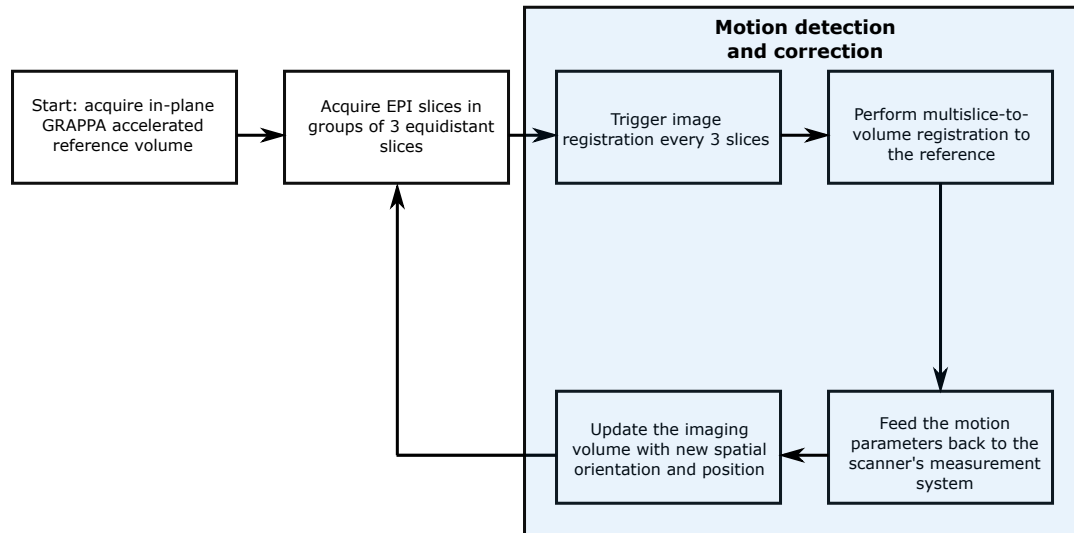


Figure 3.1: The 7T MS-PACE motion detection and correction pipeline. In this example, as only a subset of three slices is used for each registration, detection and correction can be done multiple times within a repetition time.

Shown in Figure 3.1, this technique follows an iterative process that begins with an acquisition of a volume of 2D EPI navigator slices at the start of the measurement. In the subsequent volumes of EPI slices, a registration to the reference volume is performed every time a new subset of three slices is acquired. Using the Mattes' mutual information similarity metric (described in Section 2.7.2), this multislice-to-volume registration then yields a 3D rigid body versor transformation matrix that is used to update the gradients and thus the acquisition volume. This particular similarity metric is chosen as it is more sensitive to image differences when information is more limited as in this technique, where only a subset of slices is used for registration. In this case, obtaining reliable and accurate motion estimation with typically computationally-lighter metrics, such as sum of squared differences, is more challenging [103]. This process, including the similarity metric, the gradient descent optimisation and the transformation matrix, uses the open source Insight Toolkit (ITK) libraries available within the Siemens' Image Calculation Environment (ICE) (Siemens Healthineers, Erlangen, Bavaria, Germany) image reconstruction framework.

The rigid-body image registration produces representative translational parameters in the three axes and three quaternion versors, which can be converted into rotational parameters. This is then fed back into the imaging system to correct for the motion effects by altering the slice position and orientation. The process is then repeated for every subset of three slices, enabling very quick motion updates. An important point for the slice subset acquisition is that the three slices are acquired with the largest-possible distance between one another. This is to ensure that

the registration can capture the rigid body head motion as accurately as possible.

## 3.3 Equipment

### 3.3.1 Locations and scanners

All experimental and developmental work, except for Section 3.4.1, was conducted at the Imaging Centre of Excellence site in Govan, Glasgow, Scotland. Embedded in the NHS Scotland Queen Elizabeth University Hospital, the Centre houses a MAGNETOM Terra 7T MRI scanner (Siemens Healthineers, Erlangen, Bavaria, Germany) used in the phantom and healthy volunteer studies for this thesis. At the time of this thesis' writing, 7T MRI was slowly growing into more routine clinical use as 7T commercial scanners were approved under the United States Food and Drug Administration (FDA) and the European Economic Area's *conformité européenne* (CE) standard regimes. These include the Terra. The Centre's 7T scanner is one of the first in the United Kingdom to be located in a clinical setting [104]. It also served as a collaboration interface for academic, clinical and industrial partners. All experiments on healthy subjects at this site received ethical approval from the local NHS Clinical Research Imaging Facility (CRIF) Approval Group [105].

The scan element of the work in Section 3.4.1 was performed on a MAGNETOM Skyra 3T scanner (Siemens Healthineers, Erlangen, Bavaria, Germany) during a research visit at the Fraunhofer Institute for Digital Medicine MEVIS, Bremen, Germany. This visit was funded under the Postdoctoral and Early Career Researchers (PECRE) award from the Scottish Imaging Network: A Platform for Excellence (SINAPSE) consortium.

### 3.3.2 Programs used for 7T MS-PACE technique development

A major element of this thesis is the development and validation of the 7T MS-PACE technique. This involved extensive developmental work in C++ programming language using Siemens' Integrated Development Environment for Applications (IDEA) pulse sequence development and ICE image reconstruction platforms (Syngo MR version VE11 until 2021, VE12U from 2021). The IDEA element of the developmental work involved integrating the technique into an EPI sequence originally developed in-house at the University of Glasgow by Prof David Porter. This involved the extensive integration of new codes and modules into the sequence code, which includes: enabling the sequence to receive the motion information feedback; enabling acquisition with the parallel imaging acceleration technique, in-plane generalised autocalibrating partially

### 3.3. Equipment

parallel acquisitions (GRAPPA); enabling fat saturation pulses; debugging and quality control codes such as embedding feedback slice indices on the measurement data header. The update using motion feedback was aided by a modified version of Siemens' product PACE module. The slice acquisition order was also modified so it acquired in an equidistant manner, e.g. for a 60-slice volume, the acquisition gap is 20 slices (0-20-40, 1-21-41, 2-22-42, etc). This was to synchronise it with multislice-to-volume registration technique and help to future-proof it for a potential simultaneous multislice application.

The development on the ICE platform involved extensive modification of the original 3T MS-PACE reconstruction algorithm [106] for the 7T application. This included: adding GRAPPA reconstruction modules; adapting and integrating the in-house EPI sequence reconstruction modules; adapting the reconstruction pipeline; reconfiguring the multislice-to-volume image registration functor. Shown in Figure 3.2, the reconstruction pipeline has two branches. The first is the real-time motion estimation branch, which directs data for motion calculation into the image registration functor and then feeds this information back to the sequence. The second is the normal reconstruction branch, which generates images.

The sequence was intensively phantom-tested at the 7T scanner to ensure it was safe and stable before being used in healthy volunteer experiments.

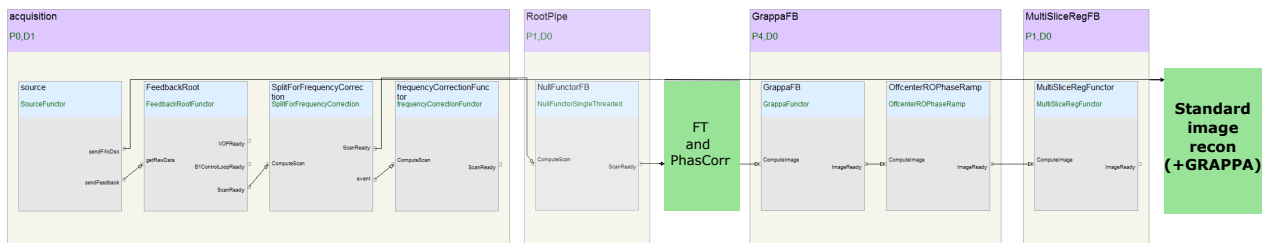


Figure 3.2: A truncated version of the ICE image reconstruction pipeline developed for the 7T MS-PACE technique, demonstrating how the data processing branches into two. On ICE, the pipeline is constructed with individual processing modules (functors) with input and output nodes that control data flow between them. The data branches out of the *source* functor to form a separate real-time motion calculation branch towards the *MultiSliceRegFunc* where motion estimation and feedback of motion parameters to the pulse sequence for real-time acquisition system updates occur. GRAPPA processing is also active in the real-time branch (*GrappaFB*). The other branch heads to the standard image reconstruction pipeline.

### 3.3.3 Phantom

Sequence testing was performed on a Siemens Solution J spherical phantom (Siemens Healthineers, Erlangen, Bavaria, Germany), which has a yellow fat to polydimethylsiloxane oil ratio of

0.05:1000. All phantom tests were conducted at the 7T Terra scanner with the coils relevant to each study.

### 3.3.4 Coils

The work described in this chapter and in the following Chapter 4 utilised a single-channel transmit, 32-channel receive channel head coil (Nova Medical, Wilmington, MA, USA). The work in Chapter 5 used a different coil, which was an 8-channel transmit, 64-channel receive head coil (MR CoilTech Ltd, Glasgow, Scotland, UK). For the specific work described in Section 3.4.1, the coil used was a single-transmit, 20-channel receive head coil (Siemens Healthineers, Erlangen, Bavaria, Germany).

## 3.4 Methods

The process of adaptation and integration of the technique for 7T EPI application involved scientific evaluations of different aspects of the technique and sequence and image reconstruction algorithm development. As feedback speed is essential for prospective motion correction, the experiment described in section 3.4.1 was conducted to evaluate the effect of the number of slices in the multislice subset. Section 3.4.2 then evaluated the sensitivity of the technique to sub-TR intra-volume motion.

Following pulse sequence development and integration of the feedback system into an in-house EPI as described in Section 3.3.2, 7T MS-PACE was then validated for use in fMRI protocols, described in Section 3.4.3

### 3.4.1 Motion detection: the effect of the number of slices in the registration subset

*(Published in [107][108][109])*

One aspect that was considered during the development is the possibility of using different numbers of slices in a multislice navigator subset. This was evaluated in order to find the ideal balance between the temporal resolution advantage by using fewer slices and registration accuracy.

The initial study was performed using retrospective reconstruction of scan data acquired from a healthy 28-year-old subject on a MAGNETOM Skyra 3T scanner (Siemens Healthineers, Erlangen, Bavaria, Germany) with a single-transmit, 20-channel receive head coil (Siemens

### 3.4. Methods

---

Healthineers, Erlangen, Bavaria, Germany). Two gradient echo EPI time series were acquired (98 volumes, 39 slices, TR 3000ms, TE 30ms, matrix size 64×64, slice thickness 3mm) using a Siemens product sequence. The time series was acquired: 1) without instructed motion; 2) with instructed motion. The motion protocol instructed through the intercom system was: 1) nodding down; 2) nodding up; 3) back to neutral position and 4) right-tilting. No prospective motion correction was applied during the scan. The translational and rotational parameters were calculated offline post-scan using an algorithm developed using ICE. Motion parameters were estimated from both time series using the following numbers of equidistantly-spaced slices in the registration subset: 2, 3, 4, 6, 12, 18. For comparison, a volume-to-volume registration was also performed (as in PACE [5]).

#### 3.4.2 Motion detection: the effect of intra-volume motion

*(Published in [110])*

The standard PACE technique, which uses volume-to-volume registration, is unable to capture intra-volume motion. MS-PACE, which instead uses subsets of EPI slices for navigation, has the potential to be used for this purpose. A study was conducted to investigate motion detection in the presence of intra-volume motion, comparing the multislice-to-volume registration approach to that of the original volume-to-volume method.

The study was performed by reconstructing and analysing data acquired in vivo from a healthy 26-year-old volunteer using a MAGNETOM Terra 7T scanner (Siemens Healthineers, Erlangen, Bavaria, Germany) with a single-transmit, 32-channel receive head coil (Nova Medical, Wilmington, MA, USA). A 2D gradient echo EPI with BOLD (blood oxygen level dependent) contrast brain image set was acquired (50 volumes, 36 slices, TR 2310ms, TE 25ms, slice acceleration factor 3, matrix size 128×128) using a Siemens product sequence. The subject was instructed to perform head movements along the x, y and z-axes during the scan. Using a processing algorithm developed in Siemens ICE, the first volume was set as the reference volume and multislice subsets from the subsequent volumes were registered against it. Two image registrations were performed: 1) full volume; 2) multislice subsets of 3 equidistant slices using rigid-body image registration. Translational and rotational parameters were then obtained.

#### 3.4.3 Application to real-time motion correction in fMRI protocol

*(Published in [111][112])*

After the previous studies on the technique's capabilities and limits, the technique was developed further in Siemens IDEA and ICE. The mature version of the technique was then validated

for use in functional MRI (fMRI) protocols. Compared to lower field strengths, functional MRI (fMRI) at 7T benefits from an improved inherent signal-to-noise ratio (SNR), higher BOLD contrast, and there is evidence of a greater spatial selectivity [59]. These benefits are most easily achieved at a high spatial resolution, where the noise in the image is less dominated by physiological contributions, making 7T highly suitable for the detailed mapping of neural activity, such as in the investigation of differential activity in the cortical layers. However, this high spatial resolution leads to a greater sensitivity to motion artefacts during the long time series used in standard fMRI protocols. These artefacts are typically mitigated with retrospective motion correction [113]. Alternatively, prospective motion correction can be performed by applying corrections to the acquisition system in real time, reducing the effects of spin history and interpolation [114]. The restricted environment in 7T scanners (i.e. narrower bores, tighter head coils) makes markerless, non-hardware techniques an attractive choice. This section evaluates the implementation of MS-PACE for 7T functional MRI (fMRI). A variant of this method has previously been implemented for fMRI at 3T [106].

Unlike in the previous implementation at 3T, the 7T implementation also includes the use of the parallel imaging technique in-plane GRAPPA [7]. This technique helps to reduce spatial distortion effects in EPI that are more pronounced in 7T [8]. Despite the extra processing needed with the integration of GRAPPA reconstruction, it was still possible to perform multislice-to-volume registration with high temporal resolution of scan updates.

The initial validation study was performed on a MAGNETOM Terra 7T scanner (Siemens Healthineers, Erlangen, Bavaria, Germany) with a single-transmit, 32-channel receive head coil (Nova Medical, Wilmington, MA, USA) using an in-house-developed EPI sequence on 3 healthy volunteers (age  $31 \pm 5$ ). The scan protocol consisted of four acquisitions, two without and two with MS-PACE motion correction. The subject was blinded to the acquisition order. Beside the motion correction, the scan parameters for both scans were identical: isotropic voxel size  $2 \times 2 \times 2 \text{mm}^3$ , resolution  $96 \times 96$ , GRAPPA factor 3, 60 slices, 100 volumes, echo spacing 580ms, TR 7s, TE 18ms and total acquisition time 12m1s. Figure 3.1 shows how the motion detection and correction pipeline operates.

Each multislice subset used for registration had 3 equidistant slices, i.e. for a 60-slice volume, the gap is 20 slices (indices of slice groups: 0-20-40, 1-21-41, 2-22-42, etc). Calculated motion parameters were then fed back to the scanner system and the imaging gradients were subsequently updated to account for the preceding movements. The threshold for correction was set for translation and rotation of 0.2mm and  $0.2^\circ$  respectively.

Residual rigid body motion parameters (translation and rotation in x, y and z axes) were also retrospectively calculated using the multislice-to-volume method. Online and offline process-

## 3.5. Results

---

ing were done within ICE (Siemens Healthineers, Erlangen, Germany) using ITK open-source image registration libraries. The residual motion parameters were compared for all subjects.

Voxelwise temporal SNR (tSNR) comparison was made between the non-corrected and corrected cases. These maps illustrate the temporal variance in noise and were calculated by comparing the mean signal of each voxel to its standard deviation over the time series.

$$tSNR = \frac{\text{mean of the time series}}{\text{standard deviation of the time series}} \quad (3.1)$$

The technique was also compared to FSL's MCFLIRT (Motion Correction FMRIB's Linear Image Registration Tool) [115]. The time series data was calculated retrospectively using the multislice-to-volume method and MCFLIRT and then compared. The reference volume parameter for the MCFLIRT calculations was set to be the first volume, akin to the multislice-to-volume method, instead of the default middle volume.

In order to expedite the calculation of motion parameters and consequently the feedback speed, evaluation by randomised spatial masking in the image registration step was enabled. Instead of using the whole image to evaluate the metric, voxels are randomly subsampled from the image. This was first evaluated by retrospectively calculating the motion parameters from data from one subject, with the random masking enabled. This feature was then enabled on the sequence in the scanner and the effects on motion correction were examined in a subject.

## 3.5 Results

### 3.5.1 Motion detection: the effect of the number of slices in the registration subset

Figure 3.3 shows x-axis (left-right) translation estimates for the different numbers of slices for image registration and compares them to results from the volume-to-volume registration. The jump at 230s is caused by the right-tilting motion. Figure 3.4 and 3.5 compare respectively the translational and rotational parameters along the three spatial axes for the motion-affected dataset.

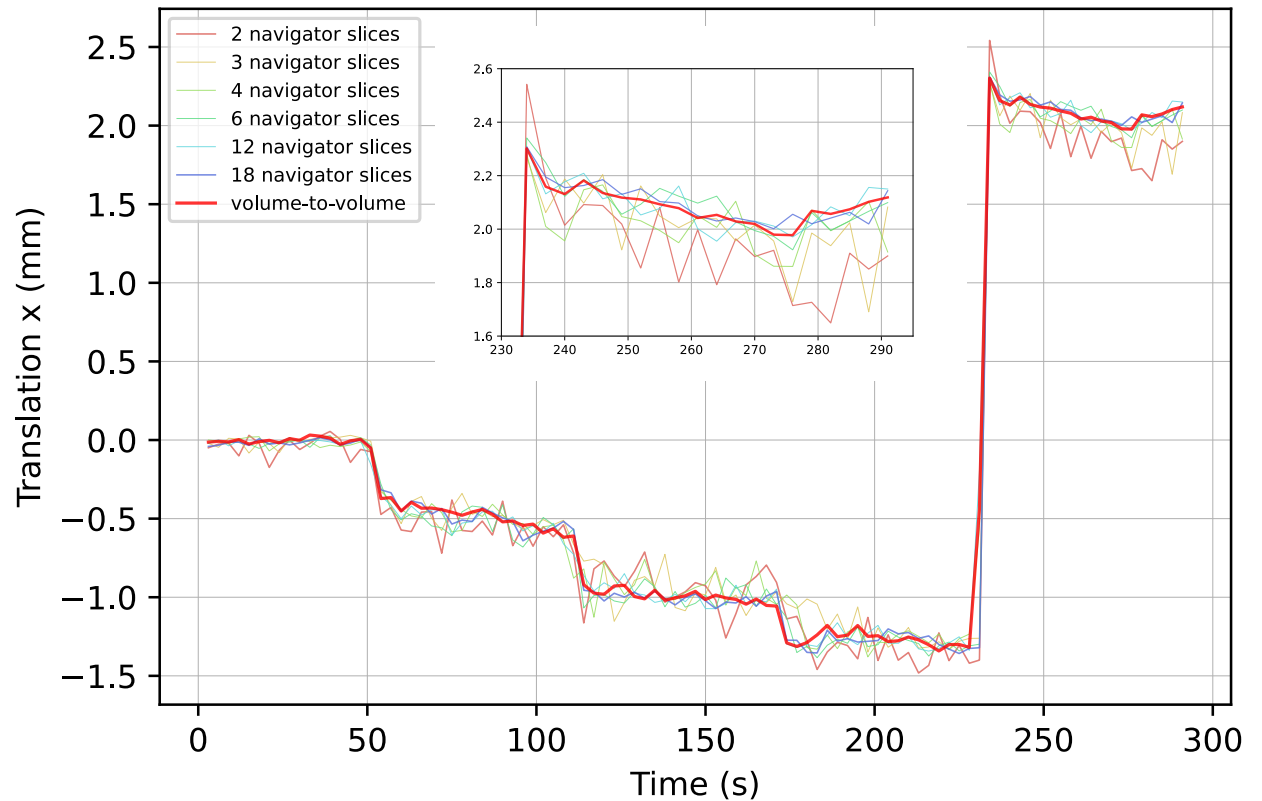


Figure 3.3: X-axis translation parameters acquired from the registration of the motion-affected dataset. The red curve signifies the reference volume-to-volume registration. The fewest (2) and the most (18) image registration slices cases are highlighted with bolder colours. The inset focuses on the 230-300s time window (post the right-tilting motion).

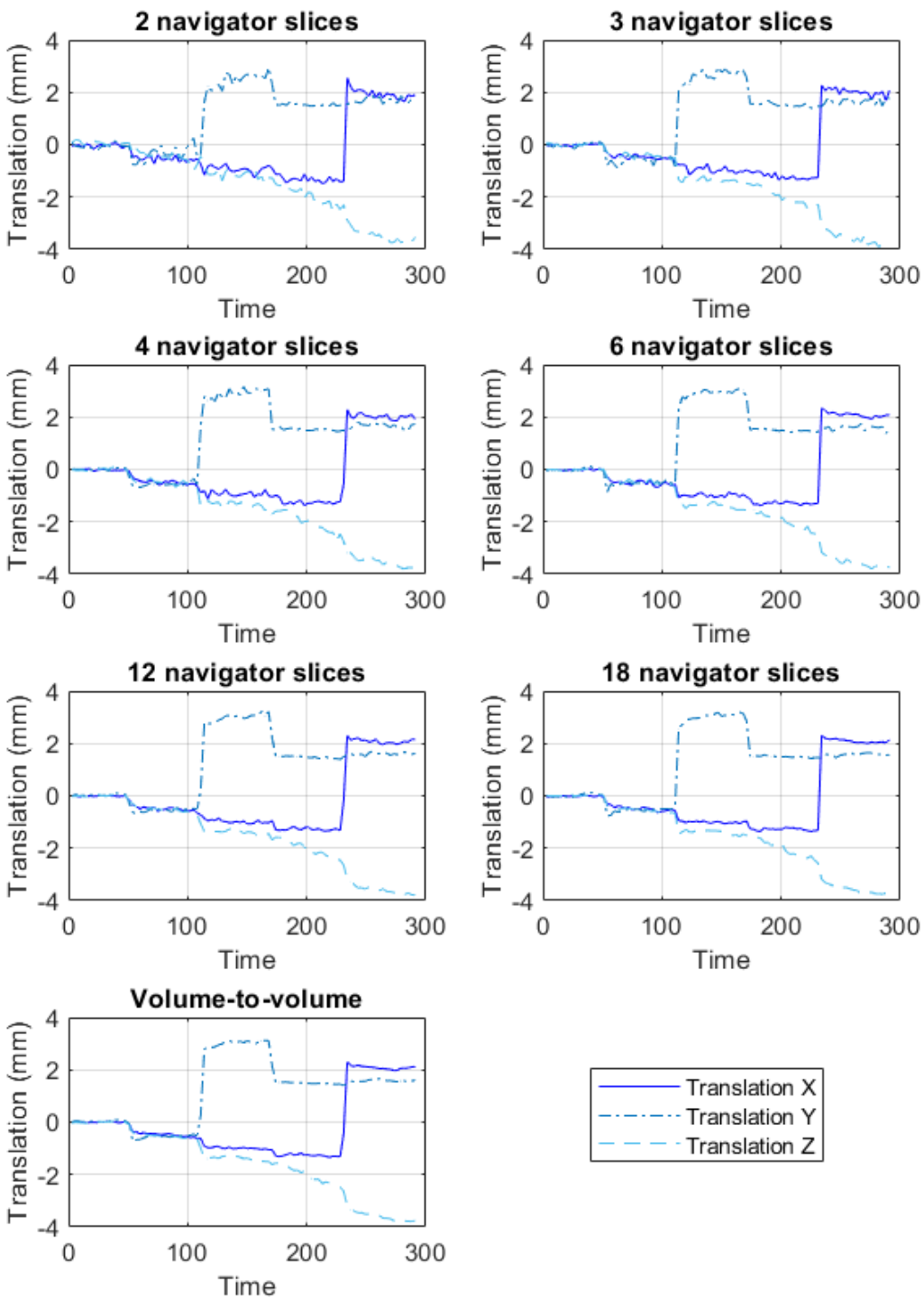


Figure 3.4: Translation parameters across the three spatial axes acquired from the registration of the motion-affected dataset with variable numbers of navigator slices.

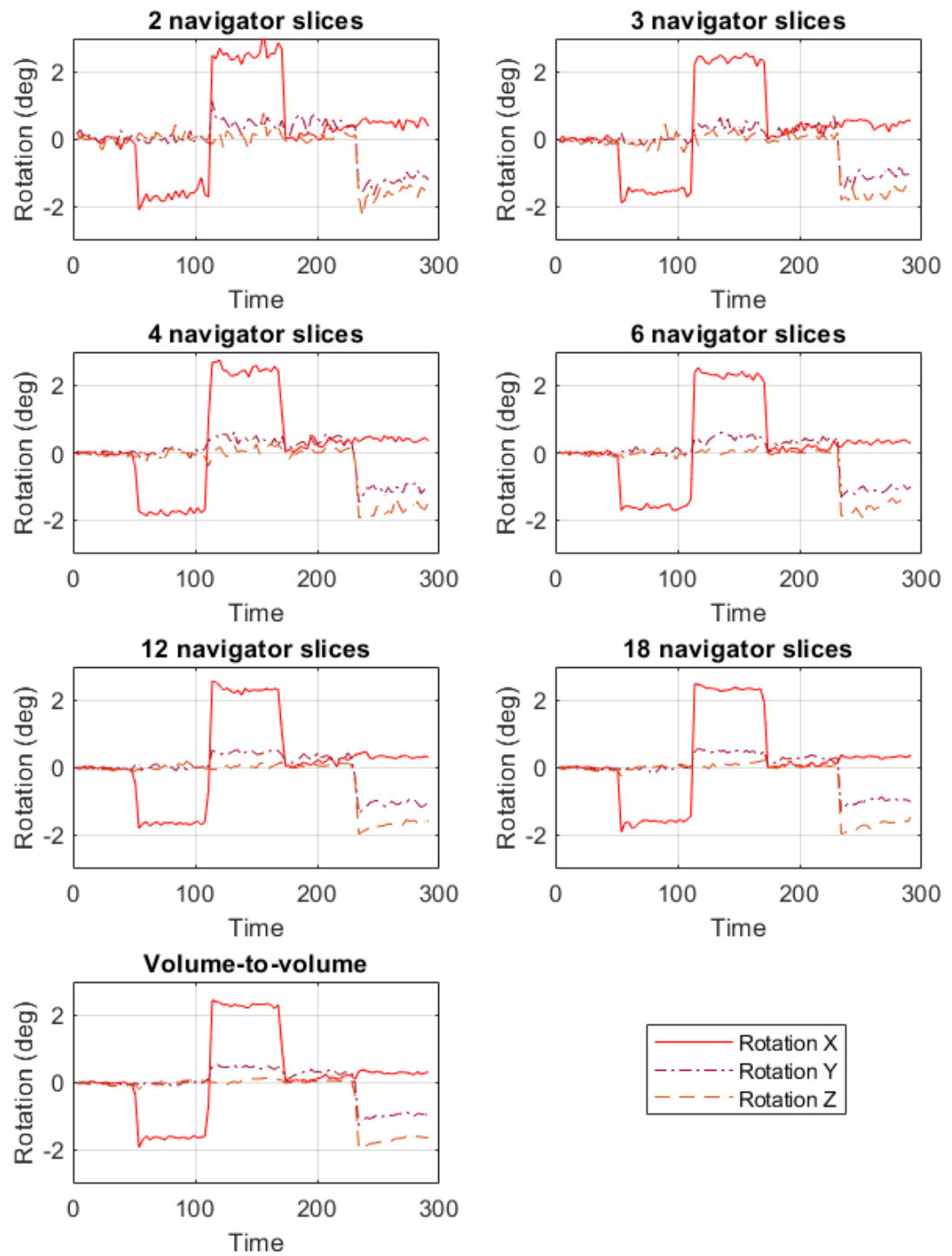


Figure 3.5: Rotation parameters across the three spatial axes acquired from the registration of the motion-affected dataset with variable numbers of navigator slices.

### 3.5.2 Motion detection: the effect of intra-volume motion

Figure 3.6 shows a comparison of volumes unaffected (a) and affected (b) by intra-volume motion. Figure 3.7 shows translation and rotation calculations for the full volume (blue line) and multislice subset (red points) registrations. The time intervals during which multidirectional intra-volume motion occurred are highlighted in grey.

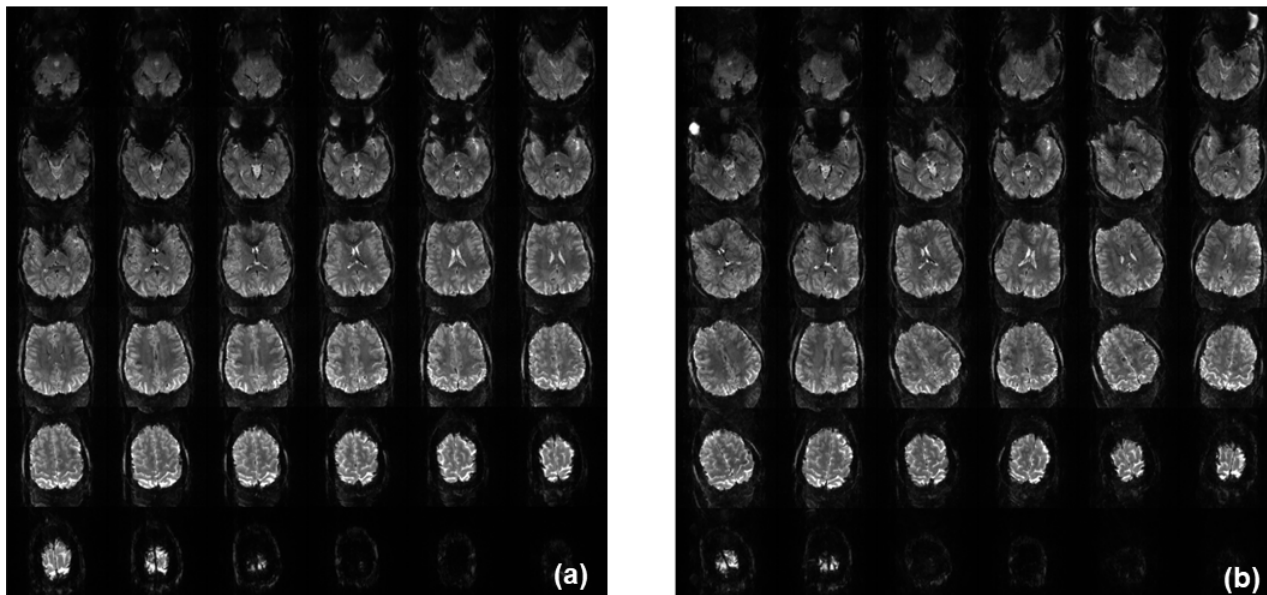


Figure 3.6: A BOLD-EPI volume unaffected (a) and affected (b) by multidirectional intra-volume motion.

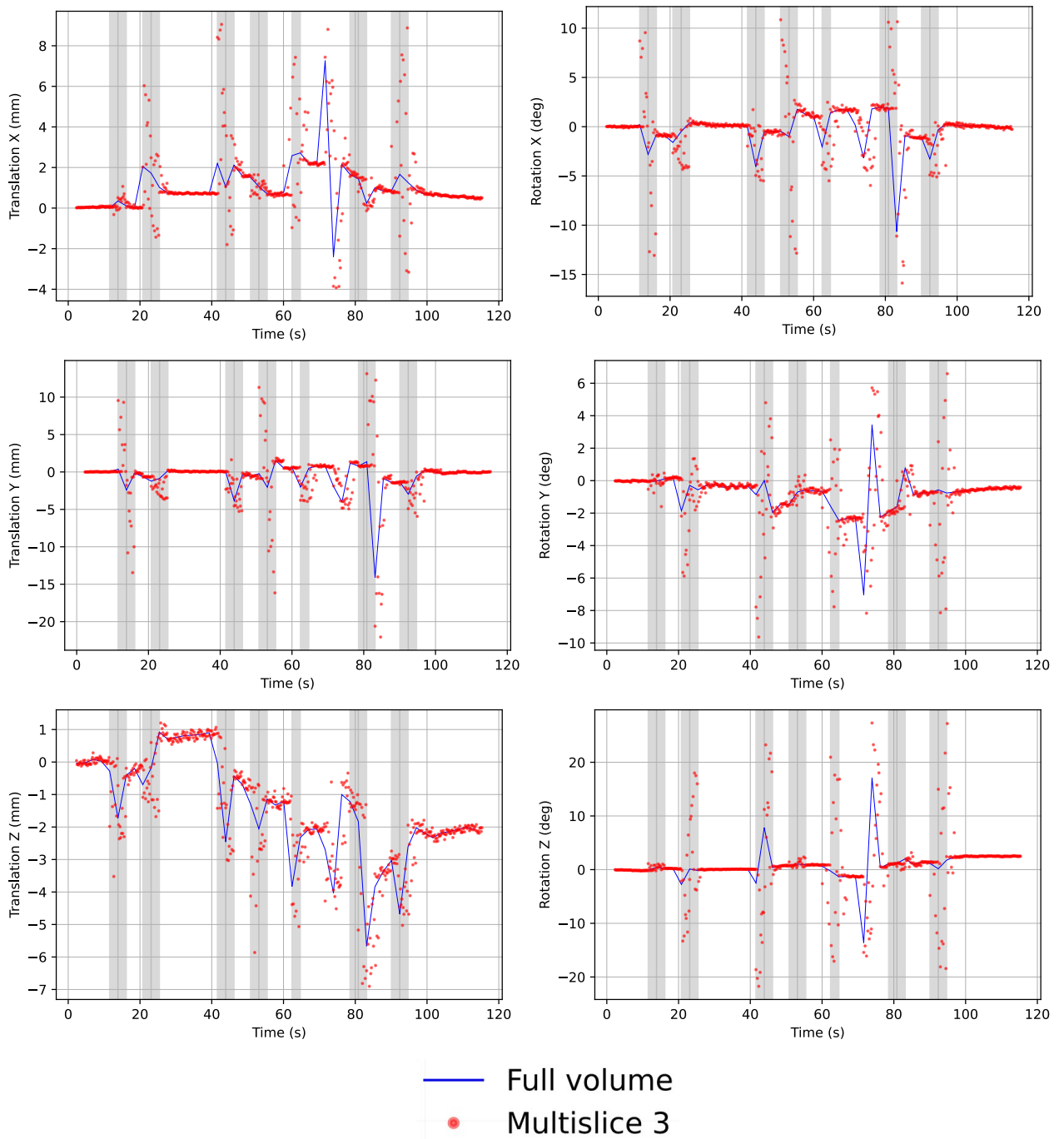


Figure 3.7: Translation and rotation parameters in both registration schemes. Blue curve shows full volume registration, red points show multislice-subset registrations. Volumes affected by intra-volume motion highlighted in grey. The translation parameters are in the left column, while the rotation ones are in the right column.

### 3.5.3 Application to real-time motion correction in fMRI protocol

Figure 3.8 shows the comparisons of the retrospectively-calculated rigid-body motion parameters from one subject. Figure 3.9 summarises this in a box plot format.

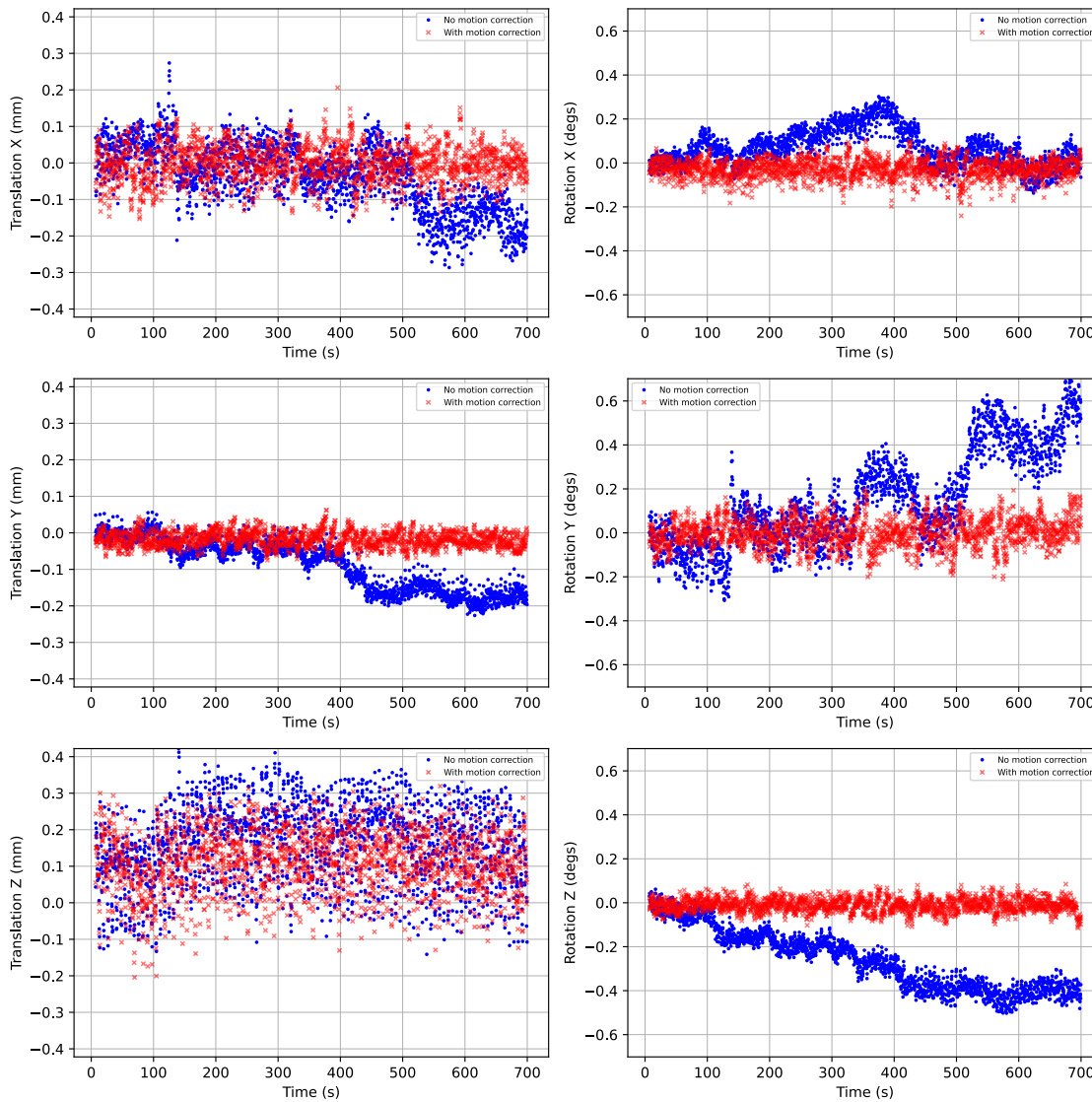


Figure 3.8: Rigid-body motion parameter estimates (x, y and z-axes) from the acquisitions without (blue) and with (red) real-time motion correction. The translation parameters are in the left column, while the rotation parameters are in the right column.

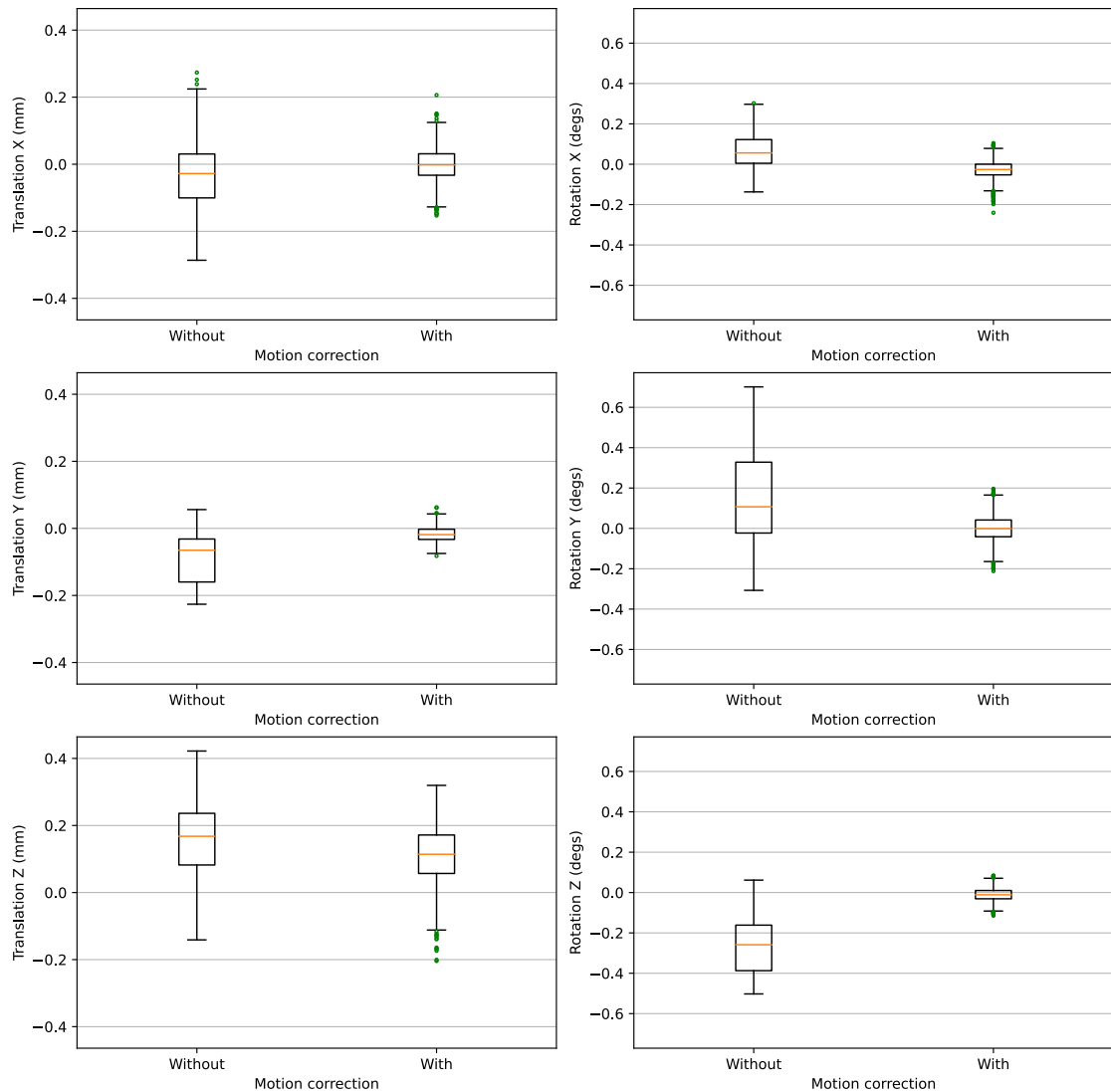


Figure 3.9: Box plot representation of the rigid body motion parameter estimates (x, y and z-axes) from the acquisitions without and with real-time motion correction. The translation parameters are in the left column, while the rotation parameters are in the right column. Each box includes the interquartile range (IQR) of the parameter values. The red line represents the median. Each whisker extends to the furthest data point in each wing that is within 1.5 times the IQR. Data points outside this range are represented by the outlier dots.

### 3.5. Results

Figure 3.10 then shows voxelwise temporal SNR (tSNR) maps for each slice, with and without motion correction. These maps illustrate the temporal variance in noise and were calculated by comparing the mean signal of each voxel to its standard deviation over the time series.

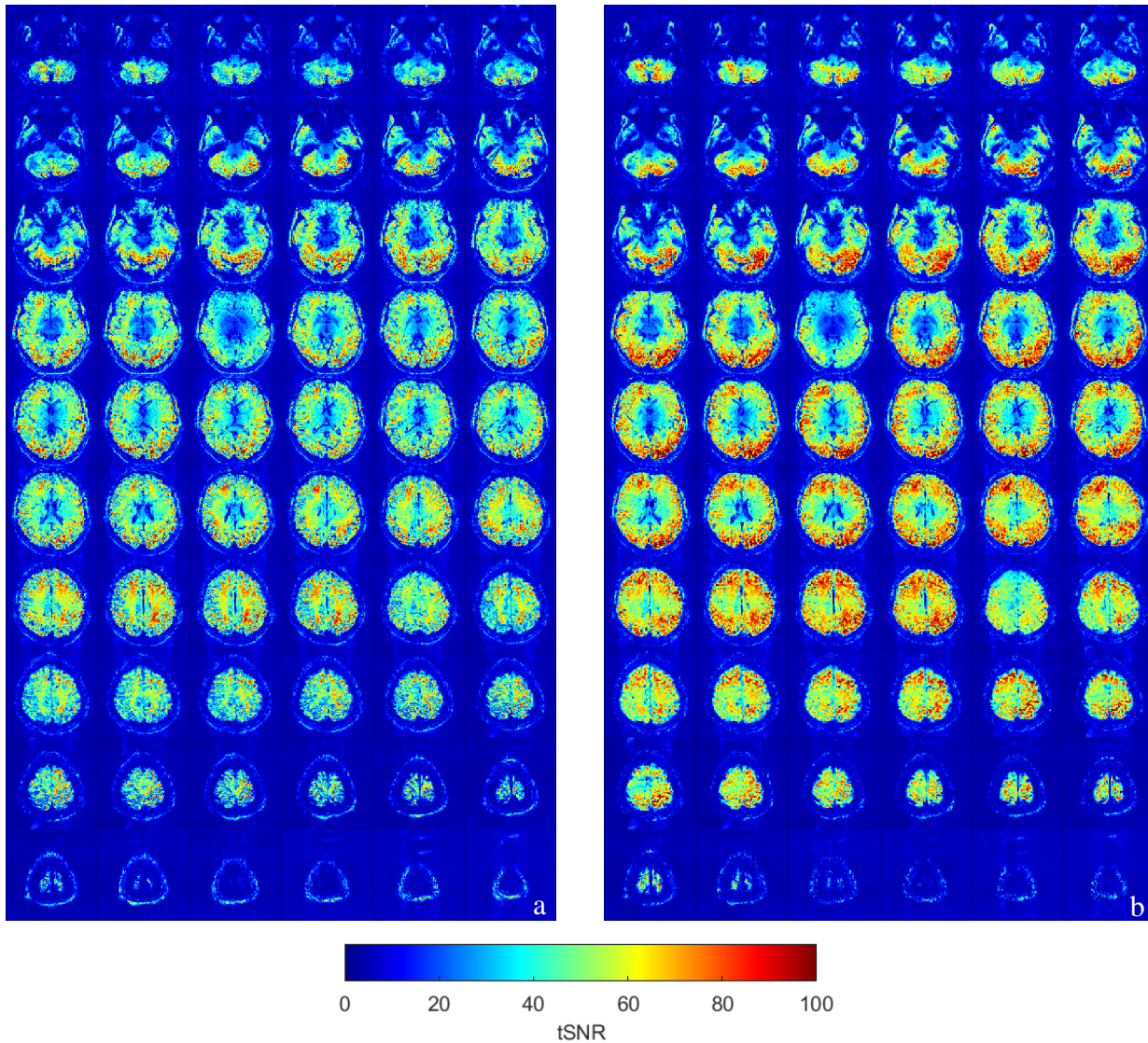


Figure 3.10: Temporal SNR (tSNR) maps from a single subject without (a) and with (b) real-time motion correction. These maps illustrate the temporal variance in noise and were calculated by comparing the mean signal of each voxel to its standard deviation over the time series. An improvement in tSNR is observed in (b).

The motion parameter calculations from the three subjects were aggregated into Figures 3.11 and 3.12. The former shows the rigid body translation parameters (x, y and z-axes), while the latter shows the rotation parameters. The plots are set to uniform axes to illustrate the varying tendencies of each subject to involuntary movement.

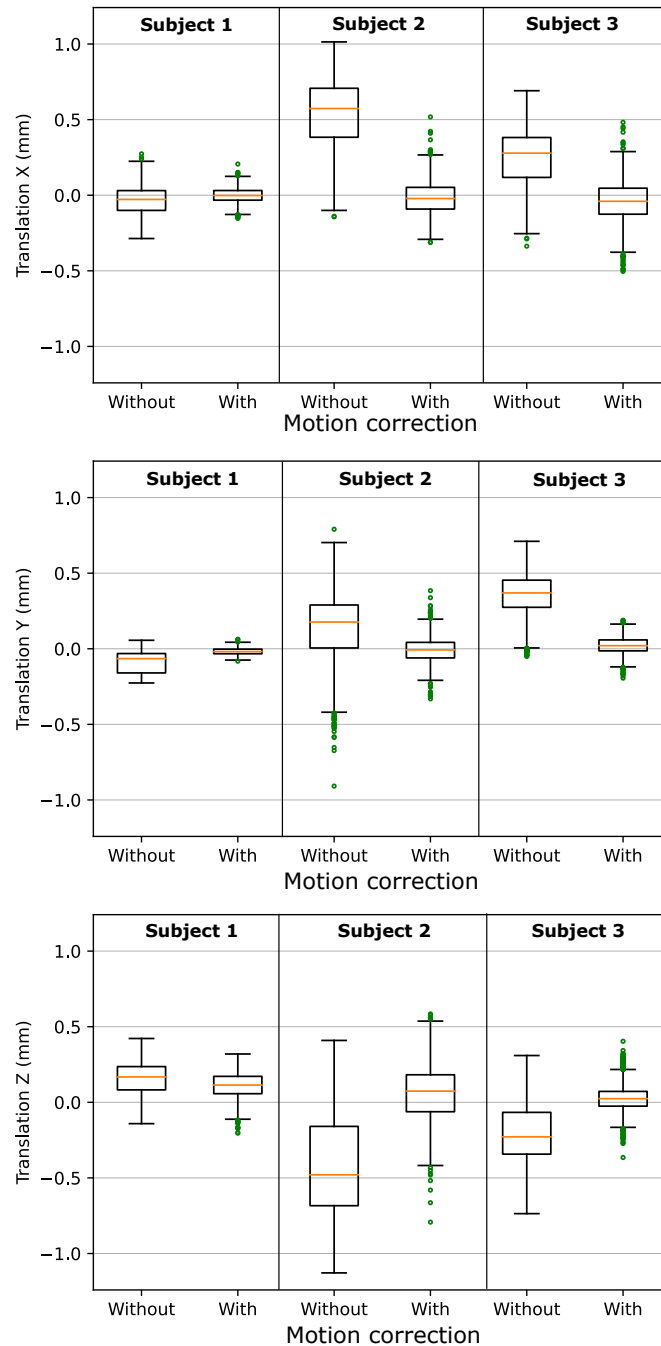


Figure 3.11: Comparison of the non-corrected and corrected translation parameter estimates (x, y and z-axes) from three separate subject acquisitions using the same protocol.

### 3.5. Results

---

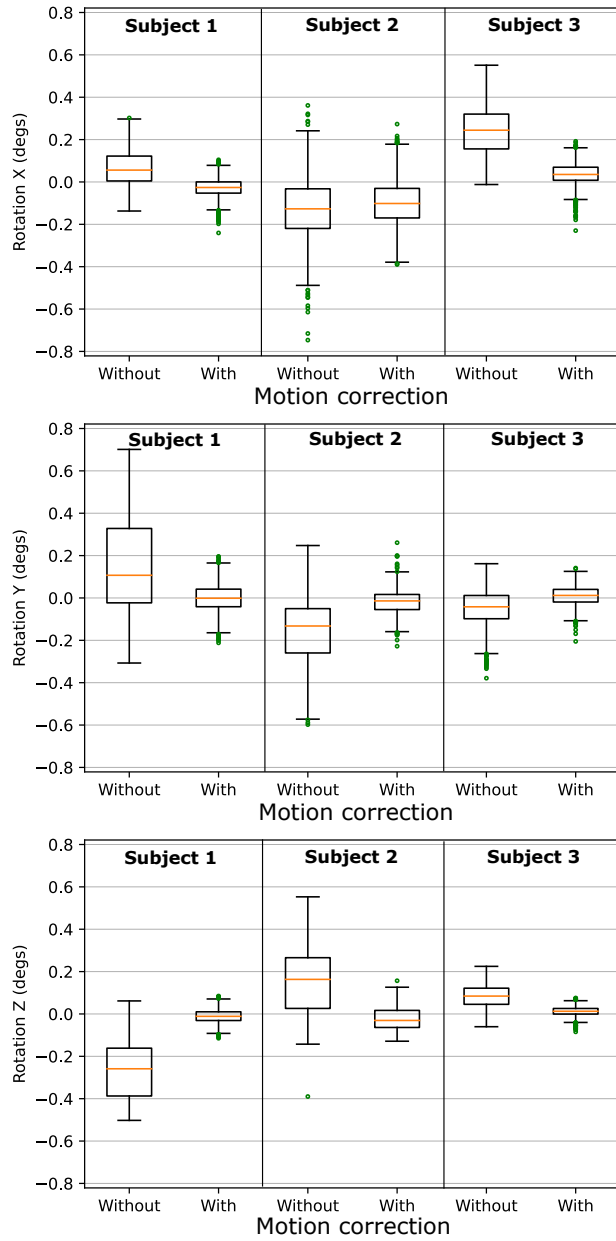


Figure 3.12: Comparison of the non-corrected and corrected rotation parameter estimates (x, y and z-axes) from three separate subject acquisitions using the same protocol.

Table 3.1 presents Figures 3.11 and 3.12 numerically, displaying mean and standard deviation values. A statistical test was applied to the averages. Table 3.2 present the Student t-test of the averages of each rigid body motion parameter of the data corrected with MS-PACE against those without.

MoCo		Off			On		
Subject		1	2	3	1	2	3
Translation	x	-0.04±0.89	0.52±0.24	0.24±0.20	-0.00±0.05	-0.02±0.01	-0.04±0.13
	y	-0.08±0.07	0.13±0.23	0.34±0.16	-0.02±0.02	-0.01±0.08	0.02±0.05
	z	0.16±0.11	-0.41±0.34	-0.21±0.18	0.11±0.08	0.06±0.18	0.03±0.09
Rotation	x	0.07±0.08	-0.13±0.14	0.24±0.11	-0.03±0.04	-0.10±0.11	0.04±0.05
	y	0.15±0.22	-0.16±0.17	-0.05±0.09	-0.00±0.06	-0.02±0.06	0.01±0.04
	z	-0.26±0.14	0.16±0.14	0.08±0.05	-0.01±0.03	0.02±0.05	0.01±0.02

Table 3.1: Mean and standard deviation ( $mean \pm SD$ ) of the non-corrected and corrected translation and rotation parameter estimates (x, y and z-axes) from three separate subject acquisitions.

Parameter		Mean parameter t-test
Translation	x	t(2) = -1.80, p = 0.21
	y	t(2) = -2.24, p = 0.15
	z	t(2) = -2.17, p = 0.16
Rotation	x	t(2) = -1.61, p = 0.25
	y	t(2) = -2.97, p = 0.10
	z	t(2) = -2.93, p = 0.10

Table 3.2: The results of Student t-test comparing the means of each rigid body parameter from scans with against without prospective motion correction. The numbers in parentheses signify the degrees of freedom in each statistical calculation, which is the number of pairs evaluated subtracted by 1.

### 3.5. Results

The residual motion parameters calculated with the multislice-to-volume method were then compared against image registration results from FSL's MCFLIRT tool. Figure 3.13 shows the comparison of rigid body translation parameters between the two algorithms from one subject data. Figure 3.14 shows the comparison of rotation parameters.

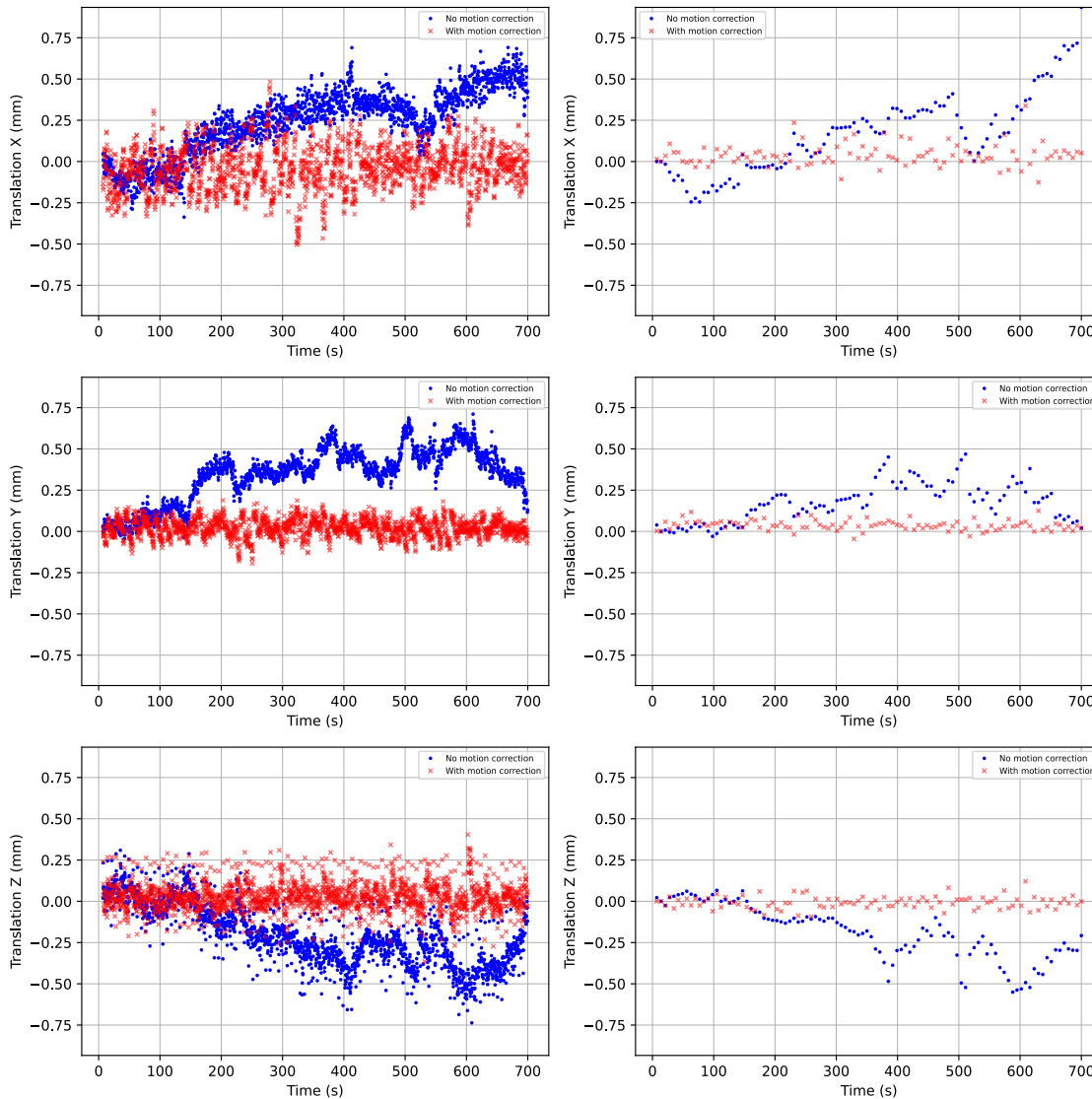


Figure 3.13: Comparison of the residual translation parameters calculated from a single subject with the multislice-to-volume method (left column) and with FSL's MCFLIRT tool (right column) from the acquisitions without (blue) and with (red) real-time motion correction.

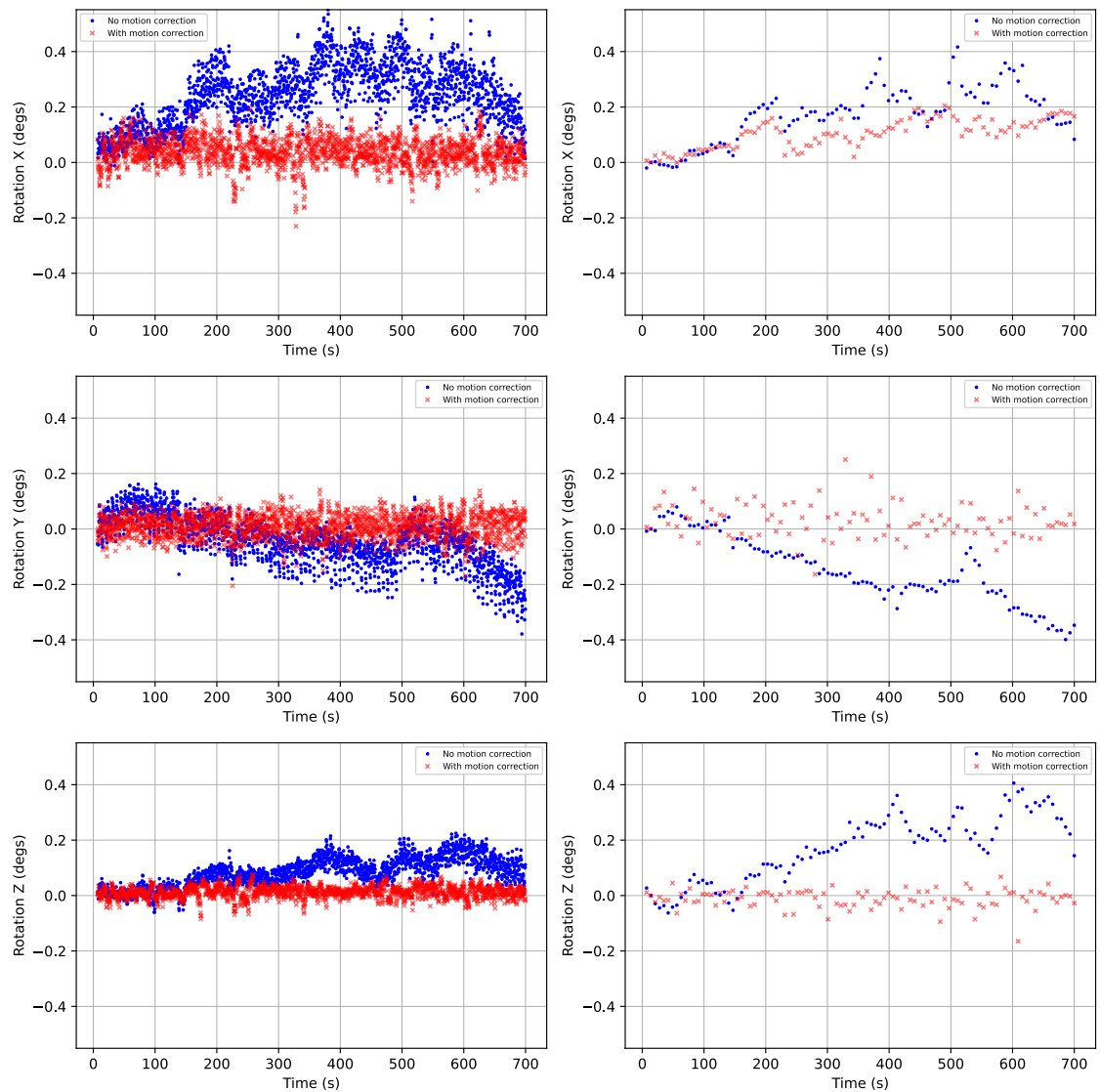


Figure 3.14: Comparison of the residual rotation parameters calculated from a single subject with the multislice-to-volume method (left column) and with FSL's MCFLIRT tool (right column) from the acquisitions without (blue) and with (red) real-time motion correction.

### 3.5. Results

To evaluate the impact of the addition of spatial masking for the image registration step of the motion detection, the residual motion parameters from one subject was retrospectively calculated with the results displayed in Figure 3.15.

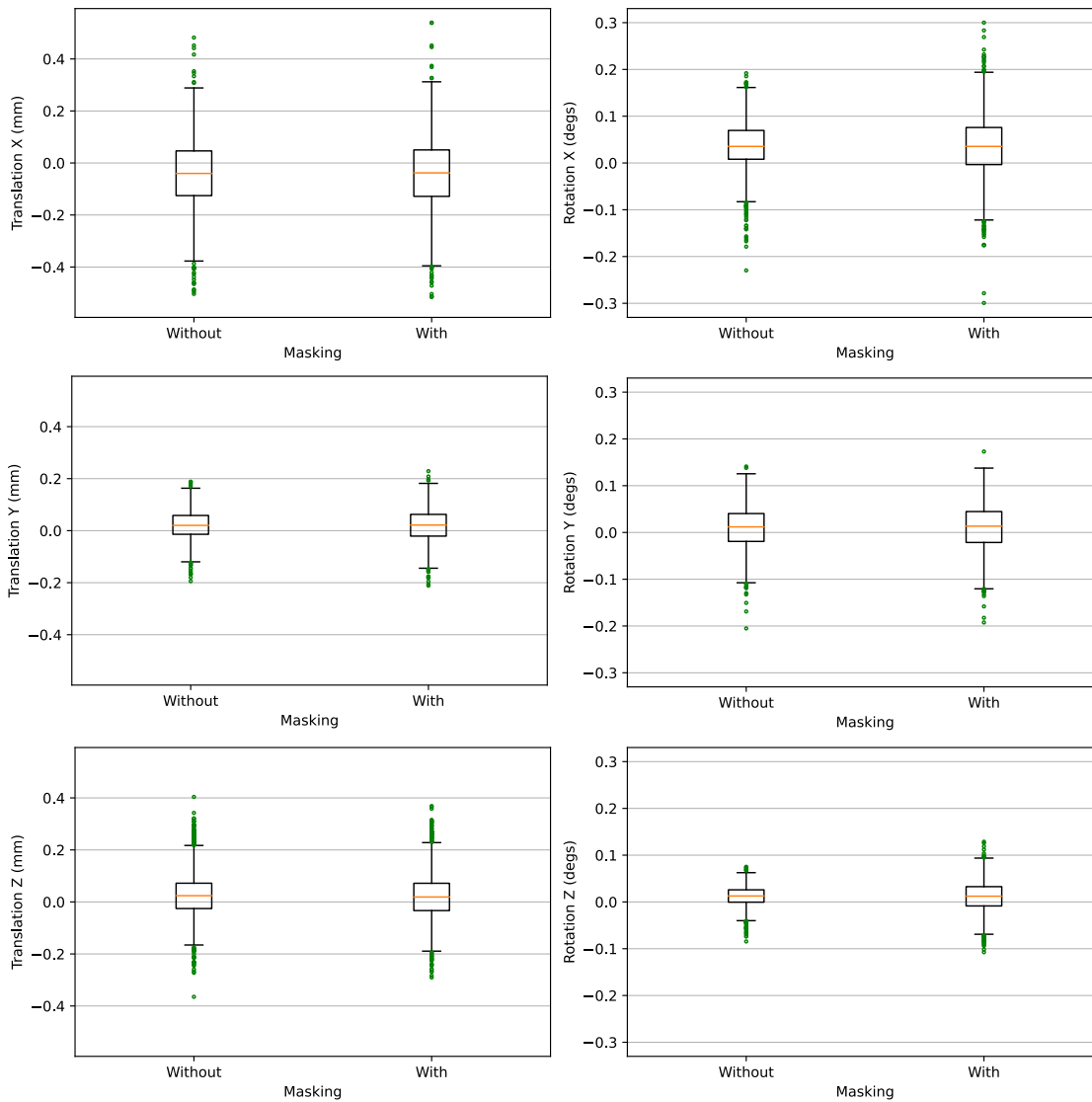


Figure 3.15: Comparison of the rigid body motion parameter estimates with motion correction applied and with motion correction plus masking. These were retrospectively calculated post-acquisition. The data are derived from one subject.

This feature was then added into the sequence's reconstruction pipeline. The updated sequence was evaluated on a subject and the same comparison was made, displayed in Figure 3.16.

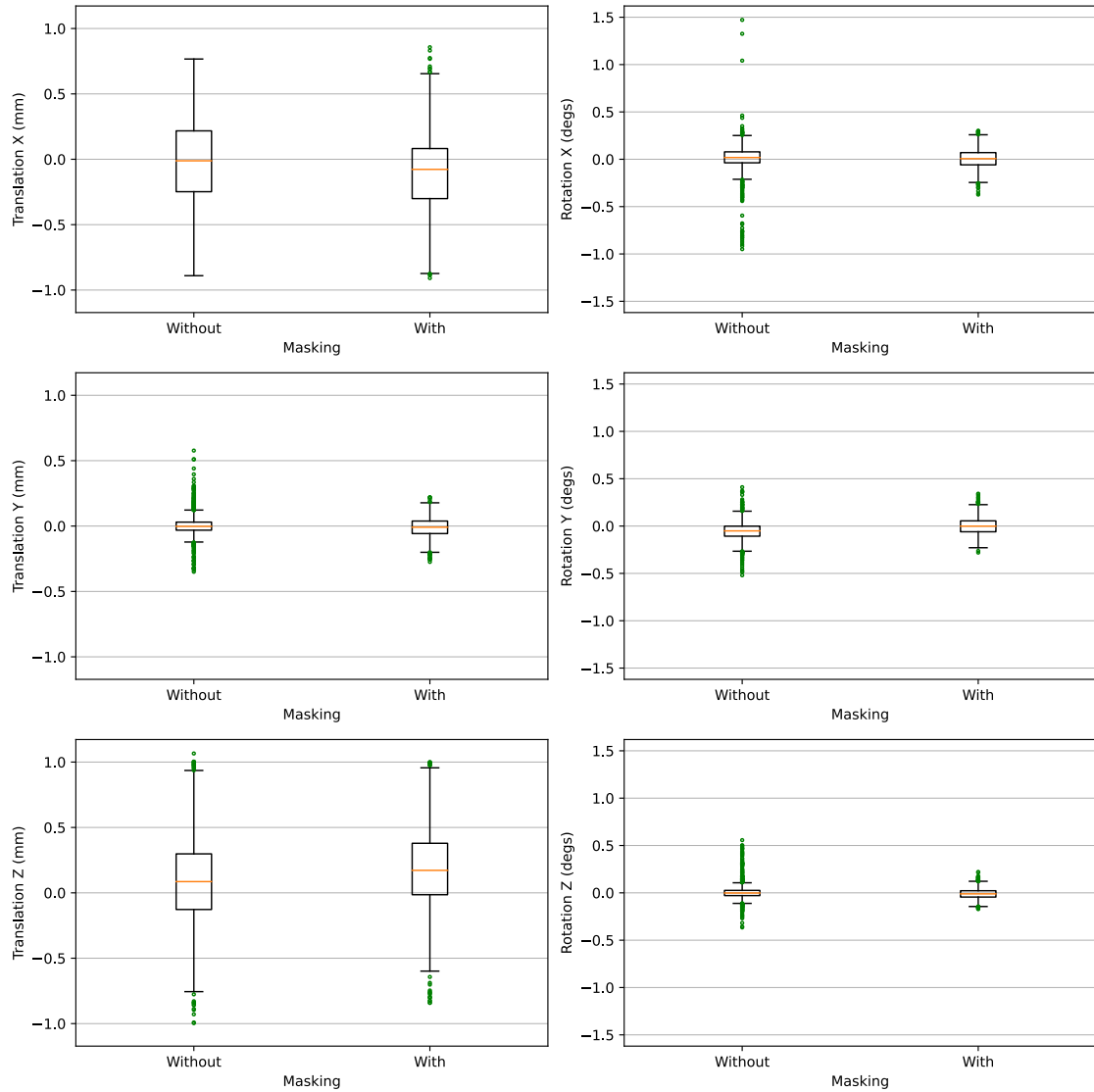


Figure 3.16: Comparison of the rigid body motion parameter estimates from a subject dataset acquired with the masking-enabled sequence, with motion correction applied and with motion correction plus masking.

## 3.6 Discussion

### 3.6.1 Motion detection: the effect of the number of slices in the registration subset

The results suggest that the use of fewer slices for the navigation subsets, i.e. two or three slices, could yield an image registration accuracy comparable to volume-to-volume registration. As seen in Fig 3.4 and 3.5, the lower extreme of the range used in the experiment, two slices, achieved a registration profile that is close to the volume-to-volume (36 slices) case. However when inspected closely in Fig 3.3, which shows the x-axis translation comparison for all scenarios, the differences between the two cases are more noticeable and significant. Using three slices provided a closer approximation to the volume-to-volume case, but also would be much faster than using volume-to-volume registration, particularly for a large number of acquired slices. The standard deviation between the two slices and full volume scenarios are 0.123mm, while it's lower at 0.101mm with three slices. Implementing a three-slice multislice-to-volume registration allows frequent sub-TR motion detection and correction for protocols with slice-dense volumes, but also with less accuracy penalty than when using two slices.

### 3.6.2 Motion detection: the effect of intra-volume motion

Figure 3.7 suggests that for volumes affected by intra-volume motion, multislice registration identified additional motion components that were not detected by the volume-to-volume registration, which averaged the different motion components occurring in the registered volume. This is shown in the grey-highlighted areas. These data do not prove definitively that the additional motion components detected by the multislice registration correspond to true motion events due to the feedback lag. A more definitive result could potentially be achieved, for example by correlating with optical tracker data, or by using a mechanical phantom with programmable defined movement. However, the good agreement with whole-volume registration during the time intervals without intra-volume motion in Figure 3.7 suggests that the multislice motion parameter estimates are reliable. The results demonstrate that multislice-to-volume registration possesses more sensitivity in detecting intra-volume motion occurring within a TR.

### 3.6.3 Application to real-time motion correction in fMRI protocol

As seen in the motion parameter estimates for the acquisition without motion correction (Figure 3.8), the volunteer was subject to longer-term motion, which increased as the scan progressed.

This is also consistent with the other subjects in this cohort, who were scanned with the same long protocol. The aforementioned figure also shows how the motion parameters after prospective motion correction are closer to zero, indicating successful motion detection and real-time adjustment of the imaging volume. It is also observed in Figure 3.8 and 3.9 that there's typically a higher variance in the through-plane motion parameters (translation Z, rotation X and Y) compared to the in-plane ones (translation X and Y, rotation Z). 3.9, a box plot comparison of the motion parameters, also demonstrates this effect. This is due to the through-plane resolution's dependence on the number of slices [108]. Figure 3.10 demonstrates an improvement in voxelwise tSNR in the acquisition with motion correction, noting that no retrospective motion correction was applied to either dataset.

Aggregating data from three subjects scanned under the same protocol, seen in Figure 3.11, Figure 3.12 and Table 3.1, it can be observed that the motion correction and detection were working consistently in each subject. The technique worked with the different involuntary motion tendencies of the subjects. This is also reflected in the statistical Student t-test evaluation of the average rigid body motion parameters in Table 3.2. The values are all negative, indicating that the motion correction resulted in overall decrease in residual motion parameters. Note that the p-values do not cross below the 0.05 threshold, which indicates statistical significance. This is due to the relatively small size of compared data. Another qualifier to these observed improvements is that all the acquisitions, corrected or not, were separate, which mean each was not affected by identical sets of involuntary motion. Larger-cohort studies are required to more strongly validate this, which was performed in Chapter 4. The blinding of the scan order was an important protocol feature for limiting biases.

Comparing the multislice-to-volume method and FSL's MCFLIRT (Figures 3.13 and 3.14) motion parameter calculations demonstrate similar residual motion component directions and patterns in both methods. As the former calculates motion parameters multiple times within a TR and volume, there is a higher temporal resolution of motion detection and adjustment compared to the latter, which uses volumetric image registration. In MCFLIRT, an intra-volume motion component is averaged with other motion components occurring in the same volume, instead of detected as a separate component. However, the multislice-to-volume method returns less precise spread of through-plane parameters compared to MCFLIRT due to the z-dimension resolution's dependence on the number of slices [108].

Although a sub-TR correction rate was achieved, the 7T implementation initially had the limitation of a feedback lag of 350-700ms, which was relatively long compared to the previous implementation at 3T. To remedy this issue, several avenues were explored. First, randomised spatial masking was added in the image registration step of the motion parameter calculation.

### 3.7. Conclusion

---

This reduces the number of pixels used during image registration and speeds up the computation time during this step. The initial application of this method on a previously-acquired dataset showed detection that is close to the original correction that used no masking. As Figure 3.15 shows, the motion estimates in the masked case are close to the non-masked case. The former has a slightly higher variance but still approximates to the latter and crucially to zero, which indicates successful motion correction. Figure 3.16 also confirms that masking didn't introduce significantly-deleterious effects to the motion correction capacity in the masking-enabled version of the sequence. When masking was enabled, the correction was not as accurate as when full-sampling as used, i.e. increased residual motion was detected. However as observed in the figure, this difference is very small. Considering the benefits of being able to use a much shorter TR, this feature returns more positive impacts. After this was implemented, the feedback lag was down to  $\approx 179$ ms. A potential area of improvement is the image registration pipeline, including parallelisation of the ITK modules used for image registration [106].

The work in this chapter has shown that the technique can correct for longer-term motion components with EPI at 7T by incorporating in-plane GRAPPA to minimise spatial distortion. A correction rate that is substantially shorter than the TR, which is the update interval for standard volume-to-volume motion correction, was achieved.

## 3.7 Conclusion

This chapter has introduced an implementation of the multislice-to-volume prospective motion correction technique for 7T EPI with the incorporation of GRAPPA for acceleration and minimisation of spatial distortion effects at this field strength. Preceding the main study, the size of the multislice subset used for motion correction was evaluated, with the use of three slices yielding an accuracy close to volume-to-volume registration. The multislice-to-volume technique also displayed sensitivity to sub-TR intra-volume motion. The main study results demonstrated that the motion correction technique is able to perform sub-TR motion correction and detection (up to 5% of TR) for longer-term motion components in long standard fMRI protocols at 7T, and subsequently reduce deleterious motion effects. The technique was also shown to work consistently across subjects with different propensities to in-scan motion. Applying the prospective motion correction technique also yielded in an observed improvement in temporal signal-to-noise ratio.

# Chapter 4

## Prospective motion correction using MS-PACE for 7T task-based functional MRI (fMRI)

### 4.1 Introduction

This chapter presents an implementation of the MS-PACE real-time motion correction technique for 7T task-based functional MRI (fMRI). To capture neuronal changes which are small, such as the associated blood oxygen level dependant (BOLD) signal [55], lengthy, multivolume acquisitions are often required to detect the signal through multiple observations. This makes fMRI protocols often prone to voluntary (e.g. from subject adjusting their position within the scanner or coil), involuntary (e.g. from gradual movement towards the padding cushion inside the coil [106]) and stimulus-correlated motion [116]. The motion risk is further elevated when the subject has to perform a task during the protocol, even if the task is relatively simple, such as finger tapping or button pressing. Motion correction is thus crucial and needed to correct for any artefacts in the acquired time series in order to preserve the quality of the data for subsequent functional analysis.

Most previous work with prospective motion correction uses volume-to-volume registration with relatively slow update rates. The MS-PACE method substantially reduces the update time and increases sensitivity to shorter-term motion components.

In this chapter, the MS-PACE integrated in-house EPI sequence developed in 3.4.3 was optimised and extended for use in task-based fMRI. The chapter sought to validate the effect of motion correction with MS-PACE in 7T fMRI acquisitions involving a finger tapping task.

## 4.2 Methods

(Published in [117][118])

The subjects were scanned on a MAGNETOM Terra 7T scanner (Siemens Healthineers, Erlangen, Bavaria, Germany) with a single-transmit, 32-channel receive head coil (Nova Medical, Wilmington, MA, USA) on 10 healthy subjects (age  $31 \pm 9$ ), of which 1 is left-handed and 9 are right-handed. The study received ethical approval from the local NHS Clinical Research Imaging Facility (CRIF) Approval Group [105]. The study was run with the aid of PsychoPy neuroscience software package [119], which transmitted the task commands to a screen behind the subject. Figure 4.1 outlines the block design used in this study. A single cross was set at the centre of the screen during non-task segments, while the word "tap" appeared on the screen during tapping segments. Apart from the first rest block, which included calibration scans, each rest/task block lasted 40 seconds, which is equal to 10 volumes. The paradigm involved tapping of the index finger on the hand specified before the start of a scan.



Figure 4.1: The block design used in the study. The finger tapping task blocks were interleaved with the rest blocks. Apart from the first rest block, which included calibration scans, each rest/task block lasted 40 seconds, which is equal to 10 volumes.

The scan protocol consisted of an initial  $T_1$ -weighted magnetization-prepared two rapid acquisition gradient echo (MP2RAGE) [120] whole-brain structural scan, which was acquired with the following parameters: sagittal orientation, isotropic voxel resolution  $0.8 \times 0.8 \times 0.8 \text{ mm}^3$ , matrix size  $320 \times 320$ , 208 slices, TR 5000ms, TE 1.94ms, TI (inversion times) = 700 and 2700 ms, echo spacing = 5.3ms, flip angles =  $4^\circ$  and  $5^\circ$ , in-plane GRAPPA acceleration = 3.

This was followed by six functional scans acquired with the in-house EPI sequence (as in Table 4.1). The functional scans were split into three groups: 2 resting scans, 2 scans with left-hand tapping and 2 scans with right-hand tapping. For each group, prospective motion correction was applied to one scan. The order of the motion corrected scans (off or on) was blinded to the subject to prevent biases. The subject was also not told pre-session that the study was looking at motion effects. Side padding cushions were provided to all subjects, but two subjects voluntarily elected to not use them. The scan parameters for the functional EPI scans were otherwise identical: gradient echo readout, transverse orientation, isotropic voxel resolution  $2.0 \times 2.0 \times 2.0 \text{ mm}^3$ , matrix size  $96 \times 96$ , GRAPPA acceleration factor of 3 with 32 calibration lines, 60 slices, 110 volumes, echo spacing 580ms, TR 4000ms, TE 18ms and total scan time 7m32s.

The threshold for motion correction was set for translation and rotation of 0.2mm and 0.2° respectively.

Task type	Prospective motion correction
None (resting)	Off
None (resting)	On
Left-hand tapping	Off
Left-hand tapping	On
Right-hand tapping	Off
Right-hand tapping	On

Table 4.1: The six EPI scans acquired from each subject and the task variation. The acquisition order was varied for each subject.

Using the method developed in Section 3.3.2, each multislice subset used for registration had 3 equidistant slices, i.e. for a 60-slice volume, the gap is 20 slices (indices of slice groups: 0-20-40, 1-21-41, 2-22-42, etc). The robustness of the motion correction was evaluated by retrospectively calculating the residual rigid body motion parameters (translation and rotation in x, y and z axes) using the multislice-to-volume method. Online and offline processing was done within the Image Calculation Environment (ICE) (Siemens Healthineers, Erlangen, Germany) using InsightToolkit (ITK) open-source image registration libraries.

For the resting (no task) data, temporal SNR (tSNR) maps were calculated for both datasets without and with prospective motion correction. These maps illustrate the temporal variance in noise and were calculated by comparing the mean signal of each voxel to its standard deviation over the time series. These were then compared for each subject by calculating the percentage difference in tSNR in every voxel between the two modes (prospective correction on and off)  $\delta tSNR_{(On-Off)}$ :

$$\delta tSNR_{(On-Off)} = \frac{tSNR_{On} - tSNR_{Off}}{\left(\frac{tSNR_{On} + tSNR_{Off}}{2}\right)} \times 100\% \quad (4.1)$$

To calculate the average  $\delta tSNR$  across all subjects, each  $\delta tSNR$  map was registered into standard Montreal Neurological Institute 152 (MNI152) space using FMRIB’s Linear Image Registration Tool or FLIRT (FSL, v.6.0, FMRIB, Oxford, England, UK) [115]. For a more accurate registration to the MNI152 space, each map was registered into its corresponding  $T_1$  structural volume before registration into MNI152 space.

The scan update rate was also analysed by evaluating the origin subset indices of the motion feedback received in each multislice subset, which were coded to be saved into the measurement data headers.

### 4.2.1 Functional analysis

For the tapping paradigm scans, a general linear model (GLM) analysis was performed using the BrainVoyager software package (v.22.4, Brain Innovation BV, Maastricht, The Netherlands) [121] to compare the parametric activation maps from the non-prospective-corrected and prospective-corrected data. The first step involved converting each DICOM dataset into a NIFTI file using the *dcm2nii* tool (MRICroGL, v.1.2, University of South Carolina, Columbia, SC, USA). Each EPI dataset was then preprocessed with slice scan-time correction (to specify each slice's timing), temporal high-pass filtering (to remove scanner and physiology-induced low frequency noise) and spatial smoothing with 4mm Gaussian kernel FWHM.

The datasets were also corrected with BrainVoyager's volumetric retrospective motion correction tool, which detects residual motion effects with volumetric image registration as opposed to the multislice-to-volume motion-correction technique used during the scan.

The processed EPI datasets were then coregistered to the  $T_1$ -weighted structural scan of the respective subject data, which was normalised to a 1-mm isovoxel dimension. Each MP2RAGE scan was skull-stripped and denoised using the CEREBRUM-7T tool [122]. To enable all-subject group analysis, each  $T_1$ -weighted structural scan was also normalised to the Talairach space, guided by the anterior commissure-posterior commissure (AC-PC) line of each brain [123]. This normalisation process was followed by the conversion of each of the fMRI slice-time-course files into volume-time-course (VTC) files using information from the coregistration step and the Talairach normalisation step.

These VTCs were used to perform a GLM analysis on each of the fMRI datasets. The VTCs were then fitted to the design matrix of predictors based on the block design. Using the tapping task as a predictor, the GLM was fitted to the time series data at each voxel to evaluate the BOLD response.

To statistically evaluate the performance of the prospective motion correction technique, A relevant region of interest (ROI), namely the primary motor cortex (Brodmann Area 4), was examined. For tapping scans on the left hand, the ROI was examined on the right hemisphere, and vice versa. The Talairach client [124] was used to pinpoint these regions within the atlas. Two measures were tested: 1. Multiple correlation coefficient or  $R$ -value (how well the GLM-analysed data fits to the model); 2.  $\beta$  weights (correlation strength of a predictor, which in this case is the BOLD activation during the task blocks) [125][126]. Paired two-tailed Student  $t$ -tests were then used. The non-prospectively corrected, but BrainVoyager-retrospectively corrected average of all subjects, was used as a benchmark/standard against the MS-PACE corrected average.

## 4.3 Results

Figure 4.2 compares the mean voxel displacement for the acquisitions without (green) and with (red) prospective motion correction across the three groups of scans, namely resting (no task), left-hand tapping and right-hand tapping scans. Using the rigid-body translational and rotational parameters across the three axes, the mean voxel displacement of each dataset is calculated by measuring the displacement of a voxel within the current imaging volume relative to the reference, before averaging the displacements across all the voxels in the volume. The figure shows reductions in mean voxel displacement across all groups of scans and all subjects, except in some subjects with low initial motion. Table 4.2 presents the statistical Student t-test results of the three groups' datasets.

Task type	Mean voxel displacement t-test
Resting	$t(9) = -3.996, p = 0.003$
Left-hand tapping	$t(9) = -3.476, p = 0.007$
Right-hand tapping	$t(9) = -3.511, p = 0.007$

Table 4.2: The results of Student t-test comparing the mean voxel displacement from scans with against without MS-PACE in the three functional group scans. The numbers in parentheses signify the degrees of freedom in each statistical calculation, which is the number of pairs evaluated subtracted by 1.

Figure 4.3 displays tSNR maps and percentage differences in tSNR from the resting scans with and without MS-PACE prospective motion correction in each subject ( $\delta$ tSNR) for a lower slice, a middle slice and an upper slice in the brain. The figure demonstrates increases in tSNR in most subjects in these slices when MS-PACE was applied.

### 4.3. Results

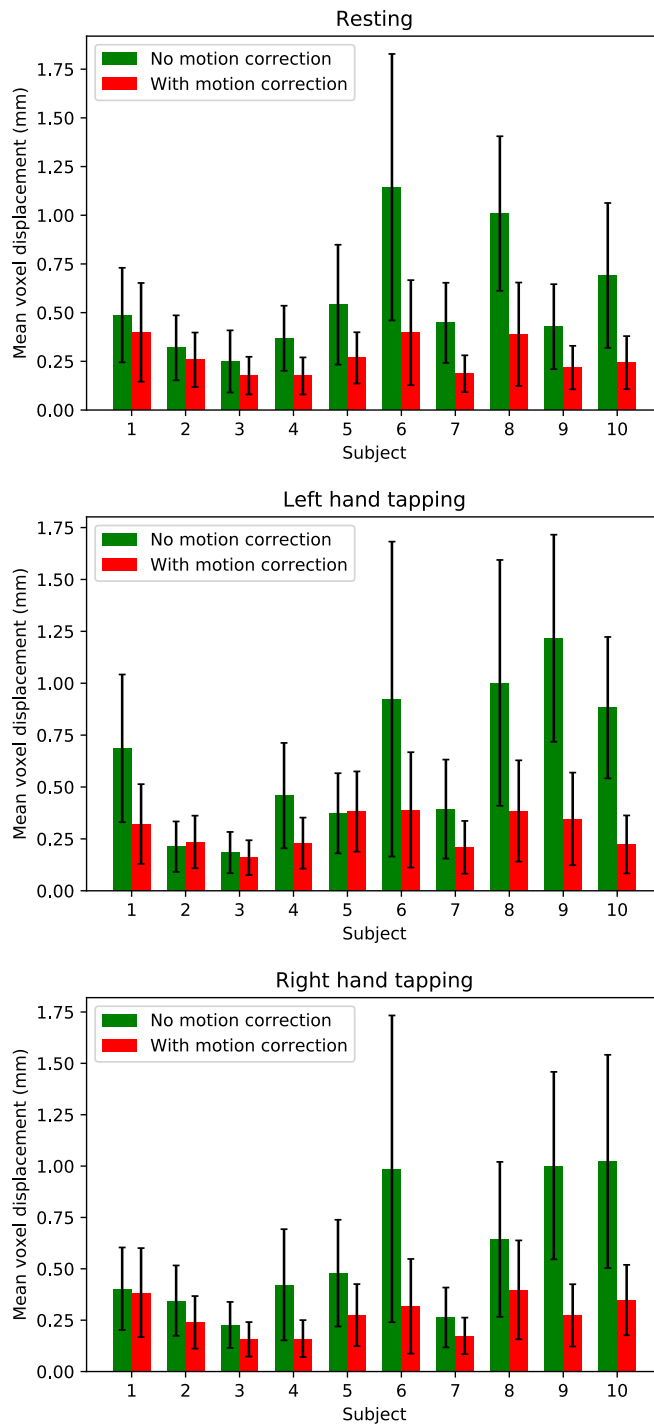


Figure 4.2: Mean voxel displacement comparison of the acquisitions without and with MS-PACE prospective motion correction for the three groups of functional scans: resting (top), left-hand tapping (middle) and right-hand tapping (bottom). The error bars represent the standard deviation in each dataset.

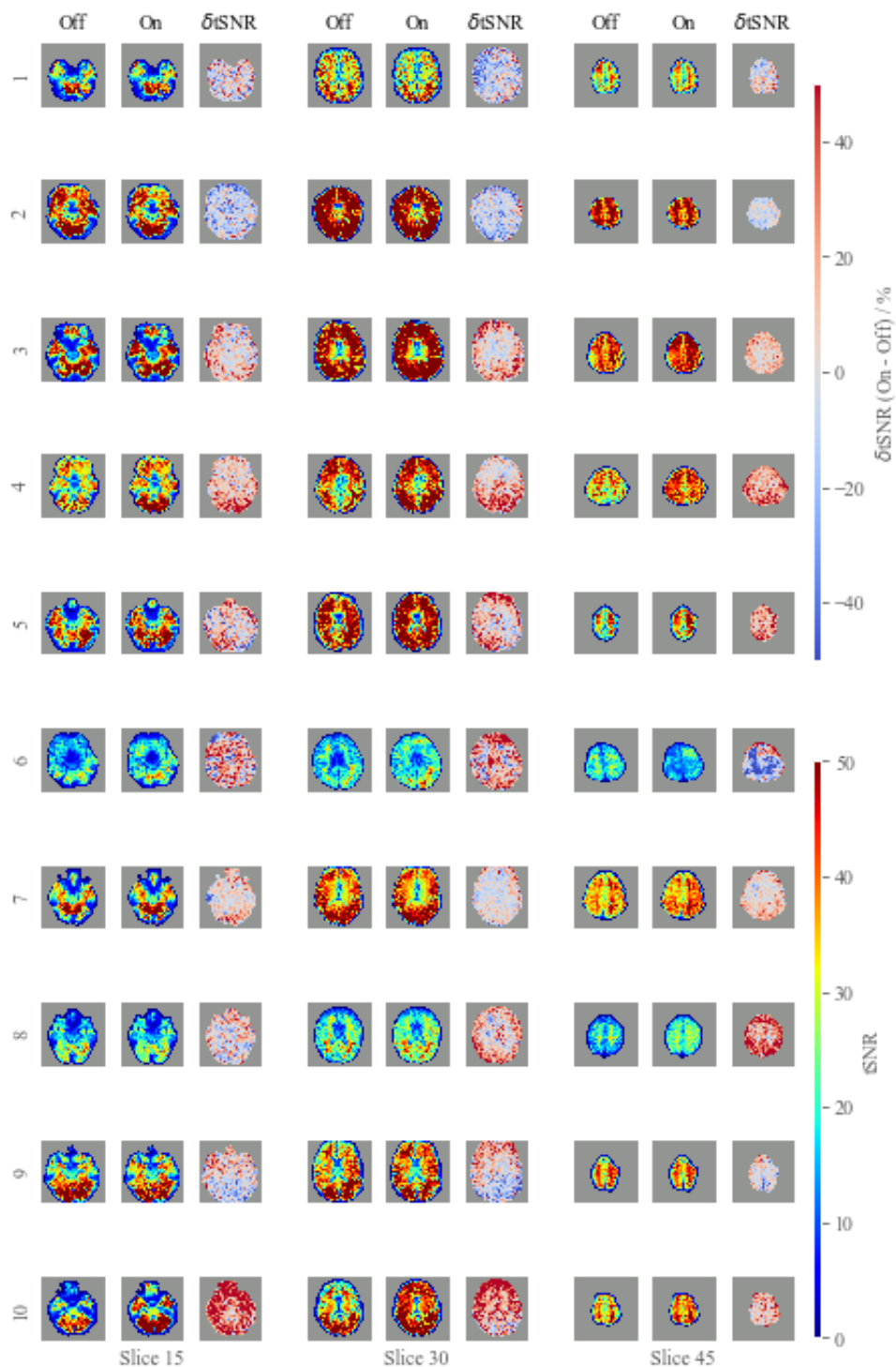


Figure 4.3: Temporal SNR (tSNR) maps and differences ( $\delta tSNR$ ) derived from the resting scans. The rows show data from individual subjects. In each row, the leftmost set of three images are from a lower slice, the middle set of three images are from a middle slice and the rightmost set of three images are from an upper slice. Within each set of three images, the first column is the tSNR map with MS-PACE turned off, the second column is the tSNR map with MS-PACE turned on, and the third column image is the  $\delta tSNR$ (On-Off).

### 4.3. Results

Figure 4.4 shows the average  $\delta\text{tSNR}(\text{On-Off})$  maps from the resting scans across all subjects normalised into standard MNI space. There is a mix of percentage increases and decreases in  $\delta\text{tSNR}$  across the maps.

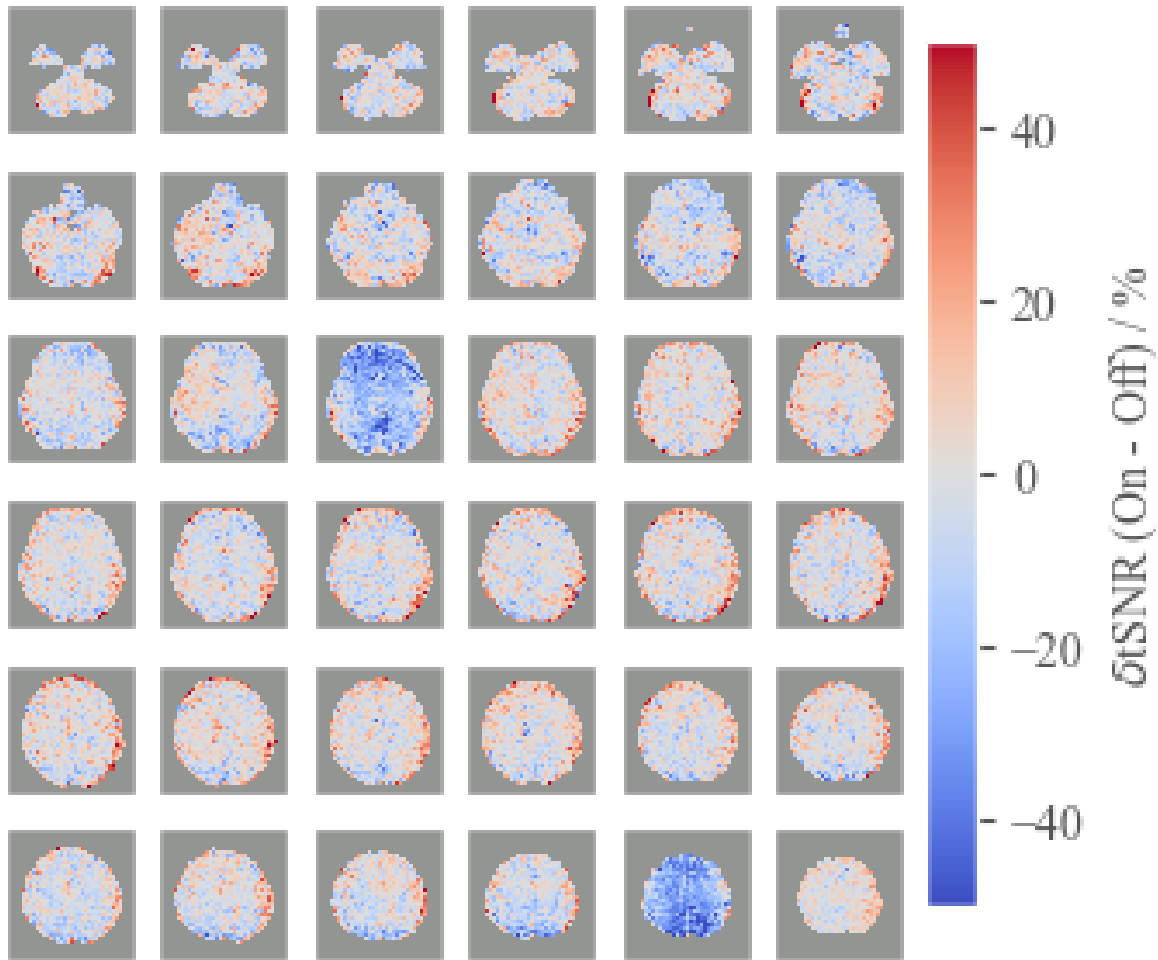


Figure 4.4: Average  $\delta\text{tSNR}(\text{On-Off})$  of the resting scans across all subjects. Each subject's  $\delta\text{tSNR}$  map was normalised into the standard MNI152 space before the average was calculated.

Figure 4.5 shows the trimmed average of the  $\delta tSNR(\text{On-Off})$  maps, which excludes the extreme 5% ends of the range and shows the average without the extreme outliers. Without the outliers, the maps show an average increase in  $\delta tSNR(\text{On-Off})$  except in two slices.

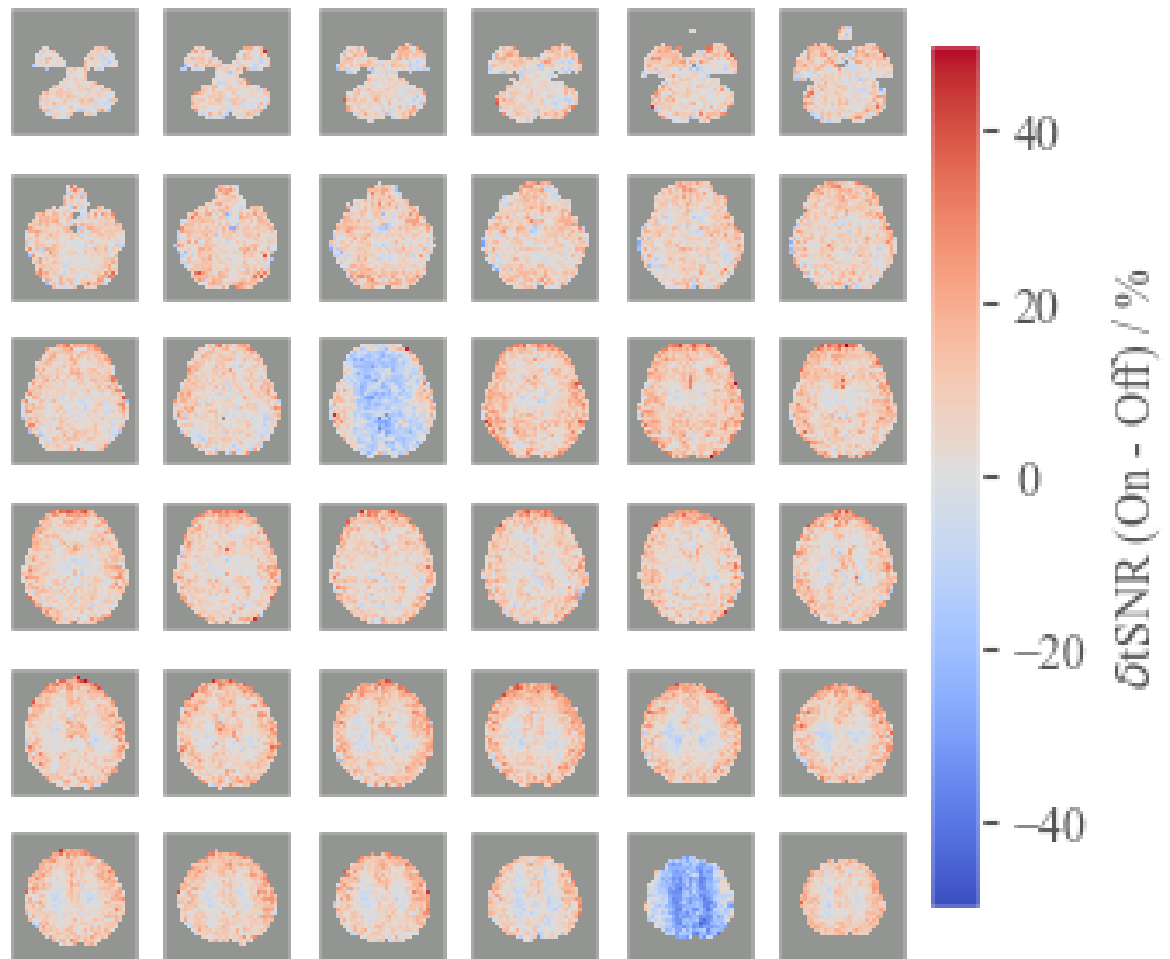


Figure 4.5: Trimmed average  $\delta tSNR(\text{On-Off})$  of the resting scans across all subjects (extreme 5% excluded). Each subject's  $\delta tSNR$  map was normalised into the standard MNI152 space before the average was calculated.

As Figures 4.4 and 4.5 displayed slices with consistently lower tSNR in the MS-PACE-corrected case, the corresponding subset of slices (indices 0, 20 and 40) were evaluated across all subjects in Figure 4.6 to determine whether the tSNR drops were consistent across all subjects. The drops were consistent, except in some slices with low tSNR from scans without MS-PACE.

### 4.3. Results

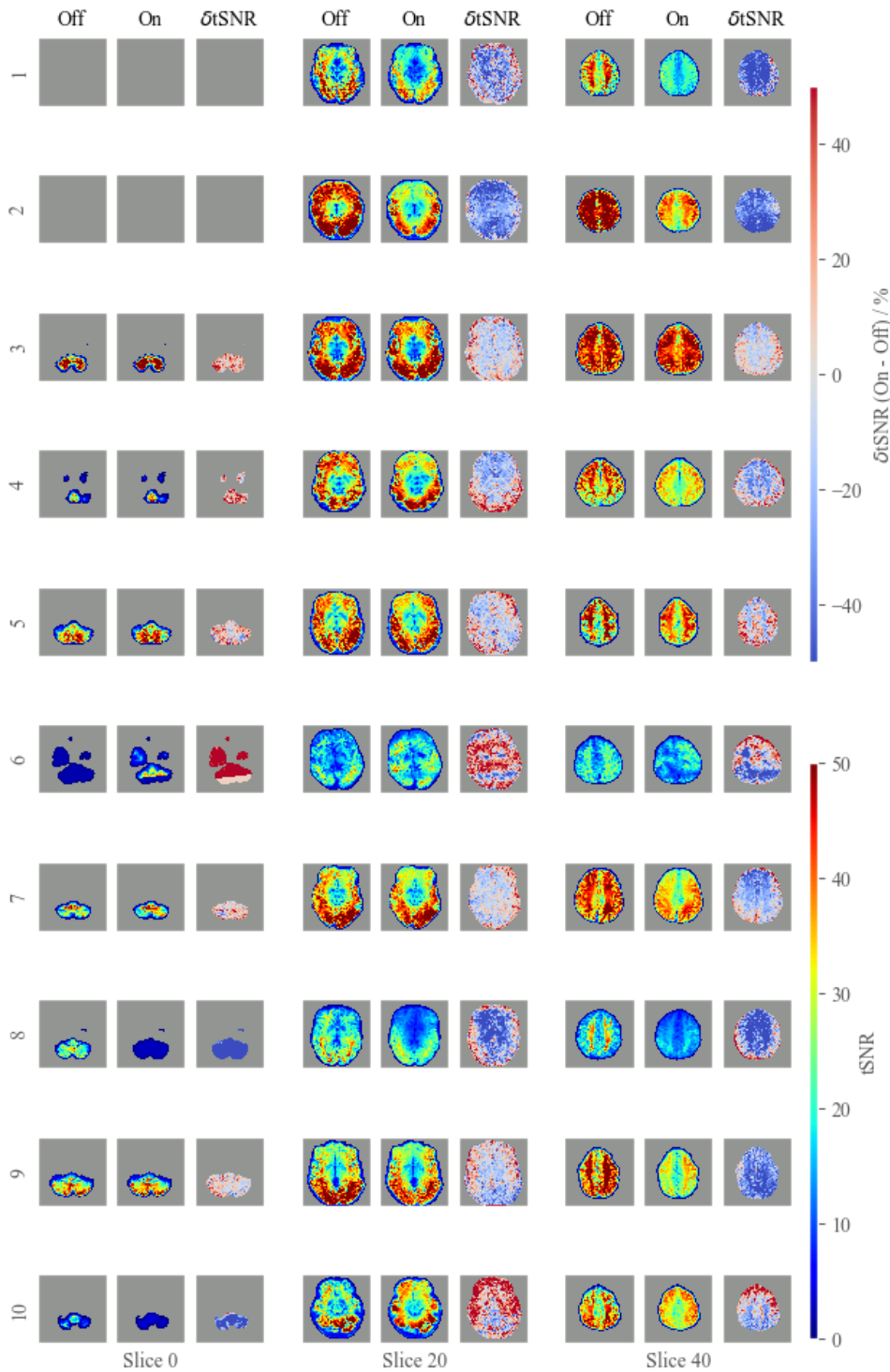


Figure 4.6: Temporal SNR (tSNR) maps and differences ( $\delta tSNR$ ) derived from the resting scans in all ten subjects when prospective motion correction was turned off or on. The maps were plotted for slices 0 (most inferior), 20 and 40 in subject-native EPI space. In each row, the leftmost set of three images are from a lower slice, the middle set of three images are from a middle slice and the rightmost set of three images are from an upper slice. Within each set of three images, the first column is the tSNR map with MS-PACE turned off, the second column is the tSNR map with MS-PACE turned on, and the third column image is the  $\delta tSNR(On-Off)$ .

Following the tSNR analysis of the affected slices, the feedback latency was also examined below in Figure 4.7. The figure shows that the affected slices used feedback from a three-slice subset in the previous volume that include superior slices, which in some subjects, had low spatial information.

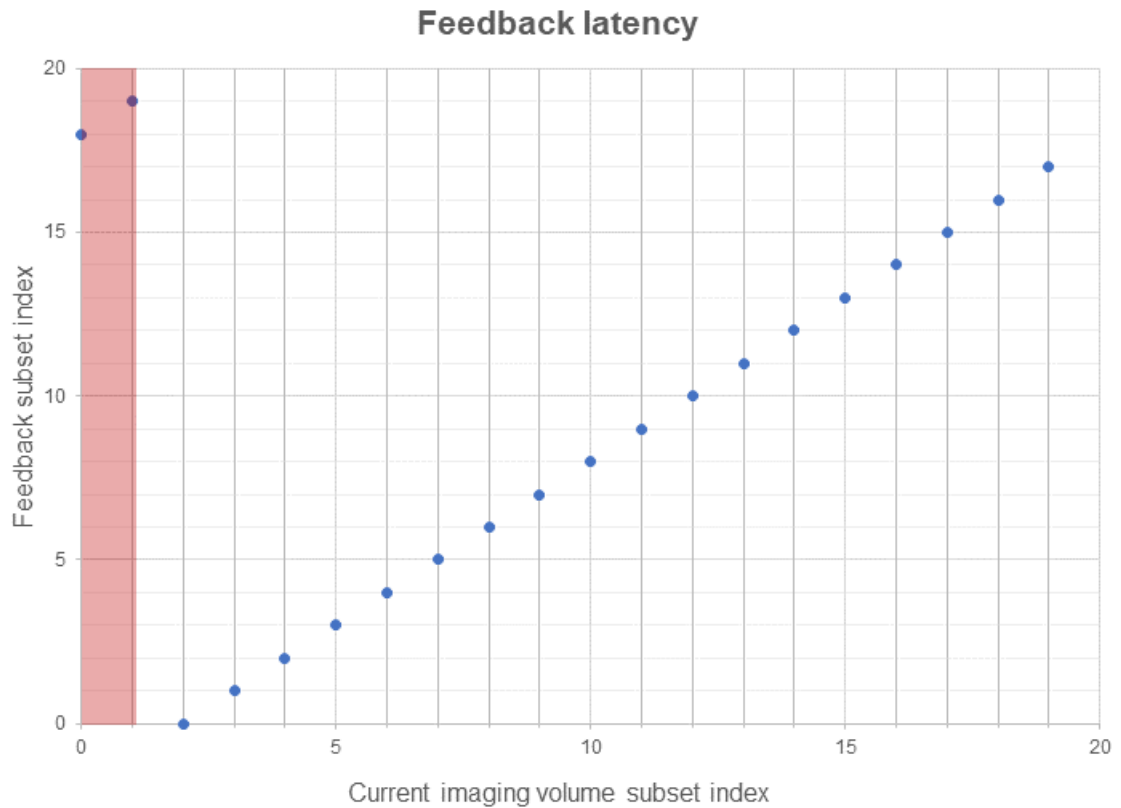


Figure 4.7: Analysis of scan update rate during prospective motion correction from one run, showing current imaging volume subset indices plotted against the origin subset of motion feedback received. The indices are of the first slice of each three-slice subset (e.g. 0 for 0-20-40, 1 for 1-21-41, etc.). The red-shaded area indicates feedback coming from the previous volume.

### 4.3. Results

Functional analyses were performed on the tapping paradigm scans. For both tapping groups, the data from subject 6 were excluded from the test due to the lack of detectable activation. For the right-hand tapping scans analysis, data from subject 1 were excluded from the test due to poor tapping performance during the non-prospectively corrected scan.

Figures 4.8a and 4.8b visualise the integrated GLM results for all subjects' left-hand tapping scans without and with prospective motion correction respectively. Figures 4.9a and 4.9b show the right-hand tapping equivalent.

To compare MS-PACE to the standard BrainVoyager retrospective correction, the latter was applied to the datasets acquired without prospective motion correction. Figure 4.8c demonstrates the integrated GLM results for all subjects' left-hand tapping scans without MS-PACE, but retrospectively-corrected in BrainVoyager. Figure 4.9c shows the right-hand tapping equivalent. Table 4.3 summarises the statistical Student t-tests of the GLM results comparing the averages in  $R$ -value and  $\beta$  weights in the primary motor cortex ROI between the MS-PACE and BrainVoyager retrospective correction (RC) methods.

Task	$R$ -value	$\beta$
Left-hand tapping	$t(8) = -1.009, p = 0.34$	$t(8) = 0.693, p = 0.51$
Right-hand tapping	$t(7) = 0.767, p = 0.47$	$t(7) = 1.898, p = 0.10$

Table 4.3: The results of Student t-test comparing the GLM results from tapping scans with prospective motion correction versus without (but retrospectively-corrected). The numbers in parentheses signify the degrees of freedom in each statistical calculation, which is the number of pairs evaluated subtracted by 1.

Lastly, the effect of combining BrainVoyager retrospective correction with MS-PACE prospective motion correction was evaluated. Figure 4.8d visualises the integrated GLM results for all subjects' left-hand tapping scans with MS-PACE prospective motion correction and BrainVoyager RC applied on both. Figure 4.9d shows the right-hand tapping equivalent.

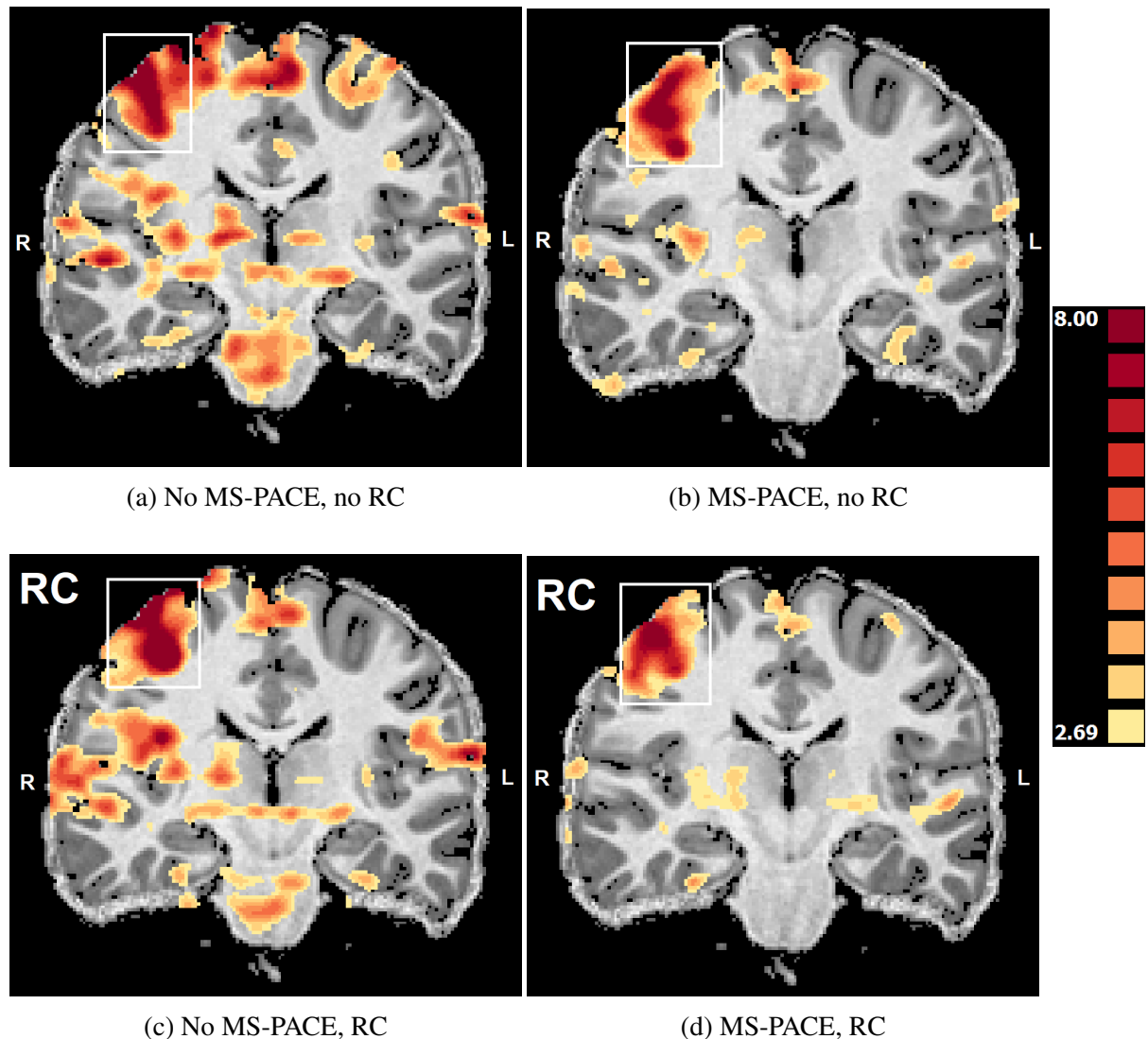


Figure 4.8: Integrated GLM results of all subjects' left-hand tapping paradigm scans without (a,c) and with (b,d) MS-PACE prospective motion correction.

BrainVoyager-retrospectively-corrected (RC) data are shown in the bottom row. The white boxes indicate the location of the hemisphere's primary motor cortex on the Talairach brain (coronal view). The bar scale is of the  $\beta$  weight, which indicates the activation during the task blocks.

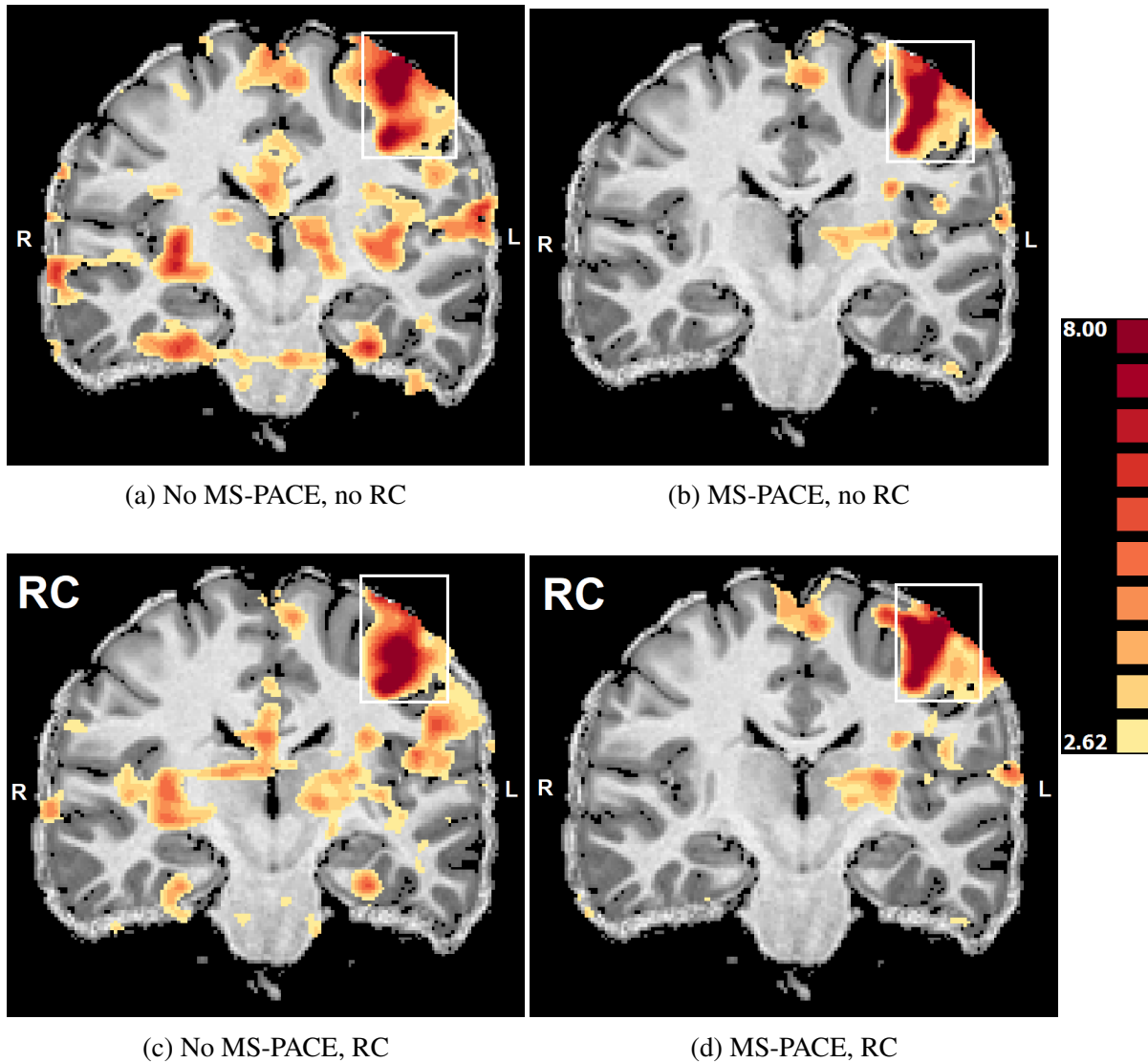


Figure 4.9: Integrated GLM results of all subjects' right-hand tapping paradigm scans without (a,c) and with (b,d) MS-PACE prospective motion correction.

BrainVoyager-retrospectively-corrected (RC) data are shown in the bottom row. The white boxes indicate the location of the hemisphere's primary motor cortex on the Talairach brain (coronal view). The bar scale is of the  $\beta$  weight, which indicates the activation during the task blocks.

To further compare the MS-PACE and BrainVoyager RC outcomes, the activation outside the primary motor cortex ROI in each individual technique map was quantified using the ImageJ software [127], i.e. between Figures 4.8b and 4.8c for left-hand tapping and between Figures 4.9b and 4.9c for right-hand tapping.

Task	RC	MS-PACE
Left-hand tapping	17.29%	5.85%
Right-hand tapping	14.75%	3.39%

Table 4.4: Comparison of outside-primary motor cortex ROI activation as a percentage of the full normalised Talairach brain slice in the integrated GLM map with an individual motion correction technique, i.e. BrainVoyager standard retrospective correction (RC) and MS-PACE.

## 4.4 Discussion

The MS-PACE prospective motion correction technique was implemented and evaluated on how it responded to the large variation of motion tendencies of the subjects in the cohort. The paradigm also added further risk of task-related motion during the protocol. Figure 4.2 compares the mean voxel displacements in each functional scan group (resting, left-hand tapping and right-hand tapping scans) from all subjects. The figure shows that the technique consistently corrected for motion across all subjects, from subjects who moved little to those who moved more significantly. For scans with a low level of movement, there was also a reduction in most cases, demonstrating that the method is performing well at multiple scales of motion. The prospective correction was found to be effective for both resting scans and scans acquired during the tapping paradigm, which are at risk from stimulus-correlated motion. It is important however to note that each acquisition is separate and thus the underlying motion patterns are variable. This explains the case of subject 2 and 5 during their left-hand tapping scans, where the non-prospectively-corrected data has marginally less displacement than the corresponding prospectively-corrected data. In both cases, the subjects moved less during the non-prospectively-corrected scans. Despite this, the marginally-worse prospectively-corrected scans still have residual displacement that is much smaller than the voxel size.

Shown in Table 4.2, statistical Student t-test evaluation of the mean voxel displacement in the three groups yields all negative values, signifying that the technique has reduced the mean in all three groups. The p-values are also much lower than the 0.05 threshold, which suggest that the findings are statistically significant.

#### 4.4. Discussion

---

Temporal SNR analysis of the resting scans also demonstrates positive effects in most subjects when prospective motion correction was applied. As observed in Figure 4.3, Percentage-wise increases in tSNR ( $\delta$ tSNR) in the prospective-corrected scans were observed to be particularly more significant in subjects that moved more, such as subject 6, 8, 9 and 10. However, the net  $\delta$ tSNR increases are not universal across all voxels, especially in regions with already high tSNR (as shown in subject 9).

The average  $\delta$ tSNR across all subjects (shown in Figure 4.4) however displays percentage decrease in most voxels when prospective motion correction was applied. As the voxelwise percentage difference has a small range (0-100% or 0-1), outlier positive or negative percentage differences can significantly contribute to the average. Using the trimmed mean statistical measure, which excludes 5% of each extreme, the outliers were excluded from this analysis. After the exclusion of outlier data, the average (shown in Figure 4.5) demonstrates an overall tSNR improvement with prospective motion correction on most slices. These findings demonstrate that while  $\delta$ tSNR generally improves using the technique, it does not always provide additional benefits when detected motion is already limited.

Observed in both Figures 4.4 and 4.5, several slices consistently have lower tSNR with prospective motion correction. These correspond to slices 20 and 40 in the native space. Comparing the  $\delta$ tSNR in the subset of slices 0, 20 and 40 (Figure 4.6), drops in tSNR in the motion corrected data can be seen to occur in a majority of the subjects in those slices. Due to the feedback latency (shown in Figure 4.7), these chronologically-acquired series of slices used feedback information from a subset in the previous volume with low amounts of information. Due to the large coverage of the brain (high number of slices), the feedback origin slices also included superior slices, which have more limited spatial information, and this could result in inaccurate registrations. As brain sizes vary, there were not always brain information in the superior part of the 60-slice volume, and when there was signal, these could disappear from the position due to motion. In the future, using a smaller volume that covers only the non-skull region of the brain may reduce these effects.

For the tapping paradigm acquisitions, an initial comparison of the group activation maps for the left-hand tapping (shown in Figures 4.8a and 4.8b) and right-hand tapping (shown in Figures 4.9a and 4.9b) was performed. In both task paradigms, primary motor cortex activation was reflected in the correct region and hemispheres in the group maps without and with prospective motion correction. However in the group maps of the former, higher levels of noise and activation outwith the primary motor cortex and supplementary motor area (located medially). The group maps of the latter have comparably less of this.

To examine how 7T MS-PACE performed against standard BrainVoyager retrospective mo-

tion correction, a procedure routinely performed in fMRI analysis [113]), paired two-tailed Student t-tests were performed on  $R$ -value and  $\beta$  weight measures to statistically compare the acquisitions with only BrainVoyager retrospective correction and with only MS-PACE. As shown in Table 4.3, the p-values in the t-test results, which evaluates whether the difference between the two averages being compared is statistically significant, are above 0.05 in all cases (both measures and both tapping tasks). A p-value of under 0.05 means the difference between the compared averages are significant. This implies that the prospective motion correction performed similarly to the retrospective motion correction of the non-prospectively corrected data, which is the standard in fMRI analysis.

Comparing group activation maps for the left-hand tapping (Figures 4.8c versus 4.8b) and right-hand tapping (Figures 4.9c versus 4.9b) demonstrates that primary motor cortex activation was detected in the scans corrected only in real time with MS-PACE at a similar level to the benchmark retrospectively-corrected data. This agrees with the aforementioned t-test results and demonstrates that the MS-PACE application during fMRI acquisitions produces volumes showing activation accurate to the paradigm or protocol. It is however worth noting that the retrospectively-corrected data has stronger activation profile in the region surrounding the primary motor cortex, suggesting that extra activation was recovered in this standard method. However, as in the preceding comparison, there is more false-positive and outside-ROI activation in the acquisitions without MS-PACE with standard thresholding. This is supported by the analysis in Table 4.4, which shows lower percentages of outside-ROI activation in the MS-PACE-only maps for both left-hand and right-hand tapping. A caveat is that some outside-ROI signal may be related to secondary functions activated during the task, for example somatosensation [128].

Finally, applying standard retrospective correction during postprocessing to the MS-PACE-corrected data yields maps with clear activation profile in the ROI and lower amount of false-positive signal, as shown in Figures 4.8d) (left-hand tapping) and 4.9d) (right-hand tapping). This demonstrates that the application of MS-PACE during the fMRI acquisitions can produce improved datasets for fMRI postprocessing analysis.

fMRI scanning protocols at 7T often target a higher spatial resolution than that used in this study, for example when exploring the differential neuronal responses in the cortical layers [129]. Future work with the MS-PACE motion correction method will include an evaluation of its performance in these ultra-high-resolution applications.

### **4.5 Conclusion**

This chapter validated an application of the MS-PACE multislice-to-volume prospective motion correction technique for task-based fMRI at 7T. An analysis of mean voxel displacements shows that the technique was able to consistently minimise motion effects in a cohort of ten subjects and in a statistically-significant manner. Voxelwise temporal SNR has also been observed to generally improve with MS-PACE, albeit this was not completely universal and there are overall percentage decreases in some subjects. Functional analysis of the tapping paradigm acquisitions demonstrated that the technique performs well in comparison to standard software retrospective motion correction. Activation signal in the primary motor cortex ROI was preserved and false-positive activations were reduced even without high thresholding. The use of both prospective and retrospective methods together has also been shown to yield maps with clear activation profiles within the ROI.

# Chapter 5

## MS-PACE prospective motion correction using parallel transmit imaging (pTx) at 7T

### 5.1 Introduction

This chapter presents a novel implementation of the MS-PACE real-time motion correction technique at 7T with the integration of parallel transmit (pTx) imaging. Ultra-high field MRI, which includes field strengths equal or larger than 7T, has an inherent problem of transmit field ( $B_1^+$ ) inhomogeneity. The inclusion of pTx sought to tackle this issue. In this chapter, a slice-by-slice  $B_1^+$  field shimming scheme using pTx was integrated into the MS-PACE technique and compared against the circularly-polarised (CP) version of the technique, which is equivalent to conventional single transmission (sTx). The objectives of this chapter were to develop a method in which pTx pulses are updated in real time as part of a prospective motion correction scheme, and to confirm that both pTx and motion correction contribute to improved image quality when applied together as part of an integrated acquisition scheme.

#### 5.1.1 Online pTx pulse design and slice-by-slice $B_1^+$ shimming

Parallel transmission uses a dedicated RF coil with independent transmit channels that generate individual RF fields. These  $B_1^+$  fields can be tailored for a homogenous, combined excitation that is simultaneously subject to SAR constraints. As the maps are subject-specific and thus also session-specific, the pTx system needs to consider  $B_1^+$  maps and static field  $B_0$  maps during each session. It is possible to eliminate the need to measure field maps every session by using a more

generalised pulse such as in the Universal Pulse (UP) approach [130]. Instead of using session-acquired field maps, universal pulses use previously-acquired maps from a representative subject group. While this provides convenience and overall scan time reduction, the UP method does not perform as well as tailored pulse design methods.

While previously complicated and requiring extensive offline work during scan sessions, tailored pTx workflows have been optimised in the recent years to be able to run online on 7T scanners such as the Siemens MAGNETOM Terra. The work described in this chapter integrated a subject-specific pTx workflow [131][132]. Instead of a full-head, volumetric  $B_1^+$  shimming, the workflow utilised slice-by-slice  $B_1^+$  shimming, which was demonstrated to provide superior transmit homogeneity at 7T compared to the former option [133].

## 5.2 Methods

*(Published in [134])*

A right-handed finger-tapping task was used to characterise the performance of fMRI data acquisition using combined prospective motion correction and pTx. 6 healthy subjects (age  $45 \pm 15$ ) were scanned on a MAGNETOM Terra 7T scanner (Siemens Healthineers, Erlangen, Bavaria, Germany) with an 8-channel transmit, 64-channel receive head coil (MR CoilTech Ltd, Glasgow, Scotland, UK) (shown in Figure 5.1) [135][136], of which 1 is left-handed and 5 are right-handed. The study received ethical approval from the local NHS Clinical Research Imaging Facility (CRIF) Approval Group [105]. The study was run with the aid of the PsychoPy neuroscience software package [119], which transmits the task commands to a screen behind the subject. The screen was viewed through a rear-facing mirror attached to the head coil (see Figure 5.1). Figure 5.2 outlines the block design used in this study, which is identical to the one used in the study in Section 4.2. A single cross was set at the centre of the screen during non-task segments, while the word "tap" appeared on the screen during tapping segments. Apart from the first rest block, which included calibration scans, each rest/task block lasted 40 seconds, which is equal to 10 volumes.

Following localisation and  $B_0$  shimming,  $B_0$  and  $B_1^+$  field mapping [137] were performed at the slice positions used by the EPI protocol, and the results were used in MATLAB (MathWorks, Natick, MA, USA) offline to generate pTx slice-specific  $B_1^+$  shim weights (see below).

Prior to the validation experiments, the MS-PACE-enabled 7T EPI sequence (see Section 3.3) was adapted for reading in and applying excitation pulses with the calculated slice-by-slice shim values.

This was followed by a  $T_1$ -weighted fast low angle shot (FLASH) whole-brain structural



Figure 5.1: The 8-channel transmit, 64-channel receive head coil used in the study. The design features an open face to help reduce claustrophobic reactions. A visor mirror was placed to reflect the screen correctly towards the subject. Reproduced with permission from Dr G. Shajan.



Figure 5.2: The block design used in the study, which is similar to in Section 4.2. The finger tapping task blocks were interleaved with the rest blocks. Apart from the first rest block, which included calibration scans, each rest/task block lasted 40 seconds, which is equal to 10 volumes.

scan, which was acquired with the following parameters: sagittal orientation, isotropic voxel resolution  $0.8 \times 0.8 \times 0.8 \text{ mm}^3$ , matrix size  $320 \times 320$ , 208 slices, TR 35ms, TE 2.00ms, echo spacing 5.3ms, flip angle  $50^\circ$ , in-plane GRAPPA acceleration factor 2.

While the  $T_1$ -weighted FLASH structural scan was being acquired, the pulse design data were collected from the scanner, reconstructed offline on MATLAB (MathWorks, Natick, MA, USA) and used to calculate slice-by-slice  $B_1^+$  shims. This slice-wise shimming was done using a specialised magnitude least-squares [138] optimisation technique, originally formulated by Williams et al. [131] (see Equation 5.1 below):  $N_s$  represents the number of slices;  $\mathbf{A}_{\text{shim}}$  the small tip-angle excitation matrix calculated with the  $B_1^+$  maps [139];  $\mathbf{b}_{\text{shim},s}$  optimised  $B_1^+$  shims;  $\alpha$  the flip angle;  $\mathbf{w}$  the region of interest mask used for evaluating excitation performance;  $\mathbf{Q}$  the Q-matrices used for SAR prediction [140];  $N_v$ , the number of Q matrices used for calculating local SAR.

$$\begin{aligned}
& \text{for } s = 1 : N_s \\
& \quad \hat{\mathbf{b}}_{\text{shim},s} = \arg \min_{\mathbf{b}_{\text{shim},s}} \| |\mathbf{A}_{\text{shim},s} \mathbf{b}_{\text{shim},s}| - \alpha \|_{\mathbf{W}}^2 \\
& \quad \text{subject to} \\
& \quad \mathbf{b}_{\text{shim},s}^H \mathbf{Q}_v \mathbf{b}_{\text{shim},s} \leq \text{SAR}_{\text{max},\text{local}} \quad \forall v = 1 : N_v \\
& \quad \text{stdev}(|\mathbf{A}_{\text{shim},s} \mathbf{b}_{\text{shim},s}|) \leq 0.1 \alpha \\
& \text{end}
\end{aligned} \tag{5.1}$$

This optimisation involved imposing a constraint on the standard deviation of 0.1 times of the flip angle and also local SAR. This process produced relative magnitude and phase for each of the 8Tx channels, which could be applied universally to all excitation pulses throughout the sequence. This optimisation step was also performed individually on each of the 51 slices. These optimised shim data were then loaded back into the scanner to be executed in the fMRI acquisitions.

After the  $T_1$ -weighted structural scan was completed, 4 functional scans were acquired with the in-house EPI sequence (as in Table 5.1). The EPI sequence was adapted to include slice-by-slice  $B_1^+$  shimming capabilities. 4 EPI scans were acquired: 2 in CP (sTx-equivalent) mode and 2 in pTx shim mode. The order of the acquisition was blinded to the subject to prevent biases. Side padding cushions were also provided to all subjects for comfort. The scan parameters for the functional EPI scans were otherwise identical: gradient echo readout, isotropic voxel size  $2.0 \times 2.0 \times 2.0 \text{ mm}^3$ , resolution  $96 \times 96$ , in-plane GRAPPA acceleration factor of 3 with 32 calibration lines, 51 slices, 110 volumes, echo spacing 580ms, TR 4000ms, TE 18ms, target flip angle  $90^\circ$  and total scan time 7m32s. The threshold for motion correction was set for translation and rotation of 0.2mm and  $0.2^\circ$  respectively.

Transmit mode	Motion correction
CP	Off
CP	On
pTx	Off
pTx	On

Table 5.1: The parameter variation of the four functional scans acquired from each subject.

Each multislice subset used for registration had 3 equidistant slices, i.e. for a 51-slice volume, the gap is 17 slices (indices of slice groups: 0-17-34, 1-18-35, 2-19-36, etc). The robustness of the motion correction was evaluated by retrospectively calculating the residual rigid body

motion parameters (translation and rotation in x, y and z axes) using the multislice-to-volume method. Online and offline processing was done within the Image Calculation Environment (ICE) (Siemens Healthineers, Erlangen, Germany) using InsightToolkit (ITK) open-source image registration libraries.

Temporal SNR (tSNR) comparison maps were also calculated. These maps illustrate the temporal variance in noise and were calculated by comparing the mean signal of each voxel to its standard deviation over the time series. These were then compared for each subject by calculating the percentage difference in tSNR in every voxel between the two modes  $\delta tSNR_{(Mode2-Mode1)}$ , e.g. between CP and pTx excitation modes, or between motion correction off and on:

$$\delta tSNR_{(Mode2-Mode1)} = \frac{tSNR_{Mode2} - tSNR_{Mode1}}{\left(\frac{tSNR_{Mode2} + tSNR_{Mode1}}{2}\right)} \times 100\% \quad (5.2)$$

To calculate the average  $\delta tSNR$  across all subjects, each  $\delta tSNR$  map was registered into standard Montreal Neurological Institute 152 (MNI152) space using FMRIB's Linear Image Registration Tool or FLIRT (FSL, v.6.0, FMRIB, Oxford, England, UK) [115]. For a more accurate registration to the MNI152 space, each map was registered into its corresponding  $T_1$  structural volume before registration into MNI152 space.

### 5.2.1 Functional analysis

The preprocessing steps follows the ones used Section 4.2.1. A general linear model (GLM) analysis was then performed using the BrainVoyager software package (v.22.4, Brain Innovation BV, Maastricht, The Netherlands) to compare the parametric activation maps from the non-prospective-corrected and prospective-corrected data. The first step involved converting each DICOM dataset into a NIFTI file using the *dcm2nii* tool (MRICroGL, v.1.2, University of South Carolina, Columbia, SC, USA). Each EPI dataset was then preprocessed with slice scan-time correction (to specify each slice's timing), temporal high-pass filtering (to remove scanner and physiology-induced low frequency noise) and spatial smoothing with 4mm Gaussian kernel FWHM.

The processed EPI datasets were then coregistered to the 1mm-isovoxel-normalised  $T_1$ -weighted structural scan of the respective subject data. Every  $T_1$ -weighted FLASH scan was skull-stripped using FSL's Brain Extraction Tool (BET) [141]. To enable all-subject group analysis, each  $T_1$ -weighted structural scan was also normalised to the Talairach space, guided by the anterior commissure-posterior commissure (AC-PC) line of each brain [123]. This normalisation process was followed by the conversion of each of the fMRI slice time course files into

### 5.3. Results

volume time course (VTC) files using information from the coregistration step and the Talairach normalisation step.

These VTCs were used to perform a GLM analysis on each of the fMRI datasets. The VTCs were then fitted to the design matrix of predictors based on the block design. Using the tapping task as a predictor, the GLM was fitted to the time series data at each voxel to evaluate the BOLD response. A relevant region of interest (ROI), namely the primary motor cortex (Brodmann Area 4), was examined. As the paradigm involves right-hand tapping, the ROI was examined on the left hemisphere. The Talairach client [124] was used to pinpoint these regions within the atlas.

## 5.3 Results

### 5.3.1 Application of MS-PACE to data acquisition using pTx

Figure 5.3 shows the transmit channel-wise  $B_1^+$  field magnitude maps from the centre slice in one subject, which were acquired for the slice-by-slice  $B_1^+$  shim calculation step. Figure 5.4 shows the corresponding transmit channel-wise phase maps. Figure 5.5 visualises the channel-combined  $B_1^+$  maps for three slice positions: 16, 26 (centre) and 36 in the subject.

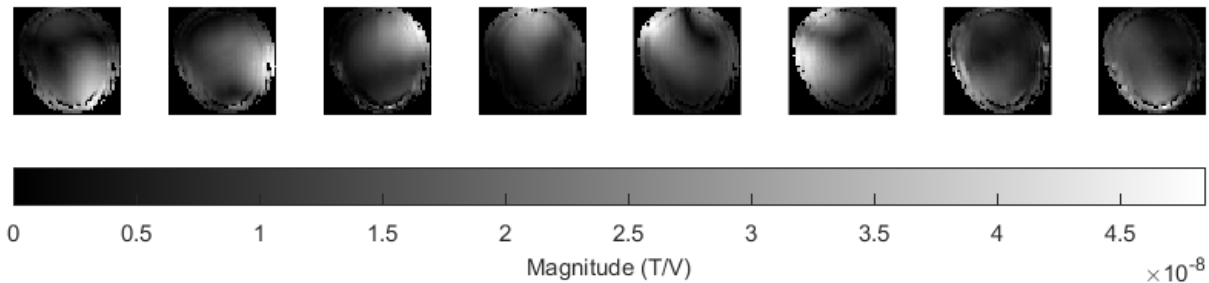


Figure 5.3: Transmit channel-wise  $B_1^+$  field magnitude maps from the centre slice in one subject.

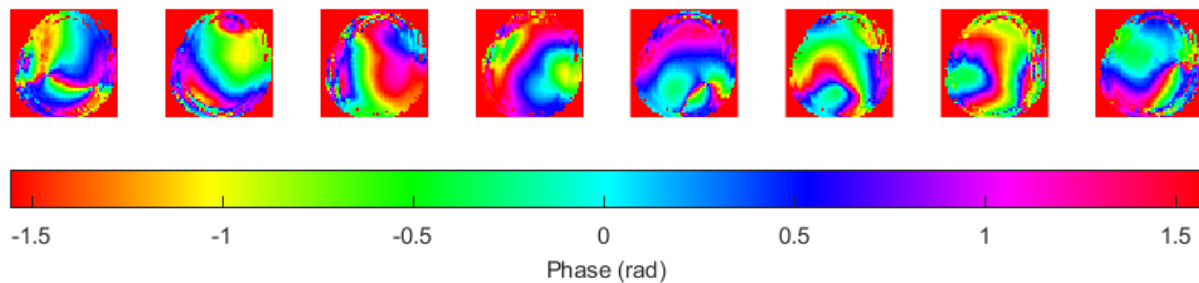


Figure 5.4: Transmit channel-wise  $B_1^+$  field phase maps from the centre slice in one subject.

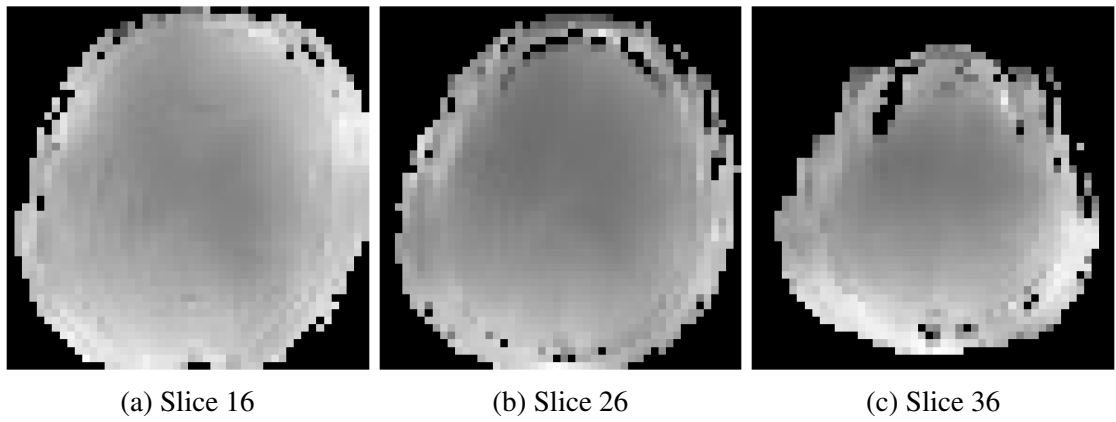


Figure 5.5: Combined  $B_1^+$  field maps for slices 16, 26 (centre) and 36 in one subject.

### 5.3. Results

Figure 5.6 compares the mean voxel displacement for the CP acquisitions without (green) and with (red) prospective motion correction. Figure 5.7 compares the same for the pTx acquisitions. Using the rigid-body translational and rotational parameters for the three axes, the mean voxel displacement of each dataset is calculated by measuring the displacement of a voxel within the current imaging volume relative to the reference, before averaging the displacements across all the voxels in the volume. The figure shows lower mean voxel displacement in scans with correction in both modes across all subjects, except in the CP scan of subject 6.

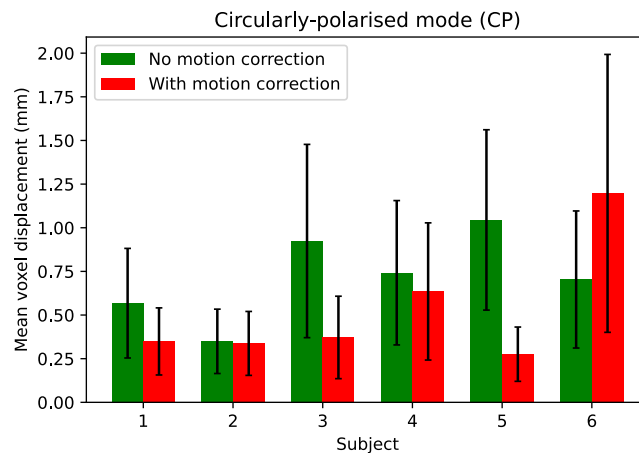


Figure 5.6: Mean voxel displacement comparison of the acquisitions without and with MS-PACE prospective motion correction for the CP acquisitions. The error bars represent the standard deviation in each dataset.

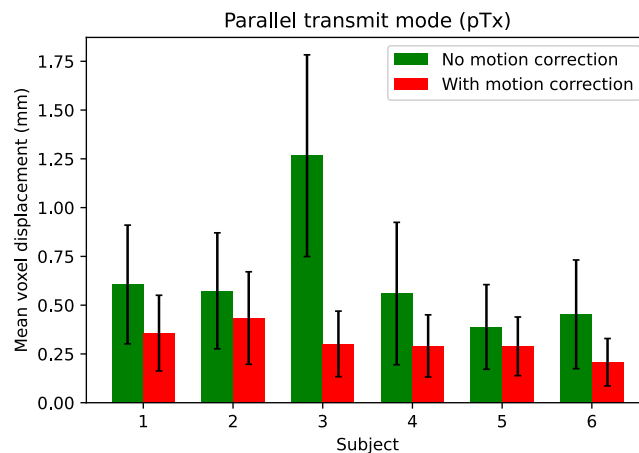


Figure 5.7: Mean voxel displacement comparison of the acquisitions without and with MS-PACE prospective motion correction for the pTx acquisitions. The error bars represent the standard deviation in each dataset.

Table 5.2 presents the statistical Student t-test results of both transmit mode scans.

Transmit mode	Mean voxel displacement t-test
CP	$t(5) = -1.079, p = 0.33$
pTx	$t(5) = -2.513, p = 0.05$

Table 5.2: Student t-test comparing the mean voxel displacement from scans with against without MS-PACE in both transmit modes. The numbers in parentheses signify the degrees of freedom in each statistical calculation, which is the number of pairs evaluated subtracted by 1.

Figure 5.8 displays tSNR maps and percentage differences in tSNR from the resting scans with and without prospective motion correction in each subject ( $\delta$ tSNR). The figure shows higher increases in tSNR where the tSNR in non-corrected scans is lower (i.e. subject 3 and 6), but lower increases and also decreases when the tSNR in non-corrected scans is already high (i.e. subject 4's occipital region and subject 5).

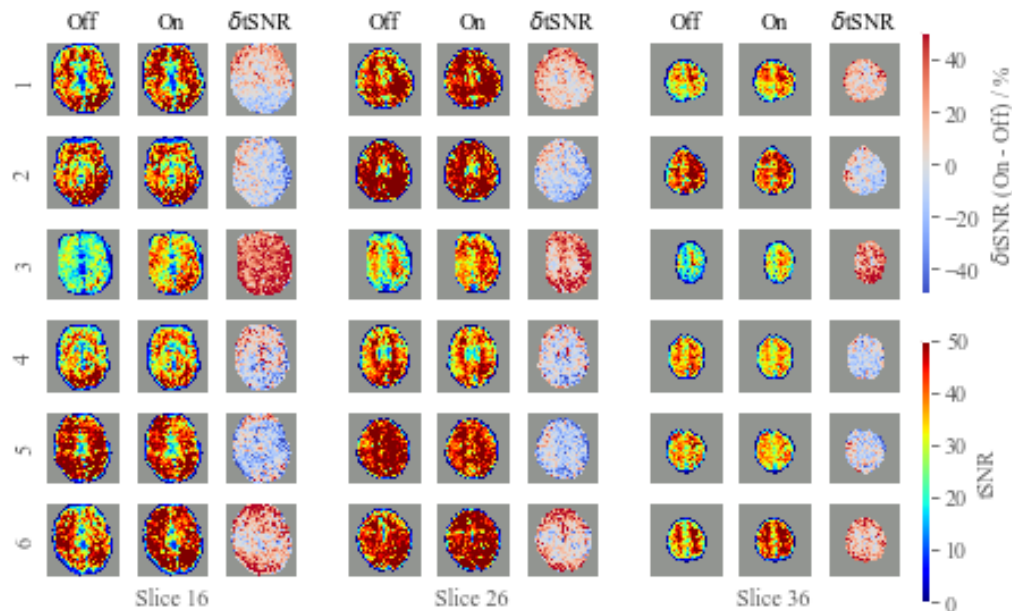


Figure 5.8: Temporal SNR (tSNR) maps and differences ( $\delta$ tSNR) derived from the pTx scans in all six subjects when prospective motion correction was turned off or on. The maps were plotted for slices 16, 26 (centre) and 36 in subject-native EPI space. In each row, the leftmost set of three images are from slice 16, the middle set of three images are from slice 26 and the rightmost set of three images are from slice 36. Within each set of three images, the first column is the tSNR map with MS-PACE turned off, the second column is the tSNR map with MS-PACE turned on, and the third column image is the  $\delta$ tSNR(pTx-CP).

### 5.3. Results

Figure 5.9 shows the average  $\delta tSNR$  maps from the pTx scans across all subjects, normalised into standard MNI space with positive values indicating an increased SNR when MS-PACE was used.

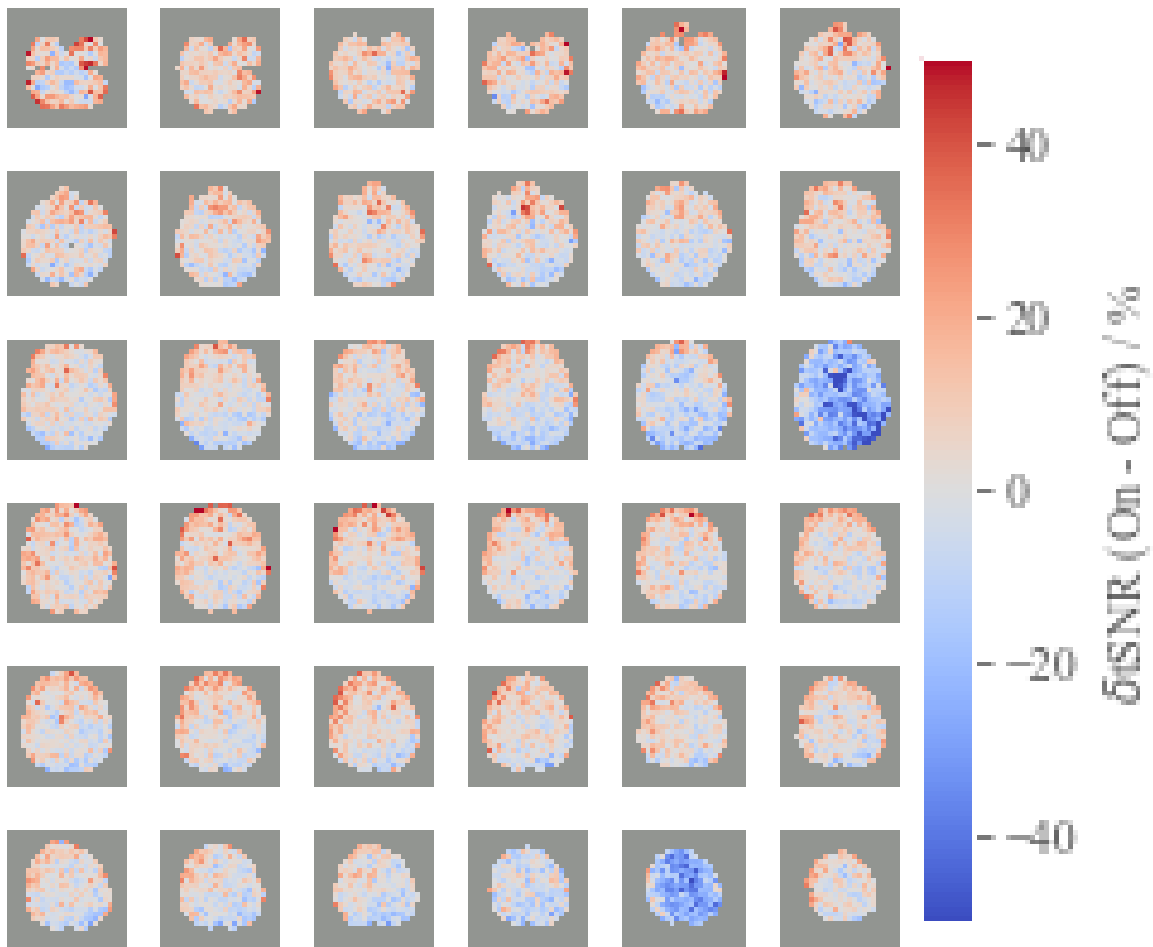


Figure 5.9: Mean  $\delta tSNR$ (On-Off) of the pTx scans across all subjects. Each subject's  $\delta tSNR$  map was normalised into the standard MNI152 space before the average was calculated.

Figure 5.10 shows the trimmed average, which excludes the extreme ends of the range.

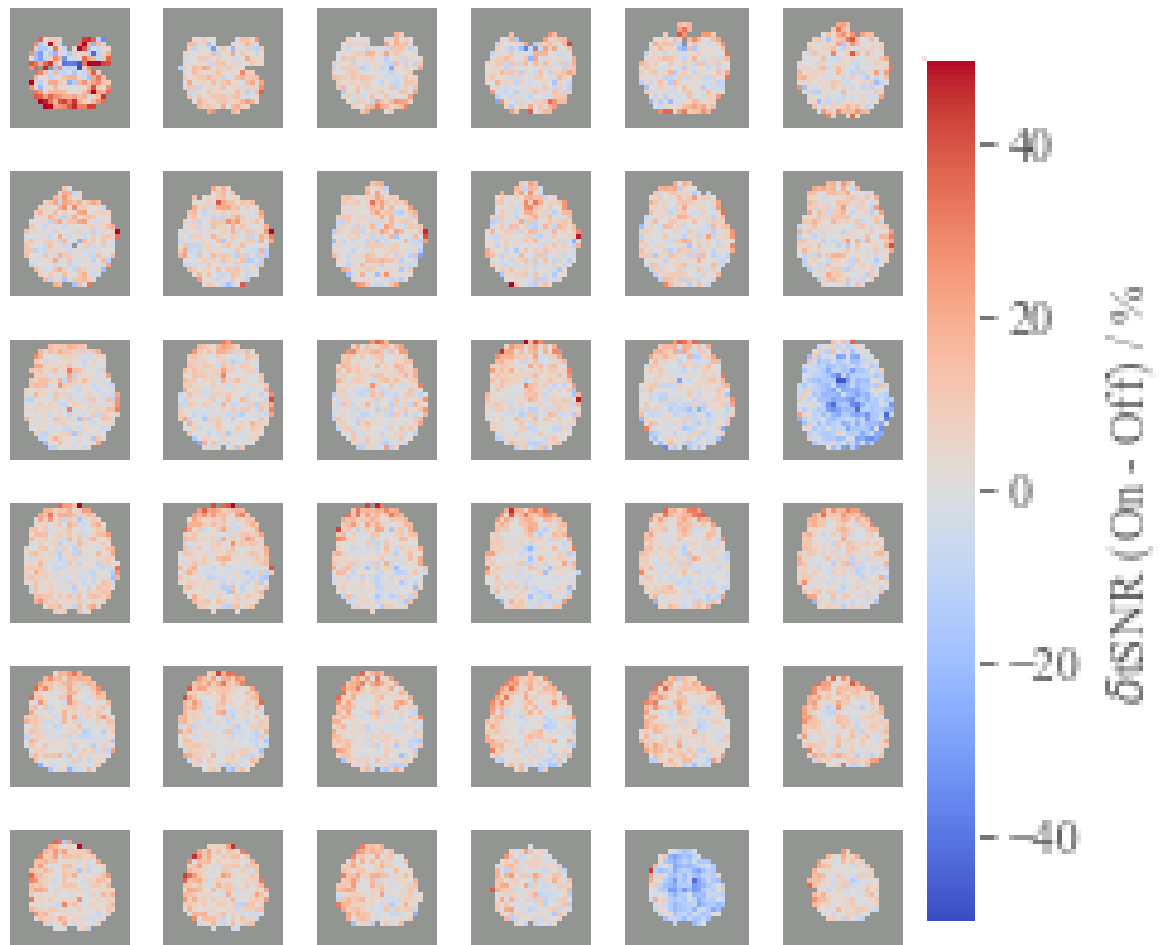


Figure 5.10: Trimmed mean  $\delta tSNR(\text{On-Off})$  of the pTx scans across all subjects. Each subject's  $\delta tSNR$  map was normalised into the standard MNI152 space before the average was calculated.

Figure 5.11 visualises the integrated GLM results for all subjects' scans without and with prospective motion correction, comparing the differences in activation levels.

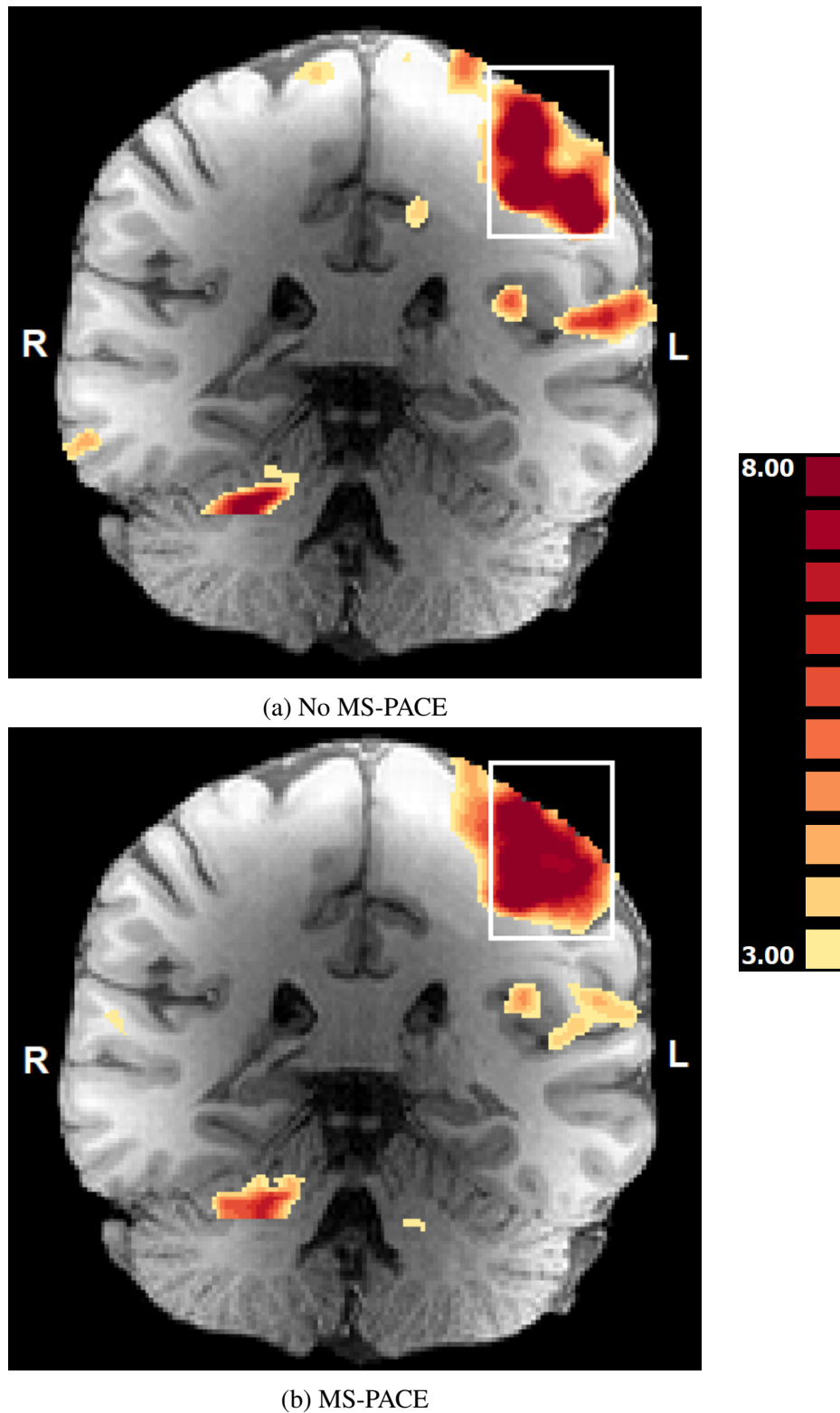


Figure 5.11: Integrated GLM results of all subjects' pTx scans without (a) and with (b) MS-PACE prospective motion correction. The white boxes indicate the location of the hemisphere's primary motor cortex on the Talairach brain (coronal view). The bar scale is of the  $\beta$  weight, which indicates the activation during the task blocks.

### 5.3.2 Comparison of MS-PACE corrected acquisitions in CP and pTx modes

Figure 5.12 displays tSNR maps and percentage differences in tSNR from the MS-PACE-corrected scans acquired in CP and pTx modes in each subject ( $\delta$ tSNR). Higher relative increases in tSNR were observed where the non-corrected scans have low tSNR, and lower when the non-corrected scans have high tSNR. A stark case is subject 6, where the corrected CP scan was heavily affected by motion.



Figure 5.12: Temporal SNR (tSNR) maps and differences ( $\delta$ tSNR) derived from the pTx scans in all six subjects when prospective motion correction was turned off or on. The maps were plotted for slices 16, 26 (centre) and 36 in subject-native EPI space. In each row, the leftmost set of three images are from slice 16, the middle set of three images are from slice 26 and the rightmost set of three images are from slice 36. Within each set of three images, the first column is the tSNR map with MS-PACE turned off, the second column is the tSNR map with MS-PACE turned on, and the third column image is the  $\delta$ tSNR(pTx-CP).

### 5.3. Results

Figure 5.13 shows the average  $\delta tSNR$  maps from the MS-PACE-corrected scans across all subjects normalised into standard MNI space with positive values indicating an increased SNR on pTx mode compared to CP.

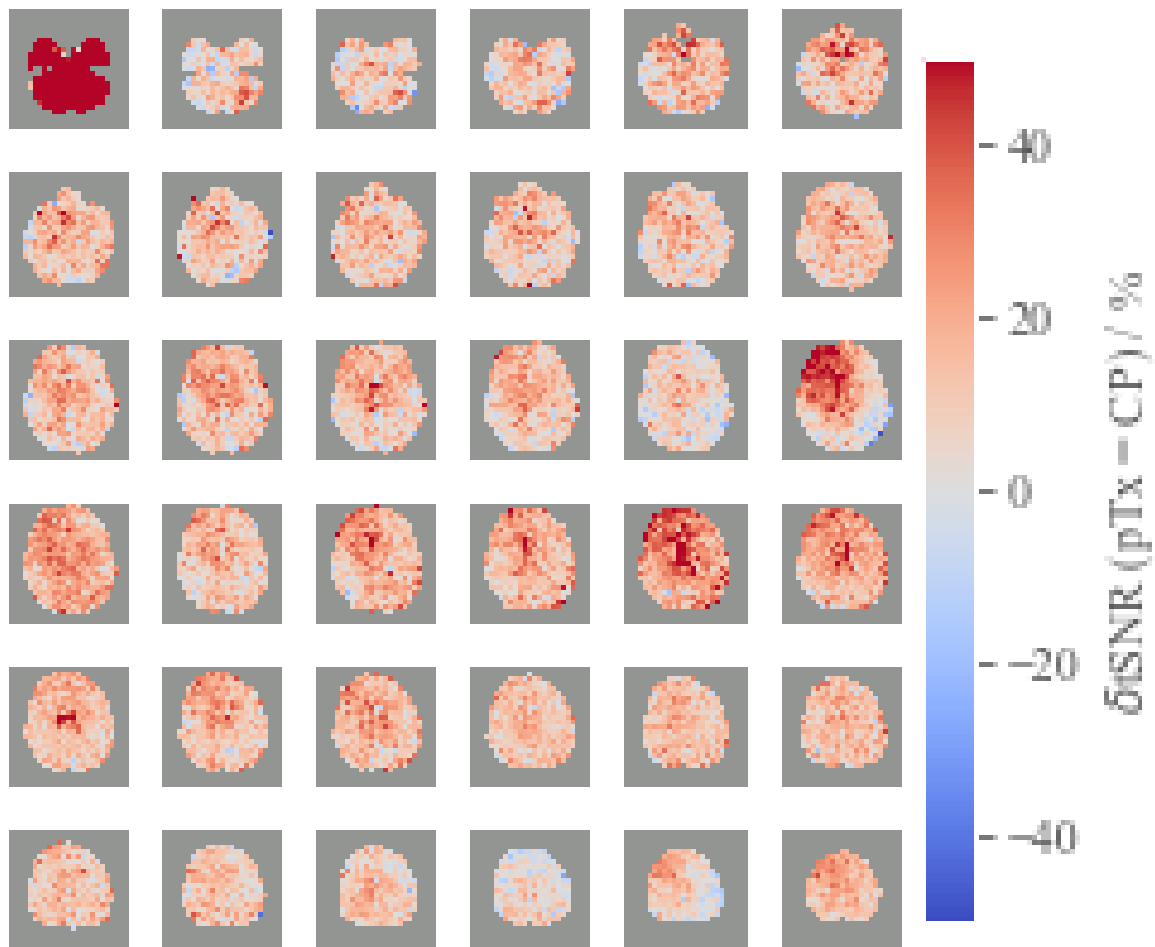


Figure 5.13: Mean  $\delta tSNR$ (pTx-CP) of the MS-PACE prospectively-corrected scans acquired in CP and pTx modes across all subjects. Each subject's  $\delta tSNR$  map was normalised into the standard MNI152 space before the average was calculated.

Figure 5.14 shows the trimmed average, which excludes the extreme ends of the range.

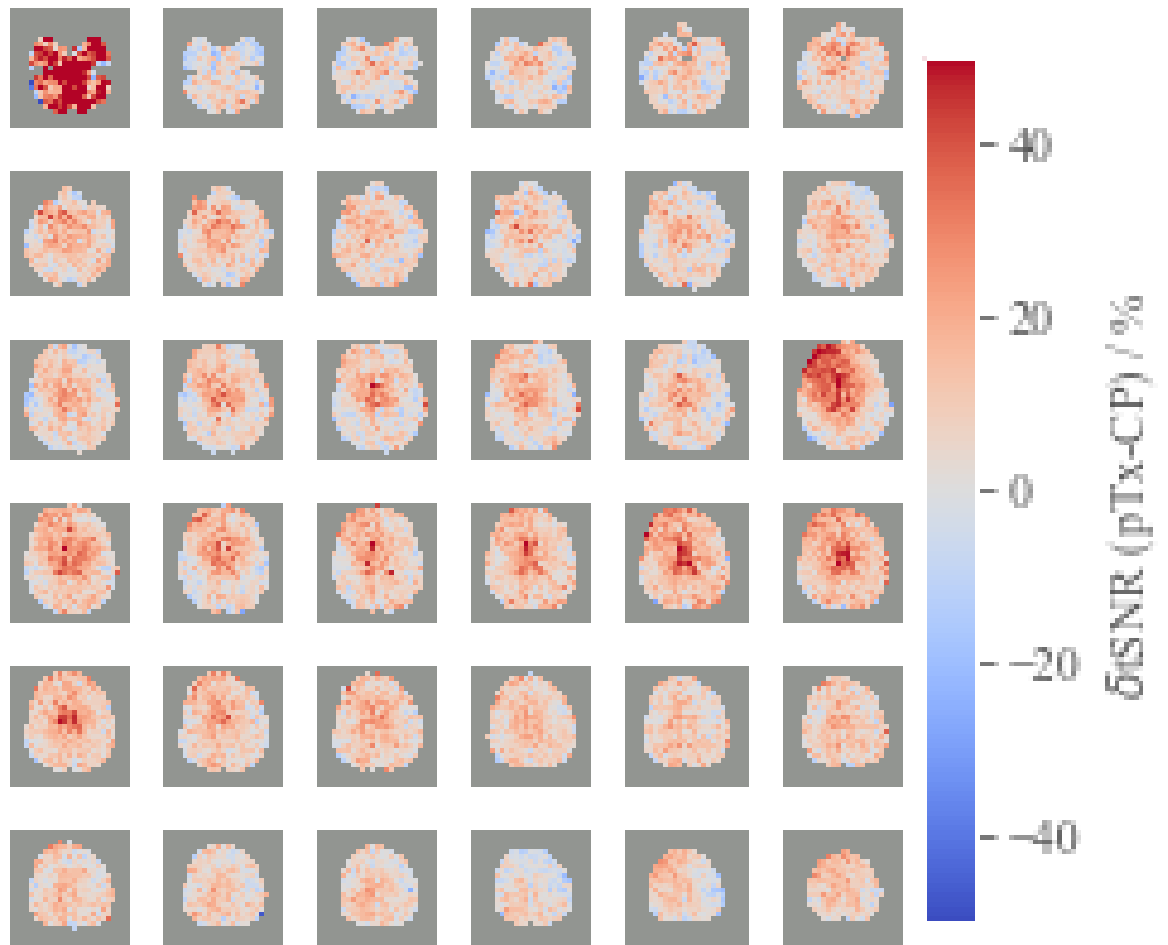


Figure 5.14: Trimmed mean  $\delta tSNR$ (On-Off) of the MS-PACE prospectively-corrected scans acquired in CP and pTx modes. Each subject's  $\delta tSNR$  map was normalised into the standard MNI152 space before the average was calculated.

Figure 5.15 visualises the integrated GLM results for all subjects' scans without and with prospective motion correction, comparing the differences in activation levels.

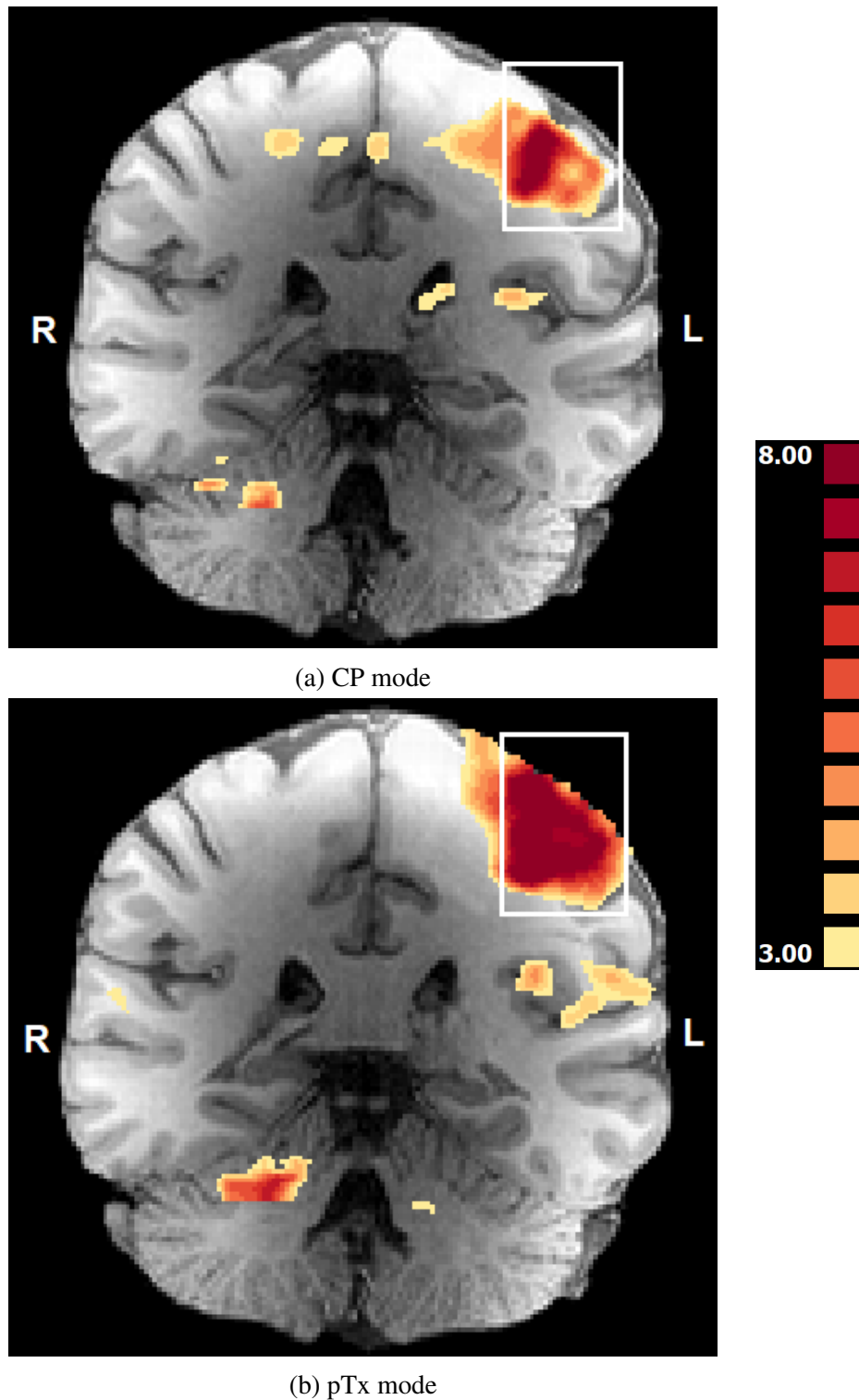


Figure 5.15: Integrated GLM results of all subjects' MS-PACE prospectively-corrected scans acquired on (a) CP and (b) pTx modes. The white boxes indicate the location of the hemisphere's primary motor cortex on the Talairach brain (coronal view). The bar scale is of the  $\beta$  weight, which indicates the activation during the task blocks.

## 5.4 Discussion

### 5.4.1 Application of MS-PACE to data acquisition using pTx

This chapter has described the evaluation of an implementation of the MS-PACE technique that is integrated with pTx scanning at 7T. The motion correction technique was applied to both CP and pTx modes in each subject. Taking advantage of the capability of the individual transmit coils to generate spatially-variable  $B_1^+$  field maps, the maps can be tailored to generate a more homogenous combined transmit field as shown in Figure 5.5. Analysing the mean voxel displacements in the CP and pTx acquisitions (Figures 5.6 and 5.7 respectively), it is observed that MS-PACE was able to reduce overall motion in both modes. This is also supported by the Student t-test statistical evaluation of the mean in both modes (Table 5.2), showing negative values (less displacement with MS-PACE). The p-value is on the 0.05 threshold of statistical significance, indicating that MS-PACE correction and pTx worked in concert successfully. The CP case has a p-value above the threshold, likely affected by an outlier. This exception is subject 6's MS-PACE corrected CP scan. The subject had moved significantly during that specific acquisition, and although real-time motion correction was applied, the scan update time was too long to correct all components of motion. It underlies a limitation of this type of real-time motion correction experiment where a comparison is made between two separate acquisitions in which the underlying motion patterns are variable. It also displays a space for temporal resolution improvements in the future. The MS-PACE implementation used in this work was based on separately-excited slices, which means a lower temporal resolution of scan updates compared to a simultaneously-excited-slices application.

As observed in Figure 5.8, tSNR improvements were observed when MS-PACE motion correction was applied to pTx data acquisition, especially in subjects that moved a lot such as subject 3. The benefits are less prominent in subject data with higher tSNR in the data acquired without MS-PACE and this is reflected on the average  $\delta$ tSNR in Figure 5.9. The trimmed mean, which excludes the extreme values, demonstrates a higher average improvement with prospective motion correction. It is important however to note that the sample size is small. A similar drop in tSNR in several slices akin to Figure 4.5 in Section 4.3 is also observed. As in that study, the slices where tSNR drops occurred were the first few chronologically-acquired slices in every volume and received feedback from a slice subset with low and variable spatial information. Future work can explore the effects of slice location in detail and modify scan protocols and update algorithms to mitigate these effects.

The group-integrated GLM activation map of the pTx prospectively-corrected scans (Fig-

ure 5.11b) demonstrates a high primary motor cortex activation profile. The group activation map from the uncorrected scans in Figure 5.11a also demonstrates high levels of primary motor cortex signal, although with leaked signals in more regions of the brain. Both maps also display activation in the cerebellum, which is also involved in coordinating learned movement and has ipsilateral control (i.e. the right hemisphere controls the right side of the body) unlike the contralateral motor cortex [142].

### 5.4.2 Comparison of MS-PACE corrected acquisitions in CP and pTx modes

This study was performed to confirm that pTx was improving data quality when the RF pulses were updated in real-time as part of the prospective motion correction technique, which was the focus of Chapter 4. The subject-wise comparison in Figure 5.12 and the all-subject average in Figure 5.13 demonstrate overall improvement when pTx was used, especially in the cerebellum (an area that suffers from low  $B_1^+$  in CP mode at UHF [52] [143]), the right frontal lobe and the centre of the brain. But as the sample size is small and the MS-PACE-corrected CP data for subject 6 has particularly low tSNR, the data point might have a significant influence towards the average. After excluding for extremes in Figure 5.14, the preceding observations seem to have remained. Marginal tSNR decreases in the left frontal lobe however have been more accentuated. There is also high tSNR on the first slice due to mask misalignment during the MNI normalisation.

The integrated GLM activation maps in Figure 5.15 demonstrate a broader activation profile in the combined pTx and MS-PACE approach. Comparing this (Figure 5.15b) against the CP equivalent (Figure 5.15a), it can be observed that activation is stronger in the primary motor cortex and the ipsilateral cerebellum region in the former.

## 5.5 Conclusion

This chapter has evaluated an application of the MS-PACE multislice-to-volume prospective motion correction technique with pTx integration at 7T using slice-by-slice  $B_1^+$  shimming. The prospective motion correction technique has been shown to work in most subjects with this pTx integration, with more pronounced spatial benefits in subjects with a higher level of motion during acquisitions. Comparing to the CP application of the technique also demonstrates an overall improvement in tSNR and functional activation signal when a combined MS-PACE and pTx imaging approach was used, with the caveat that the cohort size was relatively small.

# Chapter 6

## Conclusion

### 6.1 Future work

During the work performed in this thesis, several spaces for future improvements and technical developments were identified. The implementation of the prospective motion correction technique can potentially be improved further by introducing more technical features.

Chapter 4 and 5 demonstrated an issue with the realignment of the first acquired slices of a new volume. Optimising the acquisition parameters to explore the effects of using registration information from areas with low and variable spatial information, e.g. superior slices. The acquisition protocol may also be updated to avoid this area to reduce this effect.

While the implementation achieved a high temporal performance, it is still feasible to further improve the temporal resolution further. The integration of simultaneous multislice imaging (SMS) can decrease the repetition time required between volumes by several factors and consequently reduce the time required to acquire slices [39][40][106]. This time can be traded off with increased spatial resolution if desired as well. However, it is also important to note the SAR challenges of using SMS at 7T [40].

Spatial resolution is also an area to be potentially explored in future work. The part of k-space data used for self (EPI) or other sequence navigation could be smaller than the actual acquired data. This can be potentially examined to optimise the trade-off between SNR and spatial resolution, and see what gives the highest accuracy and precision of motion estimates. This may find an application to very high resolution laminar fMRI, when the SNR in the full images might be low [144].

Linked to the potential integration of SMS imaging with MS-PACE, exploratory work was undertaken on another possible area of reduction of motion detection time, namely the use of

## 6.1. Future work

---

unseparated multiband slices for image registration, therefore skipping the separation step and potentially further processing delay (see Appendix A). Extending from this, it was also explored whether a simpler registration of a collapsed slice combined from several (e.g. three) slices in the image registration module can reduce the time required for image registration as there would be just one slice each to be registered between the reference and the moving images. The schematic of this system is shown in Appendix A.5. A complication of implementing this method is that standard image registration algorithms, such as from ITK, would have to be substantially rewritten or replaced. There is also further possibility of applying a machine learning algorithm [145] as a means for more rapid prediction of motion estimates from the unseparated images, or even from raw data.

Applying parallel processing for the ITK image registration modules used to estimate motion parameters also has the possibility to increase the temporal resolution further and capacity for increasing other registration parameters for higher accuracy, such as the number of iteration steps. Another measure that can be used to increase motion estimation accuracy is the introduction of a Kalman filter. This can help to stabilise and smooth the motion parameter estimates especially during outlier motion patterns [100][106]. It is important to consider however that this inclusion might also introduce slight delays.

There are potential benefits of using EPI acquisition as a navigator for prospective correction in a range of 2D pulse sequences. Applying the technique in high-resolution diffusion-weighted imaging (DWI) is a possible area. While it is challenging to use the EPI images in DWI for registration due to the contrast changes with the diffusion weighting and diffusion gradient direction, the high b-value images are low in SNR and an EPI navigator can potentially be used in this case. There is also a high potential impact with standard clinical 2D sequences which do not currently have a method of motion correction available. Prospective motion correction can be crucial in these 2D sequences because retrospective motion correction is not possible if the slice position changes.

If sufficient acceleration from in-plane GRAPPA and SMS is used for the acquisition, the single-shot navigators can potentially also be integrated into multi-shot EPI sequences with spatial resolution-improving methods such as readout-segmented EPI [146][147]. With the improved spatial resolution potential at 7T, an application for navigating structural imaging sequences such as turbo spin echo (TSE) is desirable and has previously been implemented at 3T [6]. Preliminary developmental work was done on translating the technique for 7T application (early results shown in Appendix B).

## 6.2 Summary

This thesis presents the development and applications of an image-based multislice-to-volume prospective motion correction technique for MRI at 7T. Taking into consideration the distinctive challenges of ultra-high field MRI, the technique was developed with novel addition of technical features to mitigate these challenges.

Chapter 3 introduced an implementation of the technique for 7T EPI protocols. In conjunction to pulse sequence and image reconstruction pipeline development, the technique was evaluated in preceding studies on the multislice subset and intra-volume/sub-TR motion. Parallel imaging technique GRAPPA was then incorporated into the implementation to compensate for spatial distortion effects that are more prevalent at higher field strengths, such as 7T. Subsequent application in vivo displayed an ability to correct for motion and improve temporal SNR in long EPI acquisition protocols in subjects with various levels of in-scan motion. The application also compared well with the more commonly-used volumetric registration method.

The work established in Chapter 3 was a foundation for the larger population validation in vivo presented in Chapter 4. In this chapter, the multislice-to-volume technique was extended for application in 7T functional MRI with a task-based paradigm. Compounded by long acquisition times, incidental and stimulus-correlated motion, these protocols are invariably prone to motion artefacts. The motion correction application was shown to have consistently compensated for these effects in the different metrics evaluated and the findings were statistically significant. The positive benefits were especially more visible in acquisitions affected by higher levels of motion.

Addressing one of the main challenges of MRI at 7T, namely  $B_1^+$  field inhomogeneity, the motion correction technique was integrated with parallel transmit imaging in Chapter 5. This work has described for the first time application of the MS-PACE method to 7T and pTx. Integrating subject-specific, slice-by-slice  $B_1^+$  shimming, the combined approach was demonstrated to provide a consistent improvement in image quality and fMRI results in most subjects, especially when higher levels of motion were present. It also favourably compared against the circularly-polarised version, showing overall higher temporal SNR and functional activation.

The work presented in the thesis promises to make neuroimaging more robust at 7T, allowing both clinical and neuroscience applications to benefit consistently from the increased SNR and spatial resolution offered at this field strength. Nonetheless, there are improvements that can be made to further enhance its accuracy and reliability. Recommendations were also made for future applications in other pulse sequences that may potentially benefit from real-time motion correction using multislice-to-volume image registration.



# Appendix A

## Using unseparated multiband slices as an image registration shortcut

*Note: This work was performed with offline processing during the COVID-19 pandemic-related developmental and experimental work disruption. This was later presented at the 2021 Annual Scientific Meeting of the European Society for Magnetic Resonance in Medicine and Biology (ESMRMB) [148]. Due to the incomplete and preliminary nature of this work, it has not been included in the main text. It does, however, present interesting options for future work.*

### A.1 Introduction

When simultaneous multislice (SMS) excitation is used, image registration-based prospective motion correction is typically performed after the SMS-acquired slices are separated into individual slices. This study explored the possibility of programming the motion correction feedback pipeline to register the unseparated/collapsed multiband (MB) slices in a PACE scheme and explore its effects. In PACE, translational and rotational motion estimates are calculated by registering the current imaging volume to a reference volume. These estimates are then used to adjust the slice position and orientation [5]. This also results in a time delay, in addition to the multislice separation-related delay [106]. Registering the volumes without a prior separation of the SMS images (illustrated in Figure A.1) would theoretically allow for quicker processing and an increase in temporal resolution.

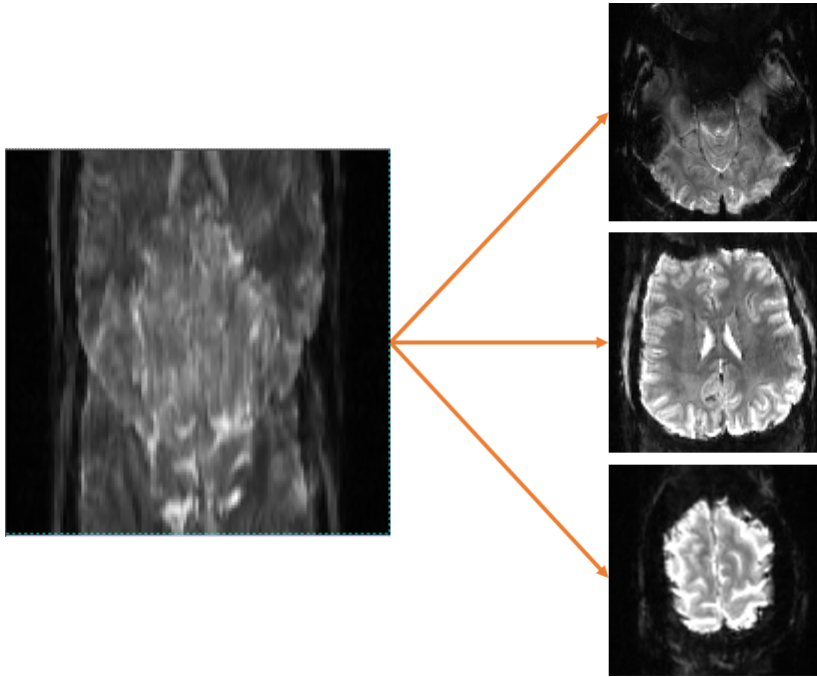


Figure A.1: An unseparated MB slice and its corresponding slices after slice-GRAPPA separation. Notice the folding and aliasing effects on the MB slice.

## A.2 Methods

The study was performed using retrospective calculation of scan data acquired from a healthy 26-year-old volunteer on a Siemens MAGNETOM Terra 7T scanner (Siemens Healthineers, Erlangen, Germany) with a single-transmit, 32-channel receive head coil (Nova Medical, Wilmington, MA, USA). A 2D EPI with BOLD contrast time series was acquired using a Siemens product EPI sequence with the following parameters: 50 volumes, 36 slices, SMS factor 3, TR/TE 2310/25ms, matrix size 128×128, slice thickness 3mm. During the scan, the subject was instructed to perform a motion protocol: 1) nodding up-down; 2) tilting left-right; 3) rotating left-right. Using a processing algorithm developed in the Siemens Image Calculation Environment (ICE) using InsightToolkit (ITK) open-source image registration libraries, volume-to-volume registration was performed for two different scenarios: 1) SMS slices unseparated; 2) SMS slices separated using the slice-GRAPPA method. Transition scans affected by intra-volume motion were excluded.

## A.3 Results

Figure A.2 shows the comparisons of the calculated residual rigid-body motion parameters when volumetric registration was performed with SMS volumes unseparated (blue) and unseparated with slice-GRAPPA.

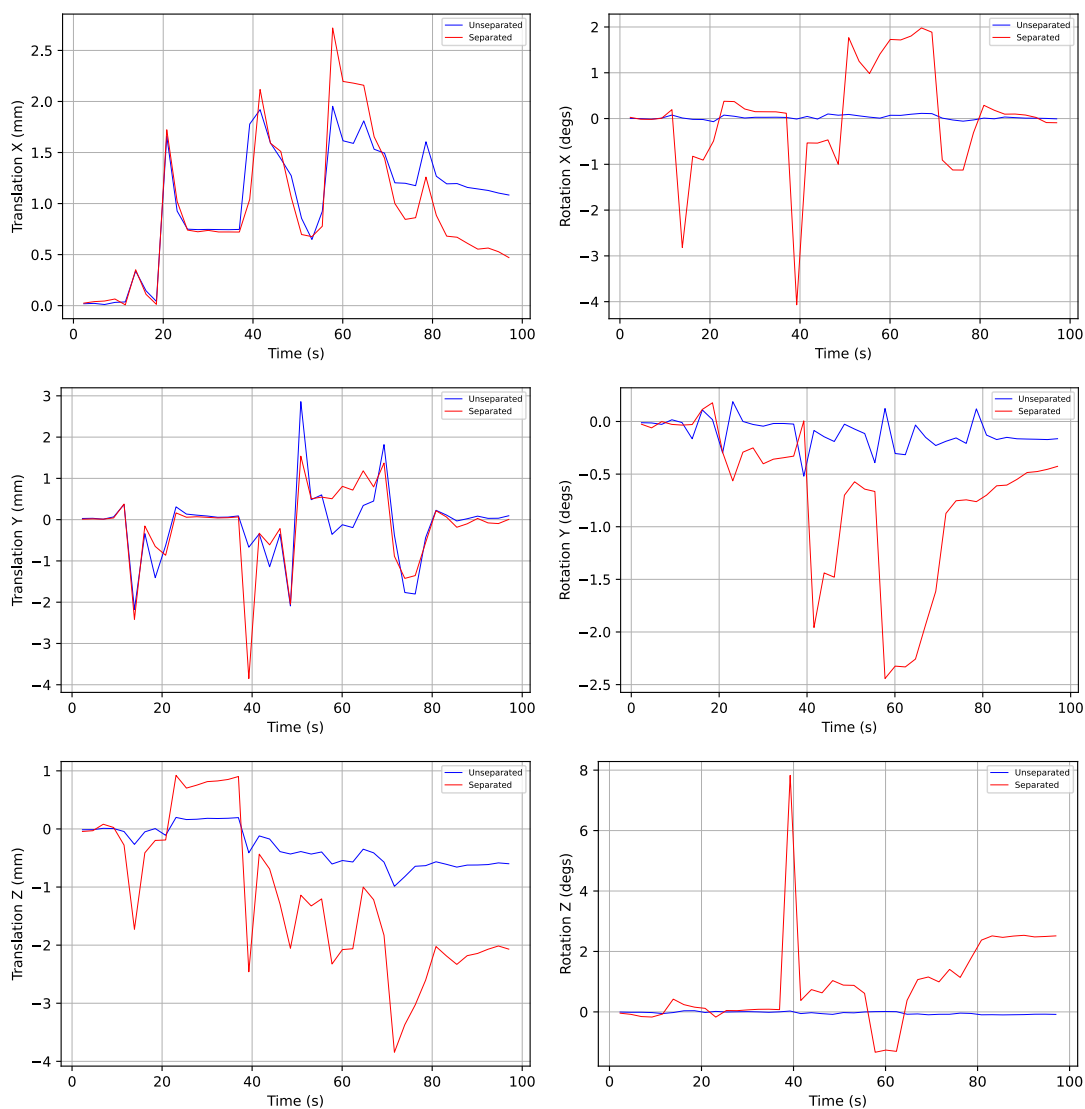


Figure A.2: Residual rigid-body motion parameters (x, y and z-axes) for the unseparated SMS volume registration (blue) and slice-GRAPPA separated SMS volume registration (red). The translation parameters are on the left column, while the rotation parameters are on the right column.

## **A.4 Discussion**

On detecting translational motion, the unseparated slice registration seem to be in close agreement with the separated slice registration, which is the benchmark for this study. However, its sensitivity to through-plane motion, such as z-axis translational and all axes rotational motion was limited. This is likely due to a limitation of the algorithm, where the the position of each aliased slice is not fully considered in the calculation of the residual motion parameters. The image registration algorithm used did not correctly model the effect of rotation on the collapsed data. This loss of slice-direction information complicates determining the through-plane motion parameters. Future work should account for this slice-direction information to estimate through-plane motion parameters more accurately.

## **A.5 Proposed future algorithm**

Following this exploratory work, an algorithm for an expedited image registration process was proposed (illustrated in Figure A.3 below). After skipping the multiband separation process, a collapsed SMS-acquired slice is iterated through a registration process against a pseudo-collapsed reference image generated from earlier-acquired reference data.

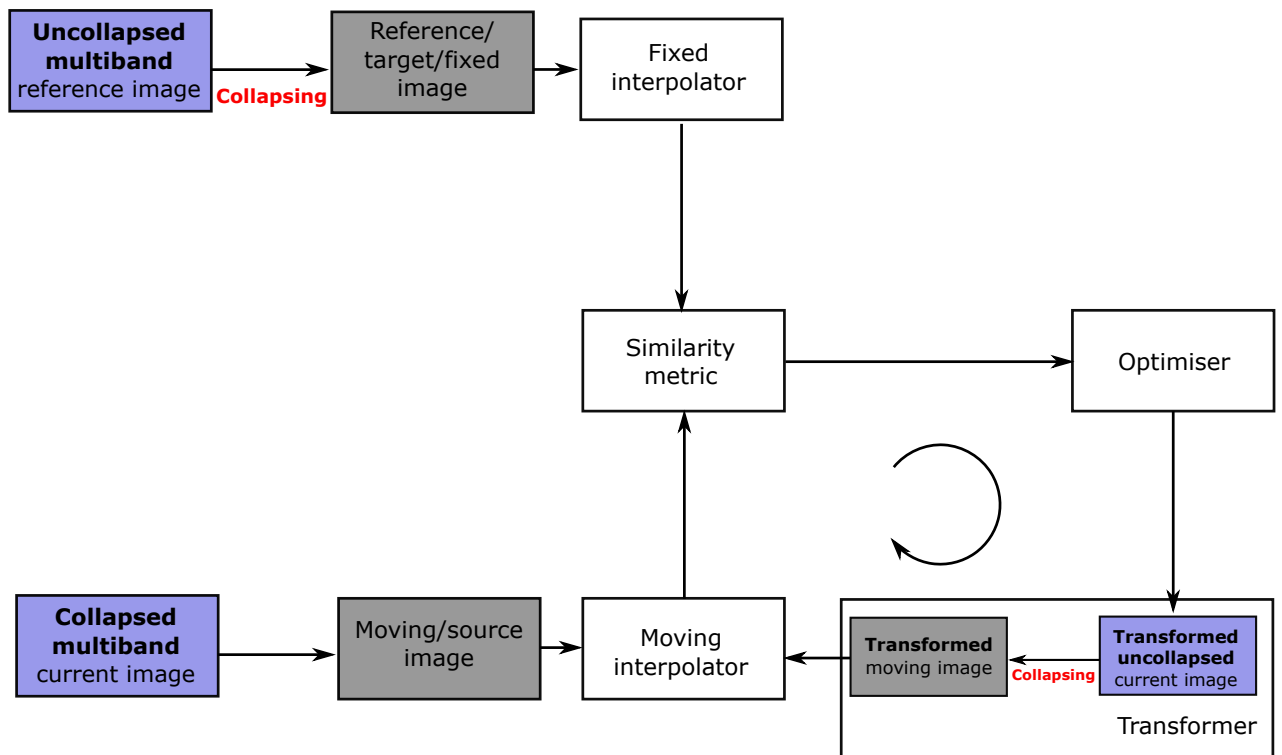


Figure A.3: The schematic of image registration with collapsed multiband slices for simultaneous multislice imaging. After skipping the multiband separation process, a collapsed SMS-acquired slice (current image) is iterated through a registration process against a pseudo-collapsed reference image generated from earlier-acquired reference data.



## Appendix B

# Preliminary work on MS-PACE navigated turbo spin echo (TSE) at 7T

*Note: The images below are from the translation and developmental work of the original 3T MS-PACE TSE technique for 7T application. The base sequence was provided by Dr Daniel Hoinkiss at the Fraunhofer Institute for Digital Medicine MEVIS in Bremen, Germany. This preliminary work made it clear that a dedicated 7T development was required and provided the motivation to base further work on an in-house EPI sequence for the MS-PACE application.*

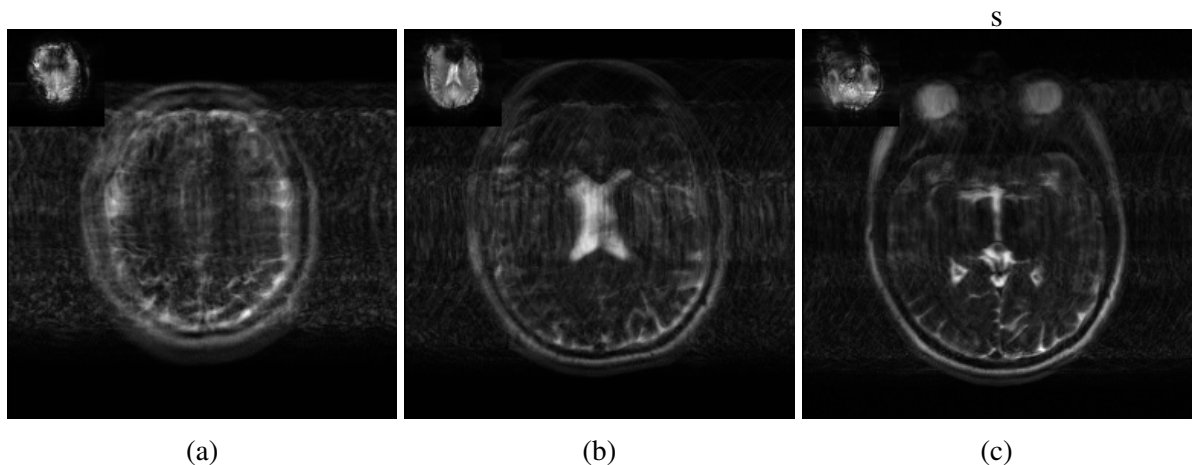


Figure B.1: Inferior (a), centre (b) and superior (c) slices from the 7T MS-PACE-navigated TSE sequence. The inset on the top left are the EPI navigators used for the corresponding TSE slices. Note the heavy blurring artefacts in all slices, reflecting that the application was still under development.



## Published work

- [107] S. Winata et al. “Optimisation of Navigator Parameter for MS-PACE Prospective Motion Correction”. In: *Postgraduate Meeting of British-Irish and Iberian Chapters of the International Society of Magnetic Resonance in Medicine (ISMRM)* (Online, 15–16 Apr. 2021) (cit. on p. 51).
- [108] S. Winata et al. “Navigator Parameter Optimisation for MS-PACE Prospective Motion Correction”. In: *Proceedings of the 2021 Annual Meeting of the British-Irish Chapter of the International Society of Magnetic Resonance in Medicine (ISMRM) "MR-FEST"* (Online, 13–17 Sept. 2021), p. 27 (cit. on pp. 51, 71).
- [109] S. Winata et al. “Optimising Navigator Scans for Use in MRI Prospective Motion Correction”. In: *15th Scottish Imaging Network: A Platform for Scientific Excellence (SINAPSE) Annual Scientific Meeting* (Online, 16–17 Sept. 2021) (cit. on p. 51).
- [110] S. Winata et al. “Multislice-to-volume registration for detecting intra-volume motion in 7T EPI”. In: *28th Organisation of Human Brain Mapping Annual Meeting (OHBM) Annual Meeting* (Glasgow, Scotland, UK, 19–23 June 2022) (cit. on p. 52).
- [111] S. Winata et al. “Multislice-to-volume Prospective Motion Correction for Functional MRI Protocols at 7T”. In: *Proceedings of the 2023 Annual Meeting of the International Society of Magnetic Resonance in Medicine (ISMRM)* (Toronto, Ontario, Canada, 3–8 June 2023) (cit. on p. 52).
- [112] S. Winata et al. “Prospective Motion Correction for Functional MRI at 7T using Multislice-to-Volume Image Registration”. In: *28th Organisation of Human Brain Mapping Annual Meeting (OHBM) Annual Meeting* (Montreal, Quebec, Canada, 22–26 July 2023) (cit. on p. 52).
- [117] S. Winata et al. “Real-time multislice-to-volume motion correction for task-based functional MRI at 7T”. In: *39th Annual Scientific Meeting of the European Society for Mag-*

*netic Resonance in Medicine and Biology (ESMRMB)* (Basel, Switzerland, 4–10 Oct. 2023) (cit. on p. 74).

- [118] S. Winata et al. “Real-time image-based motion correction for 7T task-based functional MRI.” In: *15th Scottish Imaging Network: A Platform for Scientific Excellence (SINAPSE) Annual Scientific Meeting* (Glasgow, Scotland, UK, 14 June 2023) (cit. on p. 74).
- [134] S. Winata et al. “Parallel transmit imaging with real-time multislice-to-volume motion correction for task-based functional MRI at 7T”. In: *39th Annual Scientific Meeting of the European Society for Magnetic Resonance in Medicine and Biology (ESMRMB)* (Basel, Switzerland, 4–10 Oct. 2023) (cit. on p. 92).
- [148] S. Winata et al. “Image Registration Shortcut for Prospective Motion Correction Using Unseparated Multiband Slices”. In: *38th Annual Scientific Meeting of the European Society for Magnetic Resonance in Medicine and Biology (ESMRMB)* (Online, 7–9 Oct. 2021). Vol. 34. *Magnetic Resonance Materials in Physics, Biology and Medicine*, pp. 132–133. DOI: 10.1007/s10334-021-00947-8 (cit. on p. 113).

# Bibliography

- [1] J. B. Andre et al. “Toward quantifying the prevalence, severity, and cost associated with patient motion during clinical MR examinations”. In: *Journal of the American College of Radiology* 12.7 (2015), pp. 689–695 (cit. on p. 1).
- [2] M. Zaitsev, J. Maclaren and M. Herbst. “Motion artifacts in MRI: A complex problem with many partial solutions”. In: *Journal of Magnetic Resonance Imaging* 42.4 (2015), pp. 887–901. DOI: 10.1002/jmri.24850. eprint: 15334406 (cit. on pp. 1, 35, 38, 39, 45).
- [3] J. Schulz et al. “An embedded optical tracking system for motion-corrected magnetic resonance imaging at 7T”. In: *Magnetic Resonance Materials in Physics, Biology and Medicine* 25.6 (2012), pp. 443–453. ISSN: 09685243. DOI: 10.1007/s10334-012-0320-0 (cit. on pp. 1, 38).
- [4] A. G. Webb and C. M. Collins. “Parallel transmit and receive technology in high-field magnetic resonance neuroimaging”. In: *International Journal of Imaging Systems and Technology* 20.1 (2010), pp. 2–13. DOI: <https://doi.org/10.1002/ima.20219> (cit. on pp. 1, 34, 35).
- [5] S. Thesen et al. “Prospective Acquisition Correction for head motion with image-based tracking for real-time fMRI”. In: *Magnetic Resonance in Medicine* 44.3 (2000), pp. 457–465. DOI: 10.1002/1522-2594(200009)44:3<457::AID-MRM17>3.0.CO;2-R (cit. on pp. 2, 43–45, 47, 52, 113).
- [6] D. C. Hoinkiss and D. A. Porter. “Prospective motion correction in 2D multishot MRI using EPI navigators and multislice-to-volume image registration”. In: *Magnetic Resonance in Medicine* 78.6 (2017), pp. 2127–2135. ISSN: 15222594. DOI: 10.1002/mrm.26951 (cit. on pp. 2, 47, 110).

- [7] M. A. Griswold et al. “Generalized autocalibrating partially parallel acquisitions (GRAPPA)”. In: *Magnetic Resonance in Medicine* 47 (2002), pp. 1202–1210. ISSN: 0740-3194. DOI: 10.1002/mrm.10171 (cit. on pp. 2, 23, 32, 39, 53).
- [8] O. Speck, J. Stadler and M. Zaitsev. “High resolution single-shot EPI at 7T”. In: *Magnetic Resonance Materials in Physics, Biology and Medicine* 21 (2008), pp. 73–86. DOI: 10.1007/s10334-007-0087-x (cit. on pp. 2, 26, 53).
- [9] T. T. Liu. “Noise contributions to the fMRI signal: An overview”. In: *NeuroImage* 143 (2016), pp. 141–151. ISSN: 1053-8119. DOI: <https://doi.org/10.1016/j.neuroimage.2016.09.008> (cit. on p. 2).
- [10] A. M. Smith et al. “Investigation of Low Frequency Drift in fMRI Signal”. In: *NeuroImage* 9.5 (1999), pp. 526–533. DOI: <https://doi.org/10.1006/nimg.1999.0435> (cit. on p. 2).
- [11] J. V. Hajnal et al. “Artifacts due to stimulus correlated motion in functional imaging of the brain”. In: *Magnetic Resonance in Medicine* 31.3 (1994), pp. 283–291. DOI: <https://doi.org/10.1002/mrm.1910310307> (cit. on p. 2).
- [12] K. J. Friston et al. “Movement-Related effects in fMRI time-series”. In: *Magnetic Resonance in Medicine* 35.3 (1996), pp. 346–355. DOI: <https://doi.org/10.1002/mrm.1910350312> (cit. on p. 2).
- [13] T. L. Davis et al. “Calibrated functional MRI: Mapping the dynamics of oxidative metabolism”. In: *Proceedings of the National Academy of Sciences* 95.4 (1998), pp. 1834–1839. DOI: 10.1073/pnas.95.4.1834 (cit. on pp. 3, 37).
- [14] C.-G. Yan et al. “A comprehensive assessment of regional variation in the impact of head micromovements on functional connectomics”. In: *NeuroImage* 76 (2013), pp. 183–201. DOI: <https://doi.org/10.1016/j.neuroimage.2013.03.004> (cit. on p. 3).
- [15] F. Bloch. “Nuclear induction”. In: *Physical Review* 70.7-8 (1946), pp. 470–474. DOI: 10.1016/0031-8914(51)90068-7 (cit. on pp. 5, 14).
- [16] E. M. Purcell, H. C. Torrey and R. V. Pound. “Resonance absorption by nuclear magnetic moments in a solid”. In: *Physical Review* 69.1-2 (1946), pp. 37–38. DOI: 10.1103/PhysRev.69.37 (cit. on p. 5).
- [17] T. P. L. Roberts and D. Mikulis. “Neuro MR: Principles”. In: *Journal of Magnetic Resonance Imaging* 26.4 (2007), pp. 823–837. DOI: 10.1002/jmri.21029 (cit. on p. 5).

- [18] E. Moser et al. “Ultra-high field NMR and MRI-the role of magnet technology to increase sensitivity and specificity”. In: *Frontiers in Physics* 5 (2017), pp. 1–15. ISSN: 2296424X. DOI: 10.3389/fphy.2017.00033 (cit. on p. 5).
- [19] M. Sarracanie and N. Salameh. “Low-Field MRI: How Low Can We Go? A Fresh View on an Old Debate”. In: *Frontiers in Physics* 8 (2020), pp. 1–14. ISSN: 2296424X. DOI: 10.3389/fphy.2020.00172 (cit. on p. 5).
- [20] R. W. Brown et al. *Magnetic Resonance Imaging: Physical Principles and Sequence Design*. Wiley, 2014. ISBN: 978-0-4717-2085-0 (cit. on pp. 6, 7).
- [21] M. A. Bernstein, K. F. King and X. J. Zhou. *Handbook of MRI Pulse Sequences*. Elsevier Academic, 2001. ISBN: 978-0-7817-7929-6 (cit. on p. 6).
- [22] P. Jezzard, P. M. Matthews and S. A. Smith. *Functional Magnetic Resonance Imaging: An Introduction to Methods*. Oxford University Press, 2012. ISBN: 978-0-1917-2477-0 (cit. on p. 6).
- [23] J. Keeler. *Understanding NMR spectroscopy*. University of Cambridge, 2006 (cit. on p. 6).
- [24] W. Pauli. “Zur Frage der theoretischen Deutung der Satelliten einiger Spektrallinien und ihrer Beeinflussung durch magnetische Felder”. In: *Naturwissenschaften* 12.37 (1924), pp. 741–743 (cit. on p. 6).
- [25] H. Nyquist. “Certain Topics in Telegraph Transmission Theory”. In: *Transactions of the American Institute of Electrical Engineers* (1928) (cit. on p. 17).
- [26] C. Shannon. “Communication in the Presence of Noise”. In: *Proceedings of the IRE* 37.1 (1949), pp. 10–21. DOI: 10.1109/JRPROC.1949.232969 (cit. on p. 17).
- [27] J. Frahm, A. Haase and D. Matthaei. “Rapid NMR imaging of dynamic processes using the FLASH technique”. In: *Magnetic Resonance in Medicine* 3.2 (1986), pp. 321–327. DOI: <https://doi.org/10.1002/mrm.1910030217> (cit. on p. 20).
- [28] E. L. Hahn. “Spin Echoes”. In: *Physical Review* 80 (1950), pp. 580–594 (cit. on p. 21).
- [29] J. Hennig, A. Nauerth and H. Friedburg. “RARE Imaging - A Fast Imaging Method for Clinical MR.pdf”. In: *Magnetic Resonance in Medicine* 3 (1986), pp. 823–833 (cit. on pp. 23, 29).
- [30] D. W. McRobbie et al. *MRI: From picture to proton*. Second. Cambridge University Press, 2006. ISBN: 9781107706958. DOI: 10.2214/ajr.182.3.1820592 (cit. on p. 22).

## Bibliography

---

- [31] K. P. Pruessmann et al. “SENSE: Sensitivity Encoding for Fast MRI”. In: *Magnetic Resonance in Medicine* 42 (1999), pp. 952–962 (cit. on p. 23).
- [32] P. B. Roemer et al. “The NMR Phased Array”. In: *Magnetic Resonance in Medicine* 16.2 (1990), pp. 192–225 (cit. on p. 25).
- [33] P. Mansfield. “Multi-planar image formation using NMR spin echoes”. In: *Journal of Physics C: Solid State Physics* 10.3 (1977). ISSN: 00223719. DOI: 10.1088/0022-3719/10/3/004 (cit. on p. 26).
- [34] H. Bruder et al. “Image reconstruction for echo planar imaging with nonequidistant k-space sampling”. In: *Magnetic Resonance in Medicine* 23.2 (1992), pp. 311–323. ISSN: 15222594. DOI: 10.1002/mrm.1910230211 (cit. on p. 27).
- [35] A. Jesmanowicz, E. C. Wong and J. S. Hyde. “Phase Correction for EPI Using Internal Reference Lines”. In: *Proceedings of the 12th Annual Meeting of the Society of Magnetic Resonance in Medicine, New York*. 1993, p. 129 (cit. on p. 27).
- [36] D. C. Alsop. “The Sensitivity of Low Flip Angle RARE Imaging”. In: *Magnetic Resonance in Medicine* 37 (1997), pp. 176–184 (cit. on p. 29).
- [37] P. A. Hardy et al. “Why Fat Is Bright in RARE and Fast Spin-Echo Imaging”. In: *Journal of Magnetic Resonance Imaging* 2.5 (1992), pp. 533–540. DOI: <https://doi.org/10.1002/jmri.1880020511> (cit. on p. 29).
- [38] T. Li and S. A. Mirowitz. “Fast T2-weighted MR imaging: Impact of variation in pulse sequence parameters on image quality and artifacts”. In: *Magnetic Resonance Imaging* 21.7 (2003), pp. 745–753. DOI: 10.1016/S0730-725X(03)00173-5 (cit. on p. 29).
- [39] D. A. Feinberg and K. Setsompop. “Ultra-fast MRI of the human brain with simultaneous multi-slice imaging”. In: *Journal of Magnetic Resonance* 229 (2013), pp. 90–100. ISSN: 10907807. DOI: 10.1016/j.jmr.2013.02.002 (cit. on pp. 31, 39, 109).
- [40] S. Moeller et al. “Multiband multislice GE-EPI at 7 tesla, with 16-fold acceleration using partial parallel imaging with application to high spatial and temporal whole-brain fMRI”. In: *Magnetic Resonance in Medicine* 63.5 (2010), pp. 1144–1153. ISSN: 07403194. DOI: 10.1002/mrm.22361 (cit. on pp. 31, 109).
- [41] F. A. Breuer et al. “Controlled aliasing in parallel imaging results in higher acceleration (CAIPIRINHA) for multi-slice imaging”. In: *Magnetic Resonance in Medicine* 53.3 (2005), pp. 684–691. ISSN: 07403194. DOI: 10.1002/mrm.20401 (cit. on p. 31).

- [42] K. Setsompop et al. “Blipped-controlled aliasing in parallel imaging for simultaneous multislice echo planar imaging with reduced g-factor penalty”. In: *Magnetic Resonance in Medicine* 67.5 (2012), pp. 1210–1224. ISSN: 07403194. DOI: 10.1002/mrm.23097 (cit. on pp. 31, 32).
- [43] V. Olafsson et al. “Enhanced identification of BOLD-like components with multi-echo simultaneous multi-slice (MESMS) fMRI and multi-echo ICA”. In: *NeuroImage* 112 (2015). ISSN: 10959572. DOI: 10.1016/j.neuroimage.2015.02.052 (cit. on p. 31).
- [44] M. Barth et al. “Simultaneous multislice (SMS) imaging techniques”. In: *Magnetic Resonance in Medicine* 75.1 (2016), pp. 63–81. ISSN: 15222594. DOI: 10.1002/mrm.25897 (cit. on pp. 31, 32).
- [45] S. Sammet. “Ultra-high Field MRI 7T and above - Safety and Challenges”. In: *Proceedings of the ISMRM* 20 (2012) (cit. on pp. 31, 35).
- [46] A. Sharma, M. Lustig and W. A. Grissom. “Root-flipped multiband refocusing pulses”. In: *Magnetic Resonance in Medicine* 75.1 (2016), pp. 227–237. ISSN: 15222594. DOI: 10.1002/mrm.25629 (cit. on p. 31).
- [47] D. G. Norris et al. “Power independent of number of slices (PINS) radiofrequency pulses for low-power simultaneous multislice excitation”. In: *Magnetic Resonance in Medicine* 66.5 (2011), pp. 1234–1240. ISSN: 07403194. DOI: 10.1002/mrm.23152 (cit. on p. 32).
- [48] D. Hoult and P. C. Lauterbur. “The sensitivity of the zeugmatographic experiment involving human samples”. In: *Journal of Magnetic Resonance* 34.2 (1979), pp. 425–433. ISSN: 0022-2364 (cit. on p. 34).
- [49] R. Pohmann, O. Speck and K. Scheffler. “Signal-to-noise ratio and MR tissue parameters in human brain imaging at 3, 7, and 9.4 tesla using current receive coil arrays”. In: *Magnetic Resonance in Medicine* 75.2 (2016), pp. 801–809. DOI: 10.1002/mrm.25677 (cit. on p. 34).
- [50] S. N. Williams, P. McElhinney and G. Shajan. “Ultra-high field MRI: parallel-transmit arrays and RF pulse design”. In: *Physics in Medicine and Biology* 68.2 (2023). DOI: 10.1088/1361-6560/aca4b7 (cit. on pp. 34, 36).
- [51] N. K. Bangerter et al. “Quantitative techniques for musculoskeletal MRI at 7 Tesla”. In: *Quantitative Imaging in Medicine and Surgery* 6.6 (2016), pp. 715–730. ISSN: 22234306. DOI: 10.21037/qims.2016.12.12 (cit. on p. 35).

- [52] F. Padormo et al. “Parallel transmission for ultrahigh-field imaging”. In: *NMR in Biomedicine* 29.9 (2016), pp. 1145–1161. ISSN: 10991492. DOI: 10.1002/nbm.3313 (cit. on pp. 35, 108).
- [53] B. van den Bergen et al. “7 T body MRI: B1 shimming with simultaneous SAR reduction”. In: *Physics in Medicine and Biology* 52.17 (2007), pp. 5429–5441. ISSN: 00319155. DOI: 10.1088/0031-9155/52/17/022 (cit. on p. 35).
- [54] P. Balchandani and T. P. Naidich. “Ultra-high-field MR neuroimaging”. In: *American Journal of Neuroradiology* 36.7 (2015), pp. 1204–1215. ISSN: 1936959X. DOI: 10.3174/ajnr.A4180 (cit. on p. 35).
- [55] S. Ogawa et al. “Brain magnetic resonance imaging with contrast dependent on blood oxygenation”. In: *Proceedings of the National Academy of Sciences of the United States of America* 87.24 (1990), pp. 9868–9872. ISSN: 00278424. DOI: 10.1073/pnas.87.24.9868 (cit. on pp. 36, 73).
- [56] V. Muoio, P. B. Persson and M. M. Sendeski. “The neurovascular unit – concept review”. In: *Acta Physiologica* 210.4 (2014), pp. 790–798. DOI: <https://doi.org/10.1111/apha.12250> (cit. on p. 36).
- [57] S. Posse et al. “Enhancement of BOLD-contrast sensitivity by single-shot multi-echo functional MR imaging”. In: *Magnetic Resonance in Medicine* 42.1 (1999), pp. 87–97 (cit. on p. 37).
- [58] B. Biswal et al. “Functional Connectivity in the Motor Cortex of Resting Human Brain Using Echo-Planar MRI”. In: *Magnetic Resonance in Medicine* 34 (Oct. 1995), pp. 537–541. DOI: 10.1002/mrm.1910340409 (cit. on p. 37).
- [59] W. van der Zwaag et al. “fMRI at 1.5, 3 and 7 T: Characterising BOLD signal changes”. In: *NeuroImage* 47.4 (2009), pp. 1425–1434. ISSN: 10538119. DOI: 10.1016/j.neuroimage.2009.05.015 (cit. on pp. 37, 53).
- [60] Z. Munn and Z. Jordan. “The patient experience of high technology medical imaging: A systematic review of the qualitative evidence”. In: *Radiography* 17 (2011), pp. 323–331. ISSN: 1078-8174. DOI: 10.1016/J.RADI.2011.06.004 (cit. on p. 37).
- [61] C. Federau and D. Gallichan. “Motion-correction enabled ultra-high resolution in-vivo 7T-MRI of the brain”. In: *PLoS ONE* 11.5 (2016), pp. 1–12. ISSN: 19326203. DOI: 10.1371/journal.pone.0154974 (cit. on p. 37).

- [62] F. Godenschweger et al. “Motion correction in MRI of the brain”. In: *Physics in Medicine and Biology* 61.5 (2016), R32–R56. ISSN: 13616560. DOI: 10.1088/0031-9155/61/5/R32 (cit. on pp. 38, 40).
- [63] D. Stucht et al. “Highest resolution in vivo human brain MRI using prospective motion correction”. In: *PLoS ONE* 10.7 (2015), pp. 1–17. ISSN: 19326203. DOI: 10.1371/journal.pone.0133921 (cit. on p. 38).
- [64] M. Herbst et al. “Reproduction of Motion Artifacts for Performance Analysis of Prospective Motion Correction in MRI”. In: *Magnetic Resonance in Medicine* 71.1 (2015), pp. 1–17. DOI: 10.1002/mrm.24645.Reproduction (cit. on p. 38).
- [65] M. E. Ladd et al. “Pros and cons of ultra-high-field MRI/MRS for human application”. In: *Progress in Nuclear Magnetic Resonance Spectroscopy* 109 (2018), pp. 1–50. ISSN: 00796565. DOI: 10.1016/j.pnmrs.2018.06.001 (cit. on p. 38).
- [66] C. Heilmaier et al. “A large-scale study on subjective perception of discomfort during 7 and 1.5T MRI examinations”. In: *Bioelectromagnetics* 32.8 (2011), pp. 610–619. ISSN: 01978462. DOI: 10.1002/bem.20680 (cit. on p. 38).
- [67] J. Liu et al. “Effect of head motion on MRI B0 field distribution”. In: *Magnetic Resonance in Medicine* 80.6 (2018), pp. 2538–2548 (cit. on p. 38).
- [68] R. Bammer et al. “Impact of motion on parallel transmission”. In: *Proceedings of the 19th Annual Meeting of the Society of Magnetic Resonance in Medicine*. 1993, p. 4590 (cit. on p. 38).
- [69] E. M. Bellon et al. “MR Artifacts: A Review”. In: *American Journal of Roentgenology* 147.6 (1986), pp. 1271–1281 (cit. on p. 38).
- [70] R. B. van Heeswijk et al. “Motion compensation strategies in magnetic resonance imaging”. In: *Critical Reviews in Biomedical Engineering* 40.2 (2012), pp. 99–119. ISSN: 0278940X. DOI: 10.1615/CritRevBiomedEng.v40.i2.20 (cit. on p. 38).
- [71] V. Edward et al. “Quantification of fMRI artifact reduction by a novel plaster cast head holder”. In: *Human Brain Mapping* 11.3 (2000), pp. 207–213. ISSN: 10659471 (cit. on pp. 38, 39).
- [72] V. Bettinardi et al. “Head holder for PET, CT, and MR studies”. In: *Journal of computer assisted tomography* 15.5 (1991), pp. 886–892 (cit. on p. 39).

- [73] S. Malviya et al. “Sedation and general anaesthesia in children undergoing MRI and CT: Adverse events and outcomes”. In: *British Journal of Anaesthesia* 84.6 (2000), pp. 743–748. DOI: 10.1093/oxfordjournals.bja.a013586 (cit. on p. 39).
- [74] D. J. Larkman et al. “Use of multicoil arrays for separation of signal from multiple slices simultaneously excited”. In: *Journal of Magnetic Resonance Imaging* 13.2 (2002), pp. 313–317 (cit. on p. 39).
- [75] P. G. Batchelor et al. “Matrix description of general motion correction applied to multishot images”. In: *Magnetic Resonance in Medicine* 54.5 (2005), pp. 1273–1280. DOI: 10.1002/mrm.20656 (cit. on p. 40).
- [76] T. E. Wallace et al. “Head motion measurement and correction using FID navigators”. In: *Magnetic Resonance in Medicine* 81.1 (2019), pp. 258–274. ISSN: 15222594. DOI: 10.1002/mrm.27381 (cit. on p. 40).
- [77] D. Gallichan, J. P. Marques and R. Gruetter. “Retrospective correction of involuntary microscopic head movement using highly accelerated fat image navigators (3D FatNavs) at 7T”. In: *Magnetic Resonance in Medicine* 75.3 (2016), pp. 1030–1039. DOI: 10.1002/mrm.25670 (cit. on p. 40).
- [78] J. G. Pipe. “Motion correction with PROPELLER MRI: Application to head motion and free-breathing cardiac imaging”. In: *Magnetic Resonance in Medicine* 42.5 (1999), pp. 963–969 (cit. on p. 40).
- [79] X. Hu et al. “Retrospective estimation and correction of physiological fluctuation in functional MRI”. In: *Magnetic Resonance in Medicine* 34.2 (1995), pp. 201–212. DOI: 10.1002/mrm.1910340211 (cit. on p. 40).
- [80] M. Zaitsev et al. “Magnetic resonance imaging of freely moving objects: prospective real-time motion correction using an external optical motion tracking system”. In: *Neuroimage* 31.3 (2006), pp. 1038–1050 (cit. on pp. 40, 44).
- [81] J. Fessler. “Model-based image reconstruction for MRI”. In: *IEEE Signal Processing Magazine* 27.4 (2010), pp. 81–89. DOI: 10.1109/MSP.2010.936726 (cit. on p. 40).
- [82] D. Atkinson et al. “Automatic correction of motion artifacts in magnetic resonance images using an entropy focus criterion”. In: *IEEE Transactions on Medical Imaging* 16.6 (1997), pp. 903–910. ISSN: 02780062. DOI: 10.1109/42.650886 (cit. on p. 40).
- [83] D. Atkinson et al. “Automatic compensation of motion artifacts in MRI”. In: *Magnetic Resonance in Medicine* 41.1 (1999), pp. 163–170 (cit. on p. 40).

- [84] K. P. McGee et al. “Image metric-based correction (Autocorrection) of motion effects: Analysis of image metrics”. In: *Journal of Magnetic Resonance Imaging* 11.2 (2000), pp. 174–181 (cit. on p. 40).
- [85] J. M. Fitzpatrick, D. L. G. Hill and C. R. Maurer. “Handbook of Medical Imaging, Volume 2. Medical Image Processing and Analysis - Chapter 8 Image Registration”. In: *SPIE Press* (2004), pp. 447–514 (cit. on p. 41).
- [86] D. Mattes et al. “Nonrigid multimodality image registration”. In: *Proceedings of SPIE - The International Society for Optical Engineering*. Vol. 4322. 2001, pp. 1609–1620 (cit. on p. 42).
- [87] D. Mattes et al. “PET-CT image registration in the chest using free-form deformations”. In: *IEEE Transactions on Medical Imaging* 22.1 (2003), pp. 120–128 (cit. on p. 42).
- [88] E. Ferrante and N. Paragios. “Slice-to-volume medical image registration: A survey”. In: *Medical Image Analysis* 39 (2017), pp. 101–123. DOI: 10.1016/j.media.2017.04.010 (cit. on pp. 42, 44).
- [89] N. Milosavljevic. “Rigid Body Transform”. In: *Algorithms for Structure and Motion in Biology*. Stanford University, 2004, pp. 1–10 (cit. on p. 43).
- [90] H. Goldstein. *Classical Mechanics*. Addison-Wesley, 1980 (cit. on p. 43).
- [91] J. Ashburner and K. Friston. “Rigid Body Registration”. In: *Human Brain Function: Second Edition* (2003), pp. 635–653. DOI: 10.1016/B978-012264841-0/50034-2 (cit. on p. 44).
- [92] L. Qin et al. “Prospective head-movement correction for high-resolution MRI using an in-bore optical tracking system”. In: *Magnetic Resonance in Medicine* 62.4 (2009), pp. 924–934 (cit. on p. 44).
- [93] H. Eviatar et al. “Real time head motion correction for functional MRI”. In: *Proceedings of the International Society for Magnetic Resonance in Medicine*. 1999, p. 269 (cit. on p. 44).
- [94] S. Sengupta et al. “Prospective real-time head motion correction using inductively coupled wireless NMR probes”. In: *Magnetic Resonance in Medicine* 72.4 (2014), pp. 971–985 (cit. on p. 44).
- [95] D. A. Feinberg et al. “Hybrid ultrasound MRI for improved cardiac imaging and real-time respiration control”. In: *Magnetic Resonance in Medicine* 63.2 (2010), pp. 290–296 (cit. on p. 44).

## Bibliography

---

- [96] R. Frost et al. “Markerless high-frequency prospective motion correction for neuroanatomical MRI”. In: *Magnetic Resonance in Medicine* 82.1 (2019), pp. 126–144 (cit. on p. 44).
- [97] R. L. Ehman and J. P. Felmlee. “Adaptive technique for high-definition MR imaging of moving structures.” In: *Radiology* 173.1 (1989), pp. 255–263 (cit. on p. 44).
- [98] Z. W. Fu et al. “Orbital navigator echoes for motion measurements in magnetic resonance imaging”. In: *Magnetic Resonance in Medicine* 34.5 (1995), pp. 746–753 (cit. on p. 44).
- [99] A. J. van der Kouwe, T. Benner and A. M. Dale. “Real-time rigid body motion correction and shimming using cloverleaf navigators”. In: *Magnetic Resonance in Medicine* 56.5 (2006), pp. 1019–1032 (cit. on p. 44).
- [100] N. White et al. “PROMO: real-time prospective motion correction in MRI using image-based tracking”. In: *Magnetic Resonance in Medicine* 63.1 (2010), pp. 91–105 (cit. on pp. 44, 110).
- [101] T. Benner, A. J. van der Kouwe and A. G. Sorensen. “Diffusion imaging with prospective motion correction and reacquisition”. In: *Magnetic Resonance in Medicine* 66.1 (2011), pp. 154–167 (cit. on p. 45).
- [102] R. Boegle, J. Maclaren and M. Zaitsev. “Combining prospective motion correction and distortion correction for EPI: towards a comprehensive correction of motion and susceptibility-induced artifacts”. In: *Magnetic Resonance Materials in Physics, Biology and Medicine* 23.4 (2010), pp. 263–273 (cit. on p. 45).
- [103] Q. Razlighi, N. Kehtarnavaz and S. Yousefi. “Evaluating similarity measures for brain image registration”. In: *Journal of Visual Communication and Image Representation* 24.7 (2013), pp. 977–987. DOI: <https://doi.org/10.1016/j.jvcir.2013.06.010> (cit. on p. 48).
- [104] University of Glasgow. *Imaging Centre of Excellence (ICE)*. URL: <http://web.archive.org/web/20230620120921/https://www.gla.ac.uk/colleges/mvls/ice/> (visited on 20/06/2023) (cit. on p. 49).
- [105] NHS Greater Glasgow & Clyde. *Clinical Research Imaging Facility (CRIF)*. URL: <http://web.archive.org/web/20230622161037/https://www.nhsggc.scot/staff-recruitment/staff-resources/research-and-innovation/research-imaging/> (visited on 22/06/2023) (cit. on pp. 49, 74, 92).

- [106] D. C. Hoinkiss et al. “Prospective motion correction in functional MRI using simultaneous multislice imaging and multislice-to-volume image registration”. In: *NeuroImage* 200 (2019), pp. 159–173. DOI: 10.1016/j.neuroimage.2019.06.042 (cit. on pp. 50, 53, 72, 73, 109, 110, 113).
- [107] S. Winata et al. “Optimisation of Navigator Parameter for MS-PACE Prospective Motion Correction”. In: *Postgraduate Meeting of British-Irish and Iberian Chapters of the International Society of Magnetic Resonance in Medicine (ISMRM)* (Online, 15–16 Apr. 2021) (cit. on p. 51).
- [108] S. Winata et al. “Navigator Parameter Optimisation for MS-PACE Prospective Motion Correction”. In: *Proceedings of the 2021 Annual Meeting of the British-Irish Chapter of the International Society of Magnetic Resonance in Medicine (ISMRM) "MR-FEST"* (Online, 13–17 Sept. 2021), p. 27 (cit. on pp. 51, 71).
- [109] S. Winata et al. “Optimising Navigator Scans for Use in MRI Prospective Motion Correction”. In: *15th Scottish Imaging Network: A Platform for Scientific Excellence (SINAPSE) Annual Scientific Meeting* (Online, 16–17 Sept. 2021) (cit. on p. 51).
- [110] S. Winata et al. “Multislice-to-volume registration for detecting intra-volume motion in 7T EPI”. In: *28th Organisation of Human Brain Mapping Annual Meeting (OHBM) Annual Meeting* (Glasgow, Scotland, UK, 19–23 June 2022) (cit. on p. 52).
- [111] S. Winata et al. “Multislice-to-volume Prospective Motion Correction for Functional MRI Protocols at 7T”. In: *Proceedings of the 2023 Annual Meeting of the International Society of Magnetic Resonance in Medicine (ISMRM)* (Toronto, Ontario, Canada, 3–8 June 2023) (cit. on p. 52).
- [112] S. Winata et al. “Prospective Motion Correction for Functional MRI at 7T using Multislice-to-Volume Image Registration”. In: *28th Organisation of Human Brain Mapping Annual Meeting (OHBM) Annual Meeting* (Montreal, Quebec, Canada, 22–26 July 2023) (cit. on p. 52).
- [113] S. Maknojia et al. “Resting state fMRI: Going through the motions”. In: *Frontiers in Neuroscience* 13 (2019), pp. 1–13 (cit. on pp. 53, 89).
- [114] M. Zaitsev et al. “Prospective motion correction in functional MRI”. In: *NeuroImage* 154 (2017), pp. 33–42. DOI: 10.1016/j.neuroimage.2016.11.014 (cit. on p. 53).
- [115] M. Jenkinson et al. “Improved Optimization for the Robust and Accurate Linear Registration and Motion Correction of Brain Images”. In: *NeuroImage* 17.2 (2002), pp. 825–841. DOI: 10.1006/nimg.2002.1132 (cit. on pp. 54, 75, 95).

- [116] P. Huang et al. “Prospective motion correction improves the sensitivity of fMRI pattern decoding”. In: *Human Brain Mapping* 39.10 (2018), pp. 4018–4031. DOI: <https://doi.org/10.1002/hbm.24228> (cit. on p. 73).
- [117] S. Winata et al. “Real-time multislice-to-volume motion correction for task-based functional MRI at 7T”. In: *39th Annual Scientific Meeting of the European Society for Magnetic Resonance in Medicine and Biology (ESMRMB)* (Basel, Switzerland, 4–10 Oct. 2023) (cit. on p. 74).
- [118] S. Winata et al. “Real-time image-based motion correction for 7T task-based functional MRI.” In: *15th Scottish Imaging Network: A Platform for Scientific Excellence (SINAPSE) Annual Scientific Meeting* (Glasgow, Scotland, UK, 14 June 2023) (cit. on p. 74).
- [119] J. Peirce et al. “PsychoPy2: Experiments in behavior made easy”. In: *Behavior Research Methods* 51 (2019), pp. 195–203 (cit. on pp. 74, 92).
- [120] J. P. Marques et al. “MP2RAGE, a self bias-field corrected sequence for improved segmentation and T1-mapping at high field”. In: *NeuroImage* 49.2 (2010), pp. 1271–1281. DOI: <https://doi.org/10.1016/j.neuroimage.2009.10.002> (cit. on p. 74).
- [121] R. Goebel, F. Esposito and E. Formisano. “Analysis of functional image analysis contest (FIAC) data with BrainVoyager QX: From single-subject to cortically aligned group general linear model analysis and self-organizing group independent component analysis”. In: *Human Brain Mapping* 27.5 (2006), pp. 392–401. DOI: <https://doi.org/10.1002/hbm.20249> (cit. on p. 76).
- [122] M. Svanera et al. “CEREBRUM-7T: Fast and Fully Volumetric Brain Segmentation of 7 Tesla MR Volumes”. In: *Human Brain Mapping* 42.17 (2021), pp. 5563–5580. DOI: <https://doi.org/10.1002/hbm.25636> (cit. on p. 76).
- [123] J. Talairach and P. Tournoux. “Co-planar stereotaxic atlas of the human brain”. In: *3-D proportional system: An approach to cerebral imaging* (1988) (cit. on pp. 76, 95).
- [124] J. L. Lancaster et al. “Automated Talairach Atlas labels for functional brain mapping”. In: *Human Brain Mapping* 10.3 (2000), pp. 120–131 (cit. on pp. 76, 96).
- [125] R. A. Poldrack, J. A. Mumford and T. E. Nichols. *Handbook of Functional MRI Data Analysis*. Cambridge University Press, 2011. ISBN: 978-0-5215-1766-9 (cit. on p. 76).
- [126] J. Rissman, A. Gazzaley and M. D’Esposito. “Measuring functional connectivity during distinct stages of a cognitive task”. In: *NeuroImage* 23.2 (2004), pp. 752–763. DOI: <https://doi.org/10.1016/j.neuroimage.2004.06.035> (cit. on p. 76).

- [127] C. A. Schneider, W. S. Rasband and K. W. Eliceiri. “NIH Image to ImageJ: 25 years of image analysis”. In: *Nature Methods* 9.7 (2012), pp. 671–675. DOI: <https://doi.org/10.1038/nmeth.2089> (cit. on p. 87).
- [128] T. Farkas et al. “Activation of the primary motor cortex by somatosensory stimulation in adult rats is mediated mainly by associational connections from the somatosensory cortex”. In: *Neuroscience* 90.2 (1999), pp. 353–361 (cit. on p. 89).
- [129] L. Muckli et al. “Contextual Feedback to Superficial Layers of V1”. In: *Current Biology* 25.20 (2015), pp. 2690–2695. DOI: <https://doi.org/10.1016/j.cub.2015.08.057> (cit. on p. 89).
- [130] V. Gras et al. “Universal pulses: A new concept for calibration-free parallel transmission”. In: *Magnetic Resonance in Medicine* 77.2 (2017), pp. 635–643. ISSN: 15222594. DOI: [10.1002/mrm.26148](https://doi.org/10.1002/mrm.26148) (cit. on p. 92).
- [131] S. N. Williams et al. “Multi-Slice 2D pTx Readout-Segmented Diffusion-Weighted Imaging Using Slice-by-Slice B1+ Shimming”. In: *Proceedings of the 2021 Annual Meeting of the International Society of Magnetic Resonance in Medicine (ISMRM)* (Online, 15–20 May 2021) (cit. on pp. 92, 93).
- [132] B. Ding et al. “Parallel transmit (pTx) with online pulse design for task-based fMRI at 7 T”. In: *Magnetic Resonance Imaging* 93 (2022), pp. 163–174. DOI: <https://doi.org/10.1016/j.mri.2022.07.003> (cit. on p. 92).
- [133] A. T. Curtis et al. “Slice-by-slice B1+ shimming at 7 T”. In: *Magnetic Resonance in Medicine* 68.4 (2012), pp. 1109–1116. DOI: [10.1002/mrm.23319](https://doi.org/10.1002/mrm.23319) (cit. on p. 92).
- [134] S. Winata et al. “Parallel transmit imaging with real-time multislice-to-volume motion correction for task-based functional MRI at 7T”. In: *39th Annual Scientific Meeting of the European Society for Magnetic Resonance in Medicine and Biology (ESMRMB)* (Basel, Switzerland, 4–10 Oct. 2023) (cit. on p. 92).
- [135] S. N. Williams et al. “A Nested Eight-Channel Transmit Array With Open-Face Concept for Human Brain Imaging at 7 Tesla”. In: *Frontiers in Physics* 9 (2021). DOI: [10.3389/fphy.2021.701330](https://doi.org/10.3389/fphy.2021.701330) (cit. on p. 92).
- [136] G. Shajan and D. Feinberg. “An 8-channel transmit 64-channel receive compact head coil for Next Gen 7T scanner with head gradient insert”. In: *Proceedings of the 2022 Annual Meeting of the International Society of Magnetic Resonance in Medicine (ISMRM)* (London, England, UK, 7–12 May 2022) (cit. on p. 92).

- [137] S. Chung et al. “Rapid B1+ mapping using a preconditioning RF pulse with Turbo-FLASH readout”. In: *Magnetic Resonance in Medicine* 64.2 (2010), pp. 439–446. DOI: <https://doi.org/10.1002/mrm.22423> (cit. on p. 92).
- [138] K. Setsompop et al. “Slice-selective RF pulses for in vivo B inhomogeneity mitigation at 7 tesla using parallel RF excitation with a 16-element coil”. In: *Magnetic Resonance in Medicine* 60.6 (2008), pp. 1422–1432. DOI: <https://doi.org/10.1002/mrm.21739> (cit. on p. 93).
- [139] J. Pauly, D. Nishimura and A. Macovski. “A k-space analysis of small-tip-angle excitation”. In: *Journal of Magnetic Resonance* 81 (1989). Magnetic Moments, pp. 43–56. DOI: <https://doi.org/10.1016/j.jmr.2011.09.023> (cit. on p. 93).
- [140] I. Graesslin et al. “A specific absorption rate prediction concept for parallel transmission MR”. In: *Magnetic Resonance in Medicine* 68.5 (2012), pp. 1664–1674. DOI: <https://doi.org/10.1002/mrm.24138> (cit. on p. 93).
- [141] S. M. Smith. “Fast robust automated brain extraction”. In: *Human Brain Mapping* 17.3 (2002), pp. 143–155. DOI: <https://doi.org/10.1002/hbm.10062> (cit. on p. 95).
- [142] W. Thach. “A Role for the Cerebellum in Learning Movement Coordination”. In: *Neurobiology of Learning and Memory* 70.1 (1998), pp. 177–188. DOI: <https://doi.org/10.1006/nlme.1998.3846> (cit. on p. 108).
- [143] K. Uğurbil. “Imaging at ultrahigh magnetic fields: History, challenges, and solutions”. In: *NeuroImage* 168 (2018), pp. 7–32. ISSN: 1053-8119. DOI: <https://doi.org/10.1016/j.neuroimage.2017.07.007> (cit. on p. 108).
- [144] L. Huber, K. Uludağ and H. E. Möller. “Non-BOLD contrast for laminar fMRI in humans: CBF, CBV, and CMRO2”. In: *NeuroImage* 197 (2019), pp. 742–760. DOI: <https://doi.org/10.1016/j.neuroimage.2017.07.041> (cit. on p. 109).
- [145] A. Singh, S. S. M. Salehi and A. Gholipour. “Deep Predictive Motion Tracking in Magnetic Resonance Imaging: Application to Fetal Imaging”. In: *IEEE Transactions on Medical Imaging* 39.11 (2020), pp. 3523–3534. DOI: [10.1109/TMI.2020.2998600](https://doi.org/10.1109/TMI.2020.2998600) (cit. on p. 110).
- [146] D. A. Porter and R. M. Heidemann. “High resolution diffusion-weighted imaging using readout-segmented echo-planar imaging, parallel imaging and a two-dimensional navigator-based reacquisition”. In: *Magnetic Resonance in Medicine* 62.2 (2009), pp. 468–475. DOI: [10.1002/mrm.22024](https://doi.org/10.1002/mrm.22024) (cit. on p. 110).

- [147] R. M. Heidemann et al. “Diffusion imaging in humans at 7T using readout-segmented EPI and GRAPPA”. In: *Magnetic Resonance in Medicine* 64.1 (2010), pp. 9–14. ISSN: 15222594. DOI: 10.1002/mrm.22480 (cit. on p. 110).
- [148] S. Winata et al. “Image Registration Shortcut for Prospective Motion Correction Using Unseparated Multiband Slices”. In: *38th Annual Scientific Meeting of the European Society for Magnetic Resonance in Medicine and Biology (ESMRMB)* (Online, 7–9 Oct. 2021). Vol. 34. *Magnetic Resonance Materials in Physics, Biology and Medicine*, pp. 132–133. DOI: 10.1007/s10334-021-00947-8 (cit. on p. 113).